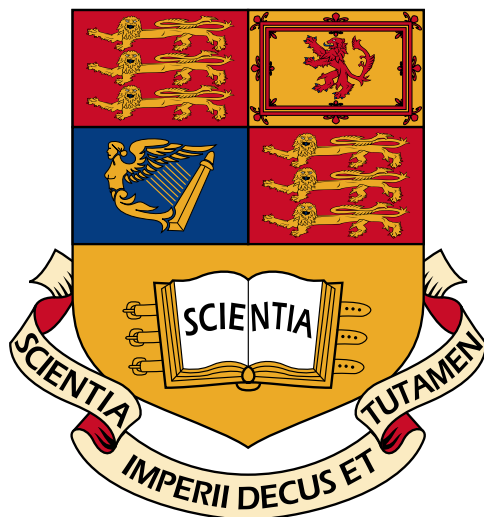


DUST IN STATIONARY AND FLOWING PLASMAS

CHRISTOPHER THOMAS NIGEL WILLIS



Submitted in partial fulfilment of the requirements for the degree of Doctor of Philosophy of
Imperial College London and for the Diploma of Membership of Imperial College.

Department of Physics
The Blackett Laboratory
Imperial College
London SW7 2BZ
November 2011

*The copyright of this thesis rests with the author, and no quotation from it or information
derived from it may be published without prior consent of the author.*

DECLARATION OF ORIGINALITY

I hereby certify that the material of this thesis, which I now submit for the award of Doctor of Philosophy, is entirely my own work unless otherwise cited or acknowledged within the body of text.

London, November 2011

Christopher Thomas Nigel Willis

ABSTRACT

This thesis contains work of a computational and theoretical nature. The floating potential of dust grains immersed in plasma is investigated via particle-in-cell simulation for a range of parameters. In particular, work is focused on the charging of grains large with respect to the electron Debye length. Numerical fits are given for the floating potential of large grains in stationary and flowing plasma. A modified version of the well known orbit-motion-limited (OML) theory is developed for large dust grains. The modified OML theory is shown to be in good agreement with simulation. This modified theory is then adapted for use with flowing plasmas. In the case of flowing plasma, for low ion temperatures and flow speeds upwards of Mach 1, interesting and unexpected effects are seen in the potential and density distribution around dust grains, these are investigated and discussed. Finally, the application of this work is outlined with particular focus on dust grains in a tokamak plasma environment.

CONTENTS

1	INTRODUCTION	14
1.1	The Debye length	14
1.2	Dust in Space	16
1.2.1	The Sound Speed	18
1.3	Dust Crystals	18
1.4	Dust in Industry	18
1.5	Dust in Fusion	19
1.5.1	Wall Interactions and the SOL	20
1.5.2	ELMs and Disruptions	21
1.5.3	Size Distribution	23
1.5.4	Dust in TOKamkS	24
1.6	Summary	25
2	BACKGROUND THEORY - CHARGING OF DUST GRAINS	26
2.1	The Maxwellian Distribution	26
2.2	The Debye-Hückel Potential	27
2.3	The Boltzmann Relation	27
2.4	Plane Retarding Probe	28
2.4.1	The Flux	29
2.4.2	The Density	30
2.5	Spherical Retarding Probe	30
2.6	Spherical Accelerating Probe	32
2.7	Sheath and Presheath	36
2.7.1	The Bohm Criterion for Cold Ions	36
2.7.2	The Bohm Criterion for Hot Ions	38
2.7.3	Presheath Types	39
2.8	Charging Models	41
2.8.1	Allen Boyd Reynolds	41
2.8.2	Orbit Motion Theory	44
3	SCEPTIC OUTLINE	52
3.1	Particle-in-Cell Codes	52
3.1.1	The Computational Problem	53
3.1.2	Leap-Frog	55
3.1.3	Computational Mesh and Finite-Difference Scheme	55
3.1.4	Particle Weighting	58
3.1.5	Instabilities	59
3.1.6	Inner Boundary	59
3.1.7	Outer Boundary	60
3.1.8	Benchmark	63
4	LARGE GRAINS IN A STATIONARY PLASMA	65
4.1	Numerical Fits to the Floating Potential	65
4.1.1	Departure from OML	66

4.1.2	Three Potential Regions	66
4.1.3	Asymptotic Limit of the Floating Potential	67
4.1.4	Numerical Fits	68
4.1.5	Recap on Numerical Fits	70
4.2	Modifying OML	73
4.2.1	Large Dust Grains	73
4.2.2	Introduction to Modified OML	76
4.2.3	Intermediate Values of ρ	80
4.2.4	The Validity of Modified OML	81
4.3	Summary	87
5	LARGE GRAINS IN A FLOWING PLASMA	88
5.1	SOML for Small Grains	88
5.1.1	Low Flow Limit	89
5.1.2	Large Flow Limit	91
5.1.3	The Potential Contribution	91
5.2	SOML for Large Grains	94
5.2.1	The Breakdown of SOML	94
5.2.2	Modified SOML	97
5.2.3	Comparison with Simulation	99
5.2.4	Intermediate Values of ρ	103
5.3	Comparison with Experiment	104
5.4	Summary	104
6	MACH CONES	106
6.1	The Warm Ion Sound Speed	108
6.1.1	The Generalised Bohm Criterion	108
6.2	Differences: Dust Immersed in a Plasma/Neutral Gas	110
6.2.1	The Effect of Ion Temperature	111
6.3	A Hydrodynamic Analog	113
6.3.1	Downstream Negative Space Charge	114
6.3.2	Gas Dynamics	116
6.4	The Presheath in Supersonic Flow	117
6.5	Comparison with Experiment	119
6.6	Summary	119
7	LARGE GRAINS AND THE ION DRAG FORCE	121
7.1	DTOKS Outline	122
7.1.1	Secondary Charging	125
7.1.2	Ion Drag Force	125
7.1.3	A Few Potential Choices	127
7.2	2D Background	130
7.3	3D Background	131
7.3.1	Dust grains in MAST	131
7.3.2	Dust grains in ITER	132
7.4	Application to Other Problems	133
8	SUMMARY AND FURTHER WORK	134
8.1	Summary and Closing Remarks	134

8.2 Further Work	135
8.2.1 Modifications to SCEPTIC	135
8.2.2 Double Cones	136
8.2.3 Modification to DTOKS	137
I APPENDIX	148
A APPENDIX	149
A.1 The Sound Speed	149
B APPENDIX	151
B.1 ITER and MAST	151
C APPENDIX	154
C.1 SOML Ion Drag via Collection	154
C.2 Accelerated Maxwellian: 1D	156

LIST OF FIGURES

Figure 1.1	The Bow Shock around the Earth and the extended magnetic field due to the solar wind	17
Figure 1.2	A schematic depicting the Limiter and Divertor. Also indicated are the Scrape-off Layer, Core plasma and Separatrix.	20
Figure 1.3	Dust trajectories from a disruption like event in MAST, the purple shaded area represents the core plasma.	22
Figure 1.4	Distribution of dust grain diameters, grains collected from the bottom of the ASDEX-upgrade tokamak. The red boxes indicate the data frequency and the black line is a log normal fit. This figure is reproduced from Fig.3 in [40].	23
Figure 1.5	Scanning electron microscope images of material from the TEXTOR tokamak [28]. The marked spaces represent 0.1mm.	24
Figure 2.1	The potential around a small grain, $\rho = 10^{-3}$. Numerical calculations [48] from full orbital motion theory (section 2.8.2.3) are compared with the Debye-Hückel potential. $\rho = r_d/\lambda_D$ where r_d is the dust grain radius. . .	28
Figure 2.2	The Boltzmann relation for electron density (red) compared with eqn.(2.14) (green) for a number of wall potentials. a) $\Phi = 0.5$, b) $\Phi = 1.2$ c) $\Phi = 3.0$ d) $\Phi = 8.0$	31
Figure 2.3	The three terms in eqn.(2.24) as a function of v_r	33
Figure 2.4	Schematic representation of the absorption radius.	34
Figure 2.5	Effective potential, eqn.(2.23), taking $\phi(r)$ steeper than an inverse square. .	35
Figure 2.6	Effective potential, eqn.(2.23), taking $\phi(r)$ proportional to an inverse square. .	35
Figure 2.7	Effective potential, eqn.(2.23), taking $\phi(r)$ to be less steep than an inverse square.	35
Figure 2.8	The top-hat distribution function, eqn.(2.37)	39
Figure 2.9	Solution to eqn.(2.51) for various J (indicated on graph). The solution is double valued with the turning points at the sheath edge, $\Phi = 0.5$. $\zeta = r/\lambda_D$ and $\Phi = -e\phi/kT_e$	43
Figure 2.10	Solution to ABR, $\rho = r_d/\lambda_D$ and $\Phi = -e\phi/kT_e$	44
Figure 2.11	A grazing orbit for a repelled particle with impact parameter h_j	46
Figure 2.12	Solution to eqn.(2.62) for various plasma ion species (indicated on the graph). $\beta = T_i/T_e$ and $\Phi = -e\phi/kT_e$	47
Figure 2.13	sOML floating potential as a function of flow for various β s (indicated on the graph). The ion species is hydrogen. u is the flow speed normalised by $\sqrt{kT_e/m_i}$ and $\Phi = -e\phi/kT_e$	48
Figure 2.14	A comparison of OM [48], OML (dashed) and ABR as a function of ρ for various β s (indicated on the graph). $\rho = r_d/\lambda_D$ and $\Phi = -e\phi/kT_e$	49
Figure 2.15	Absorption radius position as a function of ion energy for monoenergetic ions following Bohm, Burhop and Massey [69]. β^+ is the monoenergetic ion energy normalised by kT_e	50
Figure 3.1	A typical RIC cycle	53

Figure 3.2	Standard Leap Frog	55
Figure 3.3	The SCEPTIC grid. Cells at small r have a smaller area than those at large r	56
Figure 3.4	There is a lack of resolution along the axis of flow.	58
Figure 3.5	Examples of particle weighting using NGP and CIC	58
Figure 3.6	A schematic illustrating ions, indicated by the three arrows, which will be missing in the phase space far from the dust grain, the red sphere.	61
Figure 3.7	Simulation values of the floating potential for $\beta = 0.01$ (blue), 0.10 (green) and 1.00 (red) for a hydrogen plasma. The solid curves are from OM theory and the dotted horizontal lines the corresponding OML values. $\rho = r_d/\lambda_D$ and $\Phi = -e\phi/kT_e$	62
Figure 4.1	The OML potential as a function of β . The top line is the OML result for argon and the bottom line for hydrogen. SCEPTIC values are also shown. $\Phi = -e\phi/kT_e$ and $\rho = 0.04$	63
Figure 4.2	The potential from SCEPTIC compared with $1/r^2$ testing the condition (4.1). $\beta = 0.2$, $\rho = 80$	65
Figure 4.3	The % difference between the floating potential from simulation ($\Phi_{\text{sim.}}$) and OML, a range of β are shown (indicated on the graph). The red, dashed line indicates a 10% departure, the solid lines indicate the data trend. $\rho = r_d/\lambda_D$	66
Figure 4.4	β and ρ parameter space showing the difference between potential from simulation and OML, a range of β are shown. $\rho = r_d/\lambda_D$ and $\beta = T_i/T_e$	67
Figure 4.5	Potential approaching an asymptote for $\beta = 2$ (top line) and 4 (bottom line) for large ρ . $\rho = r_d/\lambda_D$ and $\Phi = -e\phi/kT_e$	68
Figure 4.6	OML and expressions (4.2) and (4.3) in the relevant regions compared with SCEPTIC data. $\beta = 1.00$ topmost line (□), $\beta = 0.10$ middle line (○) and $\beta = 0.01$ bottommost line (+). $\Phi = -e\phi/kT_e$ and $\rho = r_d/\lambda_D$	70
Figure 4.7	OML and expressions (4.2) and (4.3) in the relevant regions compared with SCEPTIC data. $\beta = 1.00$ topmost line (□), $\beta = 0.10$ middle line (○) and $\beta = 0.01$ bottommost line (+). $\Phi = -e\phi/kT_e$ and $\rho = r_d/\lambda_D$	71
Figure 4.8	OML and expressions (4.2) and (4.3) in the relevant regions compared with SCEPTIC data. $\beta = 1.00$ topmost line (□), $\beta = 0.10$ middle line (○) and $\beta = 0.01$ bottommost line (+). $\Phi = -e\phi/kT_e$ and $\rho = r_d/\lambda_D$	71
Figure 4.9	OML and expressions (4.2) and (4.3) in the relevant regions compared with SCEPTIC data. $\beta = 1.00$ topmost line (□), $\beta = 0.10$ middle line (○) and $\beta = 0.01$ bottommost line (+). $\Phi = -e\phi/kT_e$ and $\rho = r_d/\lambda_D$	72
Figure 4.10	OML and expressions (4.2) and (4.3) in the relevant regions compared with SCEPTIC data. $\beta = 1.00$ topmost line (□), $\beta = 0.10$ middle line (○) and $\beta = 0.01$ bottommost line (+). $\Phi = -e\phi/kT_e$ and $\rho = r_d/\lambda_D$	72
Figure 4.11	Simulation results for hydrogen and argon, $\rho = 100$. The solid lines are from the analytic treatment, eqn.(4.9). The dotted lines are eqn.(4.2) with the thin sheath parameters, Table 4.2. $\beta = T_i/T_e$ and $\Phi = -e\phi/kT_e$	73
Figure 4.12	The ion (red) and electron (blue) densities and the potential (green) as a function of radius for a large dust grain. $\Phi = -e\phi/kT_e$	75

Figure 4.13	Gradient of the potential (solid) and the gradient of $1/r^2$ (modulus). $\beta = 0.2$, $\rho = 80$	77
Figure 4.14	The floating potential (\times) as a function of β for large grains ($\rho = 100$) in a stationary, hydrogenic plasma. The solution to eqn.(4.15) is shown for a number of γ s. $\Phi = -e\phi/kT_e$	79
Figure 4.15	Floating potential as a function of β for large grains ($\rho = 100$) in a stationary, hydrogenic plasma. SCEPTIC data (\times), OML potential (yellow), solution to eqn.(4.15) (red), the sheath drop given by eqn.(4.8) (green) and the grain potential assuming the ions ignore the electric field (purple). $\beta = T_i/T_e$ and $\Phi = -e\phi/kT_e$	80
Figure 4.16	The floating potential according to Modified OML vs SCEPTIC data, the Transition region is calculated using eqn.(4.17). $\rho = r_d/\lambda_D$ and $\Phi = -e\phi/kT_e$	81
Figure 4.17	Effective Potential contours shown in blue for increasing J , the red squares indicate maxima and the green dashed line represents the sheath edge at $1.08r_d$. $\rho = 100$, $\beta = 1.0$ and U is normalised by kT_e	82
Figure 4.18	Effective Potential maxima (red \square) and energy distribution of the ions for $\beta = 1.0$ (blue line), the green dashed line represents the sheath edge. U is normalised by kT_e	83
Figure 4.19	J_{crit} from OML, eqn.(4.19) (blue) and J_{crit} from SCEPTIC data (red) for $\beta = 1.0$, the ion energy distribution is also shown. J is normalised by $m_i r_d \sqrt{kT_e/m_i}$	85
Figure 4.20	The blue line is J_{crit}^{OML} with $\Phi_d = 0.80$ and the red line is J_{crit}^{sim} , the critical angular momentum found from simulation. The shaded area highlights the difference between the two. J is normalised by $m_i r_d \sqrt{kT_e/m_i}$	86
Figure 5.1	Terms 1, 2, 3 and 4 in the SOML ion current from eqn.(5.5). u is normalised by $\sqrt{kT_e/m_i}$ and I_i by $4\pi r_d^2 n_i e \sqrt{kT_i/2\pi m_i}$	92
Figure 5.2	The potential distribution around a grain of $\rho = 0.04$, $u = 3.0$ and $\beta = 0.3$. The contours indicate equipotentials, the outermost is for $\Phi = 0.02$, and moving inwards, 0.05, 0.1, 0.3 and 0.5. $\Phi = -e\phi/kT_e$ and u is normalised by $\sqrt{kT_e/m_i}$	93
Figure 5.3	The floating potential from SCEPTIC for small ρ ($\rho = 0.04$) as a function of flow velocity for a number of β s. The solid lines are the solutions to SOML. u is normalised by $\sqrt{kT_e/m_i}$ and $\Phi = -e\phi/kT_e$	94
Figure 5.4	The floating potential from SCEPTIC for various ρ (indicated on the figure) and $\beta = 1$. The solid line is SOML. u is normalised by $\sqrt{kT_e/m_i}$ and $\Phi = -e\phi/kT_e$	95
Figure 5.5	The potential distribution around a large dust grain, $\rho = 80$, for flow speeds of a) $u = 0.3$, b) $u = 0.9$ and c) $u = 1.3$. $\beta = 0.2$. u is normalised by $\sqrt{kT_e/m_i}$ and $\Phi = -e\phi/kT_e$	96
Figure 5.6	The original is Fig. 7 in [87]. Typical ion orbits below the transition ($u = 0.5$) and above the transition ($u = 0.8$). u is normalised by $\sqrt{kT_e/m_i}$	97
Figure 5.7	Terms 1, 2, 3, 4 (from eqn.(5.5)) and the modified version of term 3, $\beta = 0.1$. u is normalised by $\sqrt{kT_e/m_i}$ and I_i by $4\pi r_d^2 n_i e \sqrt{kT_i/2\pi m_i}$	99

Figure 5.8	SCEPTIC values for the floating potential of a large dust grain in a flowing plasma. The solid lines are the solutions to eqn.(5.19) for various γ , the dashed line is normal SOML, $\beta = 1.0$ and $\rho = 100$. $\Phi = -e\phi/kT_e$ and the flow speed u is normalised by $\sqrt{kT_e/m_i}$	100
Figure 5.9	SCEPTIC values (\times) for the floating potential of a large dust grain in a flowing plasma. The topmost, red and purple lines assume the ions are cold/hot respectively, and ignore the electric field. The middle, yellow line is modified SOML, eqn.(5.19) with $\Delta\Phi$ from eqn.(4.8), and the bottom, green line is SOML. $\rho = 100$, u is normalised by $\sqrt{kT_e/m_i}$ and $\Phi = -e\phi/kT_e$	101
Figure 5.10	SCEPTIC values (\times) for the floating potential of a large dust grain in a flowing plasma. The topmost, red and purple lines assume the ions are cold/hot respectively, and ignore the electric field. The middle, yellow line is modified SOML, eqn.(5.19) with $\Delta\Phi$ from eqn.(4.8), and the bottom, green line is SOML. $\rho = 100$, u is normalised by $\sqrt{kT_e/m_i}$ and $\Phi = -e\phi/kT_e$	102
Figure 5.11	Floating potential of a large grain in a helium plasma. $\beta = 1.0$, $\rho = 80$. The dashed line is normal SOML, the solid line is modified SOML, eqn.(5.19), and (+) is data from SCEPTIC. u is normalised by $\sqrt{kT_e/m_i}$ and $\Phi = -e\phi/kT_e$	103
Figure 6.1	The potential around a grain of $\rho = 1$ in a flowing plasma, $u = 2.5$ and $\beta = 0.3$. A region of positive space charge is seen directly behind the grain. $\Phi = -e\phi/kT_e$ and u is normalised by $\sqrt{kT_e/m_i}$	107
Figure 6.2	The potential required to satisfy the Generalised Bohm Criterion for a shifted Maxwellian as a function of flow velocity. u is the flow velocity normalised by $\sqrt{kT_e/m_i}$, $\beta = 1.0$ and $\delta\Phi = -e\delta\phi/kT_e$	109
Figure 6.3	Schematic representation of the flow pattern in a) the conventional case of an object in supersonic flow and b) an absorbing dust grain in supersonic flow.	110
Figure 6.4	Simple model of ion flow past a dust grain, as the amount of random motion is increased the double cone is lost. The random component is a) 10%, b) 20%, c) 40% and d) 50% of the flow speed.	111
Figure 6.5	The transition from double to single cone for $\beta = 0.2$ to $\beta = 0.7$. The flow velocity is $1.75\sqrt{kT_e/m_i}$ and the grain radius is $\rho = 80$. $\Phi = -e\phi/kT_e$	112
Figure 6.6	Potential distribution Φ a) Single cone: $\beta = 1.0$, $\rho = 80$, $u = 2.5$. b) Double cone: $\beta = 0.2$, $\rho = 80$, $u = 2.5$. u is normalised by $\sqrt{kT_e/m_i}$	113
Figure 6.7	Ion density contour (red, dashed line) and the z component of the flow, v_z (green, solid line). The contour is taken from the downstream wake at $z = 2.0r_d$. Here $\beta = 0.3$, $u = 3.0$ and $\rho = 40$. u is normalised by $\sqrt{kT_e/m_i}$. $\beta = 0.2$, $\rho = 80$. Position of the stagnation point (+), position of the downstream sheath boundary (\square) and density at the stagnation point (\times). u is normalised by $\sqrt{kT_e/m_i}$	114
Figure 6.8	a) Radial velocity (in spherical coordinates) contours around a large dust grain in a flowing plasma, the left most contour is $v_r = \sqrt{kT_e/m_i}$ and closes on the dust grain. b) The break down in quasineutrality. $\beta = 0.2$, $u = 3\sqrt{kT_e/m_i}$ and $\rho = 80$	115
Figure 6.9	Flow velocity at which the upstream presheath width goes to zero. Fits are $\sqrt{1+\gamma\beta}$ with $\gamma = 1$ (red, dot dashed), $\gamma = 5/3$ (yellow, solid) and $\gamma = 3$ (green, dashed). u is normalised by $\sqrt{kT_e/m_i}$	117
Figure 6.10	Flow velocity at which the upstream presheath width goes to zero. Fits are $\sqrt{1+\gamma\beta}$ with $\gamma = 1$ (red, dot dashed), $\gamma = 5/3$ (yellow, solid) and $\gamma = 3$ (green, dashed). u is normalised by $\sqrt{kT_e/m_i}$	118

Figure 7.1	Representation of the 3D background used by <code>DTOKS</code> . The electron temperature in <code>MAST</code> is shown, red indicates hotter regions and blue cooler.	121
Figure 7.2	<code>DTOKS</code> background for T_e , T_i and β in <code>MAST</code>	123
Figure 7.3	<code>DTOKS</code> background, T_e , T_i and β in <code>ITER</code>	124
Figure 7.4	Ion drag components, “ F_c in <code>DTOKS</code> ” is the original ion drag model, eqn.(7.1). The <code>SCEPTIC</code> data is reproduced from Fig.14 of [87], $\rho = 100$ and $\beta = 0.1$. The other 4 solid lines are the drag force from eqn.(7.2) as explained in the text. u is normalised by $\sqrt{kT_e/m_i}$	128
Figure 7.5	F_c determined via eqn.(7.2) with the potential drop across the presheath used as Φ . The summation of F_c and F_s is seen to fit the <code>SCEPTIC</code> data very well. The <code>SCEPTIC</code> data is reproduced from Fig.14 of [87], $\rho = 100$ and $\beta = 0.1$. u is normalised by $\sqrt{kT_e/m_i}$	129
Figure 7.6	The velocity evolution with time of a dust grain. Each line is calculated using F_c given by eqn.(7.2). The potential described by: oml for the topmost, green line, soml for the middle, blue line, and the potential at the sheath edge calculated using modified soml for the bottom, red line.	130
Figure 7.7	Dust trajectories from the lower divertor in <code>MAST</code> . Carbon grains of $r_d = 20\mu\text{m}$ are injected with initial velocity 15ms^{-1} and two injection angles. The red and blue trajectories indicate the two approaches to the drag force discussed in the text.	131
Figure 7.8	Trajectories of tungsten spheres in <code>ITER</code> . Each grain has an initial radius of $15\mu\text{m}$ and is launched perpendicular to the divertor with initial velocity of 7ms^{-1}	132
Figure 7.9	Trajectories of tungsten spheres in <code>ITER</code> , top-down view. Each grain has an initial radius of $15\mu\text{m}$ and is launched perpendicular to the divertor with initial velocity of 7ms^{-1}	133
Figure 8.1	The inner boundary shape (shaded area) required for a cylindrical grain in relation to the computational mesh.	136
Figure 8.2	The inner boundary shape (shaded area) required for a conical object directed into the flow.	137
Figure B.1	A comparison of scale between the <code>MAST</code> and <code>ITER</code> plasmas	152
Figure B.2	A schematic representation of <code>ITER</code> 's plasma and main vessel components.	153
Figure C.1	Ion drag	154

LIST OF TABLES

Table 3.1	Spacing in the cosine of the angle.	57
Table 4.1	Values for the oml limit. Expression (4.2)	69
Table 4.2	Values for the thin sheath limit. Expression (4.2)	69

LIST OF SYMBOLS AND ACRONYMS

$a_{x,y,z}$	Shifted Maxwellian drift components
A	Mass number
β	Ratio of ion to electron temperature
β^+	Monoenergetic ion energy normalised by kT_e
c_s	Cold ion sound speed
c_{hot}	Hot ion sound speed
\bar{c}	Maxwellian distribution average/thermal speed
d	Subscript indicating a dust grain quantity
Δ	Grid spacing
$\Delta\Phi$	Sheath potential drop
$\delta\Phi$	Presheath potential drop
e	Electron charge
e	Subscript indicating electron quantity
ϵ_0	Permittivity of free space
E	Total energy
E	Electric field
f	Distribution function
F	Force
F_c	Ion drag collection force
F_s	Ion drag scattering force
h_j	Impact parameter
γ	Adiabatic index
Γ_j	Flux
i	Subscript indicating ion quantity
I_j	Current
j	Subscript indicating plasma particle
j	Current density
J	Normalised current density
k	Boltzmann constant
λ_D	Electron Debye length
m_j	Mass
n_j	Density
ω_{p_j}	Plasma frequency
p_j	Pressure

ϕ	Potential
Φ	Normalised potential
q	Charge
r_d	Dust radius
ρ	Dust radius normalised by electron Debye length
ρ_q	Charge density
se	Subscript indicating sheath edge quantity
σ_j	Cross section
T_j	Temperature
u	Flow speed normalised by $\sqrt{kT_e/m_i}$
U	Effective potential
$v_{x,y,z,r,\theta}$	Velocity components
v_{Ti}	Ion thermal velocity
w	$\sqrt{v_x^2 + v_y^2 + v_z^2}$
X	Position normalised by λ_D
Z	Atomic number
ζ	Radial position normalised by λ_D
η and μ	Parameters used in numerical fits

ABR	Allen, Boyd, Reynolds
ASDEX	Axially Symmetric Divertor EXperiment
CFC	Carbon-Fibre-Composite
ELM	Edge Localised Mode
EMC	Electrostatic Mach Cone
GBC	Generalised Bohm Criterion
ITER	International Thermonuclear Experimental Reactor
JET	Joint European Tokamak
LCFS	Last Closed Flux Surface
MAST	Mega Ampere Spherical Tokamak
MOML	Modified Orbital-Motion-Limited
OM	Full Orbit Motion
OML	Orbital-Motion-Limited
PFC	Plasma Facing Component
SCEPTIC	Specialised Coordinate Electrostatic Particles and Thermals In Cell
SOL	Scrape-Off Layer
SOML	Shifted Orbital-Motion-Limited
TEXTOR	Tokamak EXperiment for Technology Oriented Research

INTRODUCTION

If we ionise a gas, partially or fully, the resulting state of matter is a plasma. Plasmas are neutral as a whole but composed of two mingled populations of positive and negative particles, in addition to any neutral particles. As a result, plasmas respond collectively to applied electromagnetic fields.

This first chapter introduces the motivation for the subsequent work and, along with Chapter 2, reviews the work that has already been done. We will see that plasmas are not only critical for the technologies that support everyday life, they make up the majority of the visible mass in the universe.

Just as plasmas are ubiquitous in our universe, dust is ubiquitous in plasmas [1]. The presence of this dust has opened a vista of research topics ranging from astrophysical application to dust crystals. Before outlining some of the most common dusty plasma research areas we note that when dealing with these systems the floating potential of the dust grains, that is the potential at which the ion and electron currents to the grain balance, is of paramount importance. To determine the forces acting upon a given dust grain, its subsequent trajectory and lifetime, the floating potential must be known.

1.1 THE DEBYE LENGTH

One of the critical parameters in this work is the length scale of an object with respect to relevant shielding lengths in the plasma. As such, we immediately introduce the concept of Debye shielding following Chen [2].

Inserting a charged object (and maintaining the charge on it) into a plasma, the constituent components of the plasma will move in accordance. A cold plasma will perfectly screen the charge but a finite temperature plasma will not. Instead a region of positive space charge will form around the charged object, this region is called the sheath and is discussed further in section 2.7. Most of the potential drop due to the charged object is across the sheath. In addition, over a length scale of many times the sheath width a presheath forms. The potential drop across the presheath is much smaller than the drop across the sheath as well as being over a much larger distance. We will see in section 2.7 that the presheath plays an

important role and is required to join the sheath region to the bulk plasma.

Taking the 1D case of a plane held at some potential ϕ_0 , Poisson's equation in 1D is

$$\frac{d^2\phi}{dx^2} = -\frac{e}{\epsilon_0}(n_i - n_e). \quad (1.1)$$

The ion and electron densities are given by n_i and n_e respectively, e is the elementary charge and ϵ_0 the permittivity of free space. The density far away from the plane is n_∞ and the ions are assumed to be so massive that they are stationary on the timescale of the shielding, hence $n_i = n_\infty$. As will be shown later (section 2.3), the electron distribution is well approximated by the Boltzmann relation

$$n_e = n_\infty \exp\left(\frac{e\phi(x)}{kT_e}\right), \quad (1.2)$$

where k is the Boltzmann constant and T the temperature (ion and electron temperatures will be marked with the subscripts i and e respectively). Equation (1.2) tells us that there are fewer electrons where ϕ is more negative.

Substituting the ion and electron densities into eqn.(1.1)

$$\frac{d^2\phi}{dx^2} = \frac{en_\infty}{\epsilon_0}(e^{\frac{e\phi(x)}{kT_e}} - 1). \quad (1.3)$$

Defining $\Phi = -e\phi/kT_e$, when $\Phi \ll 1$, we may expand the exponential as $e^\Phi \rightarrow 1 + \Phi$. This is not appropriate near the plane where the potential is large. However, as the majority of the potential is developed across a thin region near the plane (section 2.7), it does not contribute much to the charge.

$$\begin{aligned} \frac{d^2\phi}{dx^2} &\approx \frac{en_\infty}{\epsilon_0}\left(1 + \frac{e\phi(x)}{kT_e} - 1\right) = \frac{e^2 n_\infty}{\epsilon_0 k T_e} \phi \\ \frac{d^2\phi}{dx^2} &= \frac{1}{\lambda_D^2} \phi. \end{aligned} \quad (1.4)$$

Where the (electron) Debye length is defined

$$\lambda_D = \sqrt{\frac{\epsilon_0 k T_e}{n_\infty e^2}}. \quad (1.5)$$

This length scale, in relation to the object being charged, is critical. Considering a plasma immersed sphere instead of the 1D case we write eqn.(1.4) in spherical coordinates, assuming spherical symmetry

$$\frac{d^2\phi}{dr^2} + \frac{2}{r} \frac{d\phi}{dr} = \frac{1}{\lambda_D^2} \phi. \quad (1.6)$$

The analytic solution to this is the Debye-Hückel potential

$$\phi(r) = \phi(0) \frac{r_d}{r} \exp\left(\frac{r_d - r}{\lambda_D}\right), \quad (1.7)$$

where r_d is the radius of the dust grain. The Debye-Hückel potential is discussed in section 2.2. We introduce the dimensionless quantity ρ as the radius of a plasma immersed object divided by λ_D ($\rho = r_d/\lambda_D$). Objects much smaller than the Debye length will have small ρ , objects much larger will have large ρ . As we will see, many factors depend on ρ and the behaviour of a system can vary strongly as ρ is altered.

The importance of the floating potential was noted above. We shall see in Chapter 2 that when $\rho \ll 1$ the potential is well described by a simple theory. For $\rho \gtrsim 1$ no simple theory exists, Chapters 4 and 5 are concerned with describing the floating potential of grains in this region. In Chapter 4 we fit simulation data for the floating potential as a function of ρ . We then modify the simple theory appropriate for small grains for use with large grains. Chapter 5 then extends this work for flowing plasmas.

Whilst the main motivation for this work is dust present in magnetic confinement fusion devices, the work in this thesis is applicable to plasma immersed dust generally. We now consider some of the areas where work on plasma immersed dust behaviour has a practical application.

1.2 DUST IN SPACE

Much work has been done concerning dust in space. Application ranges from the interstellar medium [3], star formation due to gravitational collapse may depend on dust charge [4], to spacecraft charging in the solar wind [5]. The solar wind is a plasma with flow velocity around 500 km s^{-1} and temperature around 100 eV [6]. The density is extremely low, $\sim 7 \times 10^6 \text{ m}^{-3}$ [7], giving a typical Debye length of approximately 30m.

Charging of space craft and the resulting drag forces are also important. Spacecraft radii range from satellites, a few meters, to the International Space Station ($\sim 110\text{m}$ long) and are likely to increase, this gives a range of ρ from 0.1 to 3. The Earth itself may be considered as a large dust grain (at least it is spherical!) in the flowing plasma of the solar wind ($\rho \gg 1$). A representation of the bow shock is shown in Fig. 1.1, large dust grains in flowing plasmas are investigated in Chapters 5 and 6. In Chapter 5 we investigate the effect of flow on the floating potential of dust grains. In Chapter 6 the effects on the plasma surrounding dust grains, primarily those with $\rho \gg 1$ is investigated in supersonic flow.

The Earth's bow shock and the solar wind are complicated by magnetic fields. Work has been done concerning plasma immersed dust with magnetic fields present. Samsonov has investigated the behaviour of magnetic grains with a magnetic field [8] and Hutchinson has investigated the result on ion collection by probes in the presence of strong magnetic fields [9]. Dust in the magnetic field of our galaxy's spiral arms, $\rho \ll 1$, has also been used as an astrophysical diagnostic [3]; all the situations we investigate are purely electrostatic.

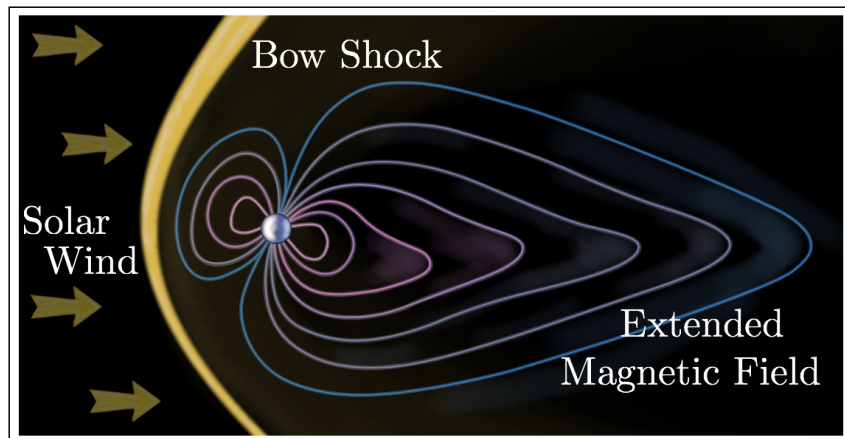


Figure 1.1.: The Bow Shock around the Earth and the extended magnetic field due to the solar wind.

Dusty plasma work is also ongoing on the International Space Station (plasma immersed object experiments within a plasma immersed object), interesting phenomena are observed and investigated under microgravity conditions [10]. Finally, dust exists in planetary ring systems. The planetary rings of Jupiter, Saturn, Uranus and Neptune are comprised mainly of dust in the micrometer range [11].

1.2.1 The Sound Speed

The solar wind has a flow speed of $\approx 500 \text{ km s}^{-1}$, assuming the ions to be cold the sound speed is $\sqrt{kT_e/m_i} \approx 100 \text{ km s}^{-1}$ and clearly the flow is supersonic. Difficulties arise as to how to define the sound speed when the ions are warm. Riemann discusses this in [12], the additional pressure term due to the warm ions in the fluid description leads to a sound speed of ¹

$$v_s = \sqrt{\frac{k(T_e + \gamma T_i)}{m_i}}$$

where $\gamma = 1$ for isothermal flow, $5/3$ for adiabatic flow with isotropic pressure and 3 for one-dimensional adiabatic flow. The different values of γ reflect the uncertainty arising from the cut-off of the hydrodynamic hierarchy. Whilst the choice of γ seems to be clearly defined, in Chapters 5 and 6 we shall see that this is not necessarily the case.

1.3 DUST CRYSTALS

The interesting and relatively young field of plasma physics which we now touch upon is that of plasma crystals. Plasma crystals were first observed in 1994 by Thomas *et al* [13] and have been the subject of much interest. The crystals form when many dust grains, individually charged and each with a Debye sheath, interact with each other. Providing the ratio of inter-particle potential energy to thermal energy is large enough, a crystal will form.

A primary use for plasma crystals is the study of phase transitions [14, 15]. The fact that the crystals are visible to the naked eye and easily photographed makes them ideal for this kind of work, the phase transitions can be observed. In addition, much work has been done by Samsonov on topics such as shock propagation [16, 17] and Mach cones [18, 19]. This work on the formation of Mach cones is of particular interest as we investigate the response of plasma surrounding a single dust grain in supersonic plasma flow in Chapter 6.

1.4 DUST IN INDUSTRY

One driving force behind work on dusty plasmas is the formation of dust in industrial plasmas, producing integrated circuits requires the repetition of layer

¹ See A.1 for details.

deposition and etching [20]. As well as manufacturing integrated circuits, plasma processing is vital to materials processing and surface fabrication, from automotive and aerospace to biomedical [21]. In order to work at the required length scale (10s of nanometers) requires plasmas. Plasmas have the ability to “grow” their own dust [22, 23] via various chemical processes or from sputtering of vessel components such as the electrodes, in effect this means it is almost impossible to completely eliminate dust from your system. It has been known for some time that dust particles of $1\mu\text{m}$ and larger form in the types of plasma used for etching and deposition [24]. This dust typically resides in the sheath edge (section 2.7), just above the wafers, and falls onto the wafers when the plasmas are “turned off”. The resulting contamination raises the number of component fails and hence increases production costs [20].

1.5 DUST IN FUSION

The final dusty plasma scenario we discuss, and the motivation for our work, is that of dust as a contaminant in a magnetic confinement fusion reactor, a tokamak² (see Fig. B.2 in Appendix B.1 for a schematic illustration of ITER). Current magnetic confinement devices do not appear to be hampered by dust, in fact some work has shown that intentional dust application may be beneficial [25]. Next generation devices, such as ITER, plan to sustain burning plasmas for much longer periods than current devices, in such cases dust may become a problem for a number of reasons:

- The build up and subsequent mobilisation of dust in the device may hamper tokamak performance.
- Tritium and Beryllium retention, radioactive and toxic respectively, by dust will lead to radioactive, toxic, breathable dust.
- Tritium retention may lead to unacceptable levels of tritium being carried away from the core and deposited elsewhere in the vessel (tritium is expensive!).
- In the event of water entering the vessel, dust may serve as a catalyst for the decomposition to oxygen and hydrogen creating a risk of explosion [26][27].

Finally in this chapter we outline plasma-wall interactions in a tokamak, and discuss the potential for dust mobilisation and its consequences.

² Tokamak is a transliteration from the Russian acronym for toroidal chamber with magnetic coils

1.5.1 Wall Interactions and the SOL

One source of tokamak dust is due to plasma-wall interactions e.g. sputtering, evaporation, arcing etc. Disruptions are another source of dust, as are Edge Localised Modes (ELMs) found in the high confinement regime (H -mode), ITER's planned operation mode. Disruptions and ELMs lead to large energy fluxes to the torus walls and can create dust and flakes of material [11, 28, 29], work is ongoing to measure dust creation/mobilisation more closely [26]. Due to the nature of tokamak devices a divertor is required to prevent particles diffusing radially onto the walls. The divertor is a solid rail which runs toroidally around the reactor, typically at the bottom. A current is passed through the divertor and the vessel's magnetic fields are drawn into a configuration similar to the second diagram in Fig. 1.2. Figure 1.2 also illustrates the last closed flux surface (LCFS), any plasma within this area is considered to be confined. Any plasma escaping the LCFS will be drawn to the divertor and be removed in what is known as the scrape-off layer (SOL).

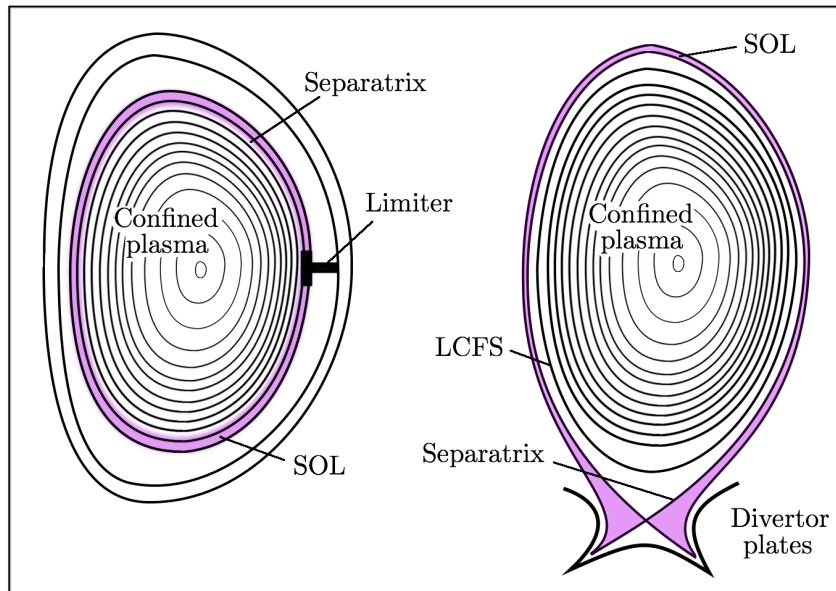


Figure 1.2.: A schematic depicting the Limiter and Divertor. Also indicated are the Scrape-off Layer, Core plasma and Separatrix.

The divertor provides a point of contact between vessel and plasma away from the core and allows control of where the plasma-wall interaction occurs, this allows the management of impurities. Despite the divertors being designed to withstand large energy fluxes, some sputtering and other forms of abrasion occur. Current divertors are made from tungsten, such as in ASDEX-upgrade [30], and carbon fibre composites (CFCs), such as the JET MkI divertor [31]. ITER is currently planned to have beryllium coated plasma facing components (PFCs) and a CFC divertor with an upgrade to a tungsten divertor at a later date. Each of these materials have

potentially significant ramifications for future fusion reactors. Tungsten is primarily used due to its very high melting point and low sputtering yield, this clearly makes it a suitable choice for fusion reactors. However, as tungsten is a high Z (Z is the atomic number) material it will not be completely stripped of its orbiting electrons even at fusion temperatures. This is hazardous for fusion reactors as a relatively small amount entering the core plasma has the potential to radiate away enough of the plasmas energy to cause a disruption. Tungsten is such an efficient radiator that if present in the core in concentrations greater than 1 part per 10^5 , the plasma will be disrupted [32]. In ITER this amounts to a grain of approximately $0.6\mu\text{g}$ (a spherical grain of diameter 0.4mm) finding its way into the core plasma.

Beryllium has the advantage of having a low Z, hence all its electrons are stripped away and we needn't worry about it radiating away power from the core, and relatively high melting point. It may however radiate in the edge plasma where the electron temperature is low enough for it to retain some of its electrons. The disadvantage of beryllium is its toxicity and resulting health implications for humans. In particular, if air-born and breathable, beryllium is highly carcinogenic and may greatly increase the risks of lung cancer. In the event of a reactor breach, beryllium dust could escape into the atmosphere. In addition, next generation tokamaks will focus on deuterium-tritium (D-T) plasmas. Exposure to D-T plasmas is likely to result in tritium retention by the dust as well as activation due to the fast neutrons produced in the fusion process. In effect, we have radioactive, toxic, breathable dust, a health inspector's worst nightmare.

1.5.2 ELMs and Disruptions

The confinement time in tokamaks is described via empirical scaling laws with different scaling laws required for different confinement types. Two important confinement modes are the low and high confinement regimes, L-mode and H-mode respectively [33, 34]. We are not concerned with the specific details of the confinement modes, but note that H-mode is considered to be the most likely candidate for a steady state fusion reaction [35], and will be the confinement mode in ITER. The transition to the H-mode regime is not yet fully understood but in general transport barriers at the plasma edge confine heat/particles in the core and confinement time is improved. As a result, steep temperature and density gradients form close to the plasma edge [36], this leads to a specific type of instability, ELMs [37, 38]. ELMs are short time scale perturbations in the edge plasma, they incur particle and energy losses, lead to a degradation of confinement, and may damage PFCS. There are a number of ELM classifications however, it is sufficient for us to know they exist and regularly deposit energy to PFCS. In next generation devices

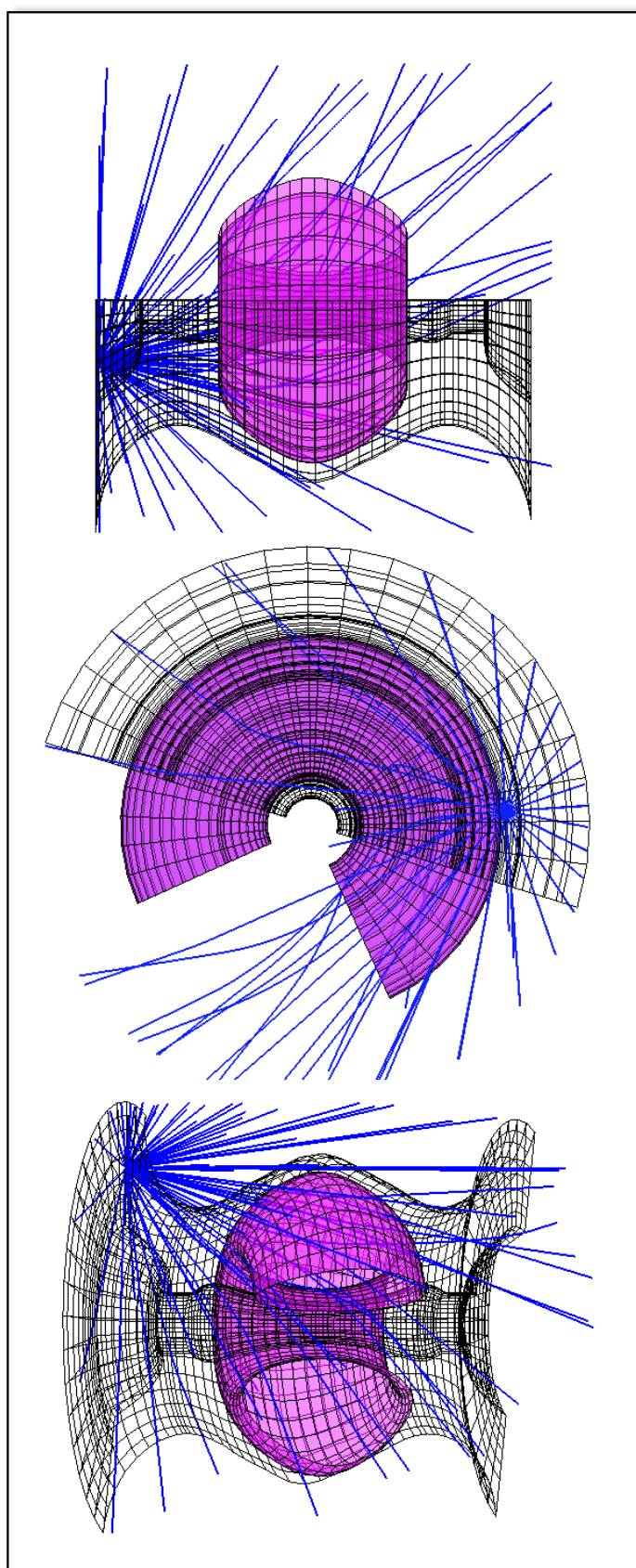


Figure 1.3.: Dust trajectories from a disruption like event in MAST, the purple shaded area represents the core plasma.

like ITER ELMS may impart an unacceptable heat load on the divertor. ELMS also have a serious potential for mobilising impurities and dust from the device walls and divertor. In long term plasma confinement, this liberated dust could be critical.

There are various instabilities that can (and do) occur when trying to confine a plasma magnetically. Whilst we are not concerned here with their specifics, it is important to note that they can lead to a disruption. A disruption is the sudden loss of thermal energy to the walls, this is often followed by termination of the discharge. Disruptions are violent events and mitigation of disruptions if paramount if next generation devices are to be viable. Disruptions transfer large amounts of energy to a small area of the vessel wall over a short time scale and are another source of dust [39]. Figure 1.3 shows simulated trajectories of dust in MAST after a disruption.

1.5.3 Size Distribution

Some work has been done collecting and analysing dust from current tokamaks [28, 29, 40]. The distribution of grain radii found from a variety of tokamaks is $\approx 1.5\mu\text{m}$ with a standard deviation of $\approx 1\mu\text{m}$ [40]. Figure 1.4 shows the distribution of dust grain diameters collected from the bottom of the ASDEX-upgrade tokamak. The Debye length in the SOL of ASDEX-upgrade is $\approx 1 \times 10^{-5}\text{m}$ [41] giving a range of the dimensionless parameter ρ as ≈ 0.1 to 10 .

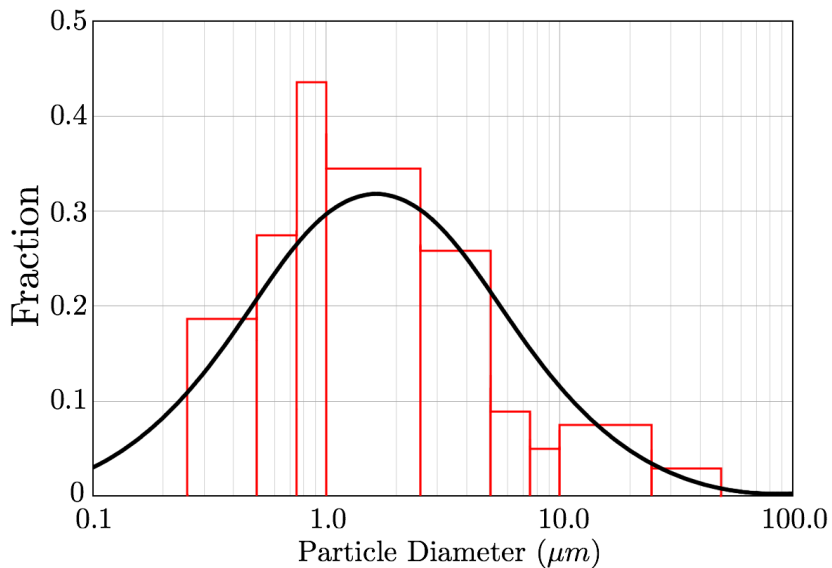


Figure 1.4.: Distribution of dust grain diameters, grains collected from the bottom of the ASDEX-upgrade tokamak. The red boxes indicate the data frequency and the black line is a log normal fit. This figure is reproduced from Fig.3 in [40].

Figure 1.5 shows scanning electron microscope images of material from the TEXTOR tokamak. An assortment of dust shapes and sizes is seen including spheres and flakes with diameters larger than 0.1mm. The spheres are particularly interesting as they indicate that the material has been molten, probably as a result of encountering hot regions of the plasma. We conclude that the range of ρ will be large, potentially > 100 in some of the cooler, edge regions of the SOL. As indicated by the spheres in Fig. 1.5, some material is likely to reach the hotter regions of the plasma.

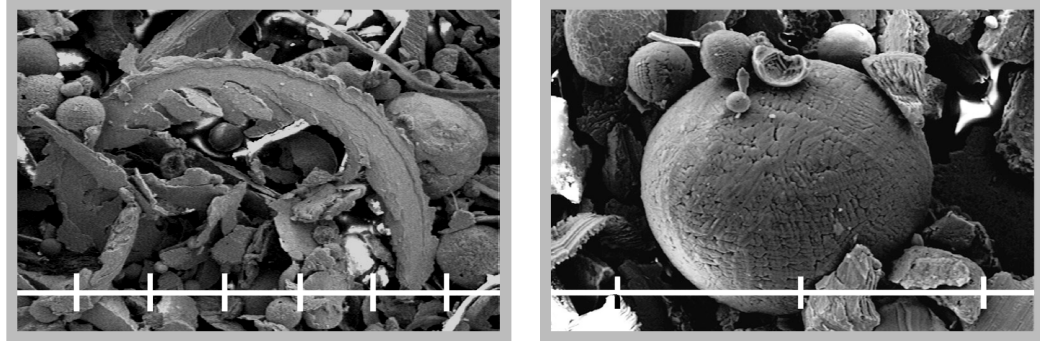


Figure 1.5.: Scanning electron microscope images of material from the TEXTOR tokamak [28].
The marked spaces represent 0.1mm.

1.5.4 Dust in TOKamkS

The Dust in TOKamakS code (`DTOKS`) is our in-house code developed by Martin *et al* [42]. The `DTOKS` code is used to simulate the lifetimes and trajectories of dust grains in a number of tokamaks. As mentioned, Chapters 4 and 5 introduce a charging model for warm ions with a dependence on ρ . Chapter 7 is concerned with implementing this charging model in `DTOKS` and we reserve an outline of the `DTOKS` code until then. Bacharis and Coppins [43] found that the dominant force on a dust grain in a tokamak environment is the ion drag which we now briefly introduce.

1.5.4.1 Ion Drag

The ion drag force on a dust grain has two contributing factors. The first of these is the direct collision of ions onto the grain surface, the collection term. The second is the momentum transferred from ions deflected in the electric field due to the grain but not striking the grain, the scattering term. For small grains this scattering contribution is the dominant one [44, 45]. The ion drag force treatment in `DTOKS` will be outlined in Chapter 7. After implementing our updated charging models in `DTOKS`, it will be the ion drag force that is most heavily effected.

1.6 SUMMARY

It is clear then that dust is present in current tokamaks and will be present in future devices. Currently dust does not appear to hamper performance due to the short time scale over which fusion experiments are conducted. The consequences for long term burning plasmas may only be apparent when ITER comes online. In order to preempt this, and further our understanding of dust transport in current devices, we choose to simulate dust motion in tokamaks. To do this accurately it is critically important to know the potential of the dust in addition to the electromagnetic fields and plasma flows within the device in question. There are further important parameters, such as the plasma's response to the dust and the consequences for the ion drag force, but the floating potential, the potential at which ion and electron currents to the grain balance, is the starting point.

BACKGROUND THEORY - CHARGING OF DUST GRAINS

In the previous chapter we saw that dust and plasma seem to collude within a wide variety of environments. To determine dust behaviour we concluded that knowing the dust potential was paramount. In this section we introduce some necessary background theory and present an overview of the common charging models used to determine grain potential.

First we introduce the Maxwellian distribution, the Debye-Hückel potential and the Boltzmann relation. We then use the Debye-Hückel potential and Maxwellian distribution to investigate the appropriateness of using the Boltzmann relation for the electron density in a planar wall case.

2.1 THE MAXWELLIAN DISTRIBUTION

If a set of particles is left alone and interact via collisions, thermal equilibrium will result. From the self-collisionality a Maxwellian velocity distribution results [46]

$$f^{Max}(v_x, v_y, v_z) = n \left(\frac{m}{2\pi kT} \right)^{3/2} \exp \left[-\frac{m}{2kT} [(v_x - a_x)^2 + (v_y - a_y)^2 + (v_z - a_z)^2] \right]. \quad (2.1)$$

where v_x , v_y and v_z are the components of velocity along the x , y and z axes, m and T the mass and temperature of the species respectively and k is the Boltzmann constant. The components $a_{x,y,z}$ represent flow in a given direction, for any a_x , a_y , $a_z \neq 0$ we have a drifting Maxwellian.

The 1D, stationary Maxwellian velocity distribution is

$$f_{Max}^{1D}(v_x) = n \sqrt{\frac{m}{2\pi kT}} e^{-\frac{mv_x^2}{2kT}} \quad -\infty < v_x < +\infty. \quad (2.2)$$

Taking a stationary Maxwellian, in spherical coordinates the speed of a particle is given by $w = (v_x^2 + v_y^2 + v_z^2)^{1/2}$ and $0 \leq w < +\infty$ hence

$$f^{Max}(w)dw = 4\pi w^2 n \left(\frac{m}{2\pi kT} \right)^{3/2} e^{-\frac{mw^2}{2kT}} dw.$$

The average speed (thermal speed) of a non-drifting Maxwellian is then

$$\langle w \rangle = \frac{1}{n} \int_0^\infty w f^{Max}(w) dw = \sqrt{\frac{8kT}{\pi m}} = \bar{c} \quad (2.3)$$

and the 1-way particle flux

$$\Gamma_x^{Max} = \int_{v_x=0}^{+\infty} f^{Max}(v) v_x dv_x \int_{-\infty}^{\infty} dv_y \int_{-\infty}^{\infty} dv_z = \frac{1}{4} n \bar{c}. \quad (2.4)$$

We will refer to these quantities later.

2.2 THE DEBYE-HÜCKEL POTENTIAL

As we will see in section 2.8.2.1, the most commonly used charging theory does not determine the potential distribution around the grain. A solution to this is to assume a Debye-Hückel (screened Coulomb or Yukawa) potential [47]. Writing the linearised version of Poisson's equation, eqn.(1.4), in spherical coordinates and assuming spherical symmetry

$$\frac{d^2\phi}{dr^2} + \frac{2}{r} \frac{d\phi}{dr} = \frac{1}{\lambda_D^2} \phi. \quad (2.5)$$

The analytic solution to this is the Debye-Hückel potential

$$\phi(r) = \phi(0) \frac{r_d}{r} \exp\left(\frac{r_d - r}{\lambda_D}\right), \quad (2.6)$$

where r_d is the radius of the dust grain. The drawbacks of the Debye-Hückel approach are that the linearisation is unlikely to be valid near the grain as the surface potential will be of order unity, and the assumption of Boltzmann electrons may also be questioned due to the absorbing nature of the grain, see section 2.3. For a small, absorbing grain, $\rho \ll 1$, the Debye-Hückel potential is compared with numerical calculations [48] in Fig. 2.1¹. The agreement is excellent out to $\sim 10^3 r_d$, the Debye-Hückel potential falls off as an exponential whereas the numerical calculations indicate the potential should fall as an inverse square of the radius far from the grain.

2.3 THE BOLTZMANN RELATION

The Boltzmann relation is a link between the electron density, temperature and electrostatic potential. It is applicable providing the dominant forces on the elec-

¹ Fig. 2.1 is reproduced using data from [48]

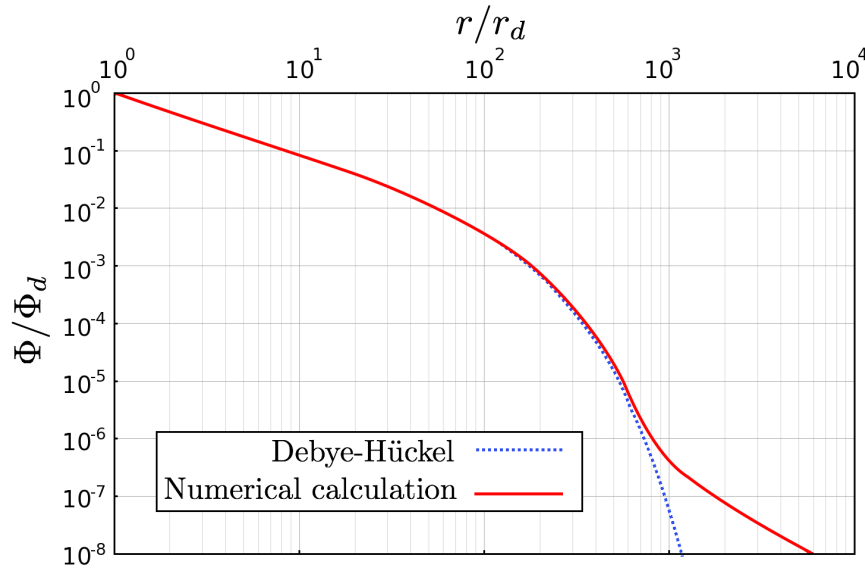


Figure 2.1.: The potential around a small grain, $\rho = 10^{-3}$. Numerical calculations [48] from full orbital motion theory (section 2.8.2.3) are compared with the Debye-Hückel potential. $\rho = r_d/\lambda_D$ where r_d is the dust grain radius.

trons are a pressure gradient and electrostatic repulsion.

Electron momentum conservation gives

$$en_e E + \nabla p_e = 0 \quad (2.7)$$

Using Gauss' law, $E = -\nabla\phi$, and the isothermal ideal gas law, $p_e = n_e k T_e$, we have

$$-en_e \nabla\phi + k T_e \nabla n_e = 0. \quad (2.8)$$

Integrating this we find the Boltzmann relation

$$n_e(x) = n_\infty \exp\left(\frac{e\phi}{k T_e}\right). \quad (2.9)$$

2.4 PLANE RETARDING PROBE

We now use the Maxwellian distribution and the Debye-Hückel potential to investigate the effects of a retarding wall on the distribution of the repelled charge carriers, and examine the approximation of using the Boltzmann relation to describe their density.

In 1D conservation of energy for a charge carrier of charge q gives

$$E = \frac{1}{2}mv^2 + q\phi(x), \quad (2.10)$$

where E is the energy of the charge carrier in the unperturbed plasma. As ϕ increases, the charge carrier is retarded (v is reduced). For a charge carrier to reach a point x it must have $E \geq q\phi(x)$, to reach the wall it must have $E \geq q\phi(0)$ where $\phi(0)$ is the wall potential. Charge carriers with $q\phi(0) > E > q\phi(x)$ can penetrate some way towards the wall before being reflected.

2.4.1 The Flux

The flux, assuming a Maxwellian distribution of velocities, is

$$\Gamma = n_{\infty} \left(\frac{m}{2\pi kT} \right)^{1/2} \int e^{-\frac{mv_x^2}{2kT}} v_x dv_x \quad (2.11)$$

Following Swift and Schwar [49] we change the integral over velocity to an integral over energy, the lower bound becomes E_1 , the minimum energy required for a charge carrier to overcome the potential $\phi(x)$. We have

$$v_x = \pm \left[\frac{2}{m} (E - q\phi) \right]^{1/2}, \quad dv_x = \frac{dE}{m \left[(E - q\phi) \right]^{1/2}}.$$

Integrating over v_y and v_z (as in eqn.(2.2)) the integral becomes

$$\Gamma = n_{\infty} \left(\frac{m}{2\pi kT} \right)^{1/2} \int_{E_1}^{\infty} \frac{e^{-E/kT}}{m} dE. \quad (2.12)$$

Now E_1 is the minimum energy a charge carrier must posses in order to have a finite velocity at the wall. Performing this integration

$$\Gamma(x) = n_{\infty} \left(\frac{m}{2\pi kT} \right)^{1/2} \left[\frac{e^{-E/kT}}{m(-1/kT)} \right]_{E_1}^{\infty} = \frac{n_{\infty}}{4} \left(\frac{8kT}{\pi m} \right)^{1/2} e^{-q\phi(x)/kT}$$

so the flux density at the wall, $\phi(x) = \phi(0)$, is

$$\Gamma_{surface} = \frac{n_{\infty}}{4} \bar{c} e^{-q\phi(0)/kT}. \quad (2.13)$$

2.4.2 The Density

We now look specifically at the electron density as a function of position [49]. Again we assume a Maxwellian velocity distribution. The electrons reflected at some x are counted twice, those being absorbed are only counted once. The limits of A + B are from $-e\phi(x)$ to ∞ and the limits of B are from $-e\phi(0)$ to ∞ .

$$n(x) = n_{\infty} \left(\frac{m}{2\pi kT} \right)^{1/2} \frac{1}{(2m)^{1/2}} \left[\int_{A+B} \frac{2e^{-E/kT}}{(E + e\phi)^{1/2}} dE - \int_B \frac{2e^{-E/kT}}{(E + e\phi)^{1/2}} dE \right].$$

Substituting in $t^2 = (E + e\phi)/kT$

$$\begin{aligned} n(x) &= \frac{n_{\infty}}{\pi^{1/2}} e^{e\phi(x)/kT} \left[2 \int_0^{\infty} e^{-t^2} dt - \int_{[-e(\phi(0)-\phi(x))/kT]^{1/2}}^{\infty} e^{-t^2} dt \right] \\ &= \frac{n_{\infty}}{2} e^{e\phi(x)/kT} \left[1 + \operatorname{erf} \left[\left(\frac{-e(\phi(0)-\phi(x))}{kT} \right)^{1/2} \right] \right]. \end{aligned} \quad (2.14)$$

When $y = -e(\phi(0) - \phi(x))/kT$ is large, $\operatorname{erf}(y) \rightarrow 1$ and we have

$$n(x) = n_{\infty} e^{e\phi(x)/kT}, \quad (2.15)$$

which is the Boltzmann relation. Such a distribution is only true when the drain of electrons by the probe is negligible. Introducing the normalised potential $\Phi = -e\phi/kT_e$, the applicability of the Boltzmann relation is illustrated in Fig. 2.2 (the potential is assumed to be Debye-Hückel for the sake of argument). For the cases of $\Phi = 3.0$ and 8.0 the Boltzmann relation is an excellent approximation. For the lower values of wall potential the Boltzmann relation is not as good, for the case of $\Phi = 0.5$ the Boltzmann relation is wrong by a factor of two at the wall surface as few electrons are reflected.

2.5 SPHERICAL RETARDING PROBE

In the planar case it was assumed that the charge carrier energy could be separated into independent components perpendicular and parallel to the wall, the velocity component parallel to the wall was assumed to play no role. In the case of a sphere or cylinder we need to consider angular momentum.

We include angular momentum, following the notation of Bernstein and Rabinowitz [50], by considering the repelled species around a spherical probe. This is an ideal place to introduce the concept of an ‘effective’ potential which will

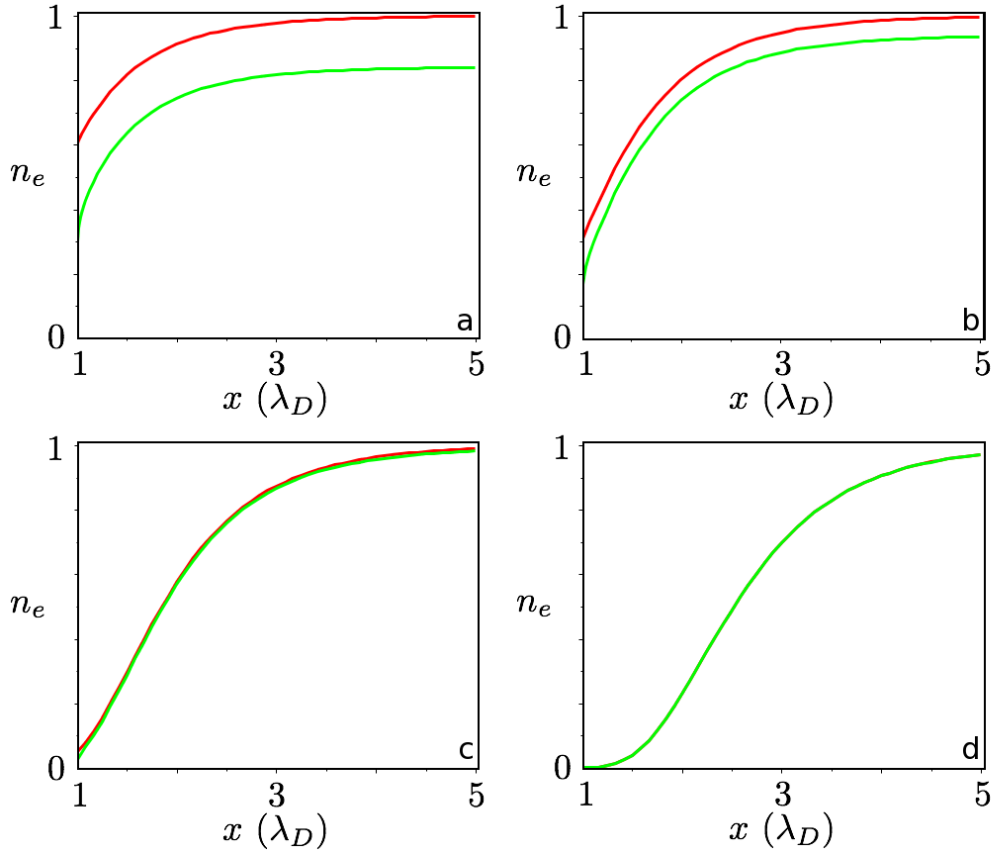


Figure 2.2.: The Boltzmann relation for electron density (red) compared with eqn.(2.14) (green) for a number of wall potentials. a) $\Phi = 0.5$, b) $\Phi = 1.2$ c) $\Phi = 3.0$ d) $\Phi = 8.0$

play a crucial role in the work developed later. Choosing v_r as the radial velocity component and v_θ as the tangential velocity component, the total energy is

$$E = \frac{1}{2}m(v_r^2 + v_\theta^2) + q\phi(r), \quad (2.16)$$

and the angular momentum

$$J = mv_\theta r. \quad (2.17)$$

Combining these equations we have

$$E = \frac{1}{2}mv_r^2 + \underbrace{\frac{1}{2}\frac{J^2}{mr^2} + q\phi(r)}_U \quad (2.18)$$

where U behaves as an effective potential energy. Rearranging this

$$\frac{1}{2}mv_r^2 = (E - q\phi) - \frac{J^2}{2mr^2}. \quad (2.19)$$

For the left hand side to be positive (which it must be) we require

$$(E - q\phi) \geq \frac{J^2}{2mr^2} \quad \text{or} \quad J^2 \leq 2mr^2(E - q\phi). \quad (2.20)$$

This imposes the condition that a retarded particle of total energy E cannot exist at radius r with $\phi(r)$ if the square of the angular momentum is larger than $2mr^2(E - q\phi)$. For a given J , r and $\phi(r)$ the total energy of a particle must have a minimum value

$$E = \frac{J^2}{2mr^2} + q\phi(r) \quad (2.21)$$

for it to reach radius r .

2.6 SPHERICAL ACCELERATING PROBE

For the case of an attracted particle we take an ion in a negative potential, the ion energy is

$$E = \frac{1}{2}mv_r^2 + \frac{1}{2}mv_\theta^2 + e\phi(r).$$

Far from the grain the energy may be distributed in any combination possible between the radial and tangential motion, the total energy E is of course conserved. Another conserved quantity is the angular momentum, eqn.(2.17), and we substitute this into the above equation giving

$$E = \frac{1}{2}mv_r^2 + \frac{J^2}{mr^2} + e\phi(r). \quad (2.22)$$

We may ask what happens when the radial velocity goes to zero. Recalling the effective potential we defined as

$$U = \frac{J^2}{mr^2} + q\phi(r) \quad (2.23)$$

we write eqn.(2.22)

$$E = \frac{1}{2}mv_r^2 + U. \quad (2.24)$$

The above three terms are plotted as a function of v_r in Fig. 2.3, E is of course constant. As expected, a minimum in $mv_r^2/2$, where $v_r = 0$, corresponds to a maxima in the effective potential U . The terms in Fig. 2.3 are plotted as functions of v_r however, this is effectively the same as plotting them as a function of r as v_r is

a function of r . A maximum in the effective potential as a function of radius, $U(r)$, therefore corresponds to the radial velocity going to zero.

W

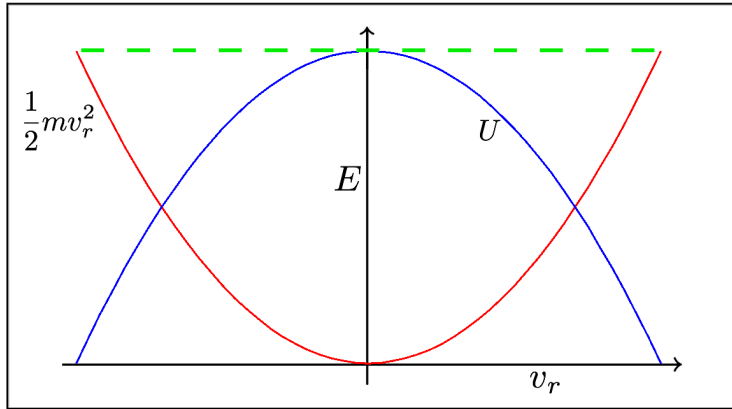


Figure 2.3.: The three terms in eqn.(2.24) as a function of v_r .

We know E and J are conserved and we know that a maximum in the effective potential corresponds to a radial velocity of zero, i.e. a reflected ion. We can now impose a condition on the potential profile by finding turning points in U [48]. Turning points of $U(r)$ can be found by setting the radial derivative of U equal to zero.

Differentiating eqn.(2.23)

$$\frac{dU}{dr} = \frac{-J^2}{mr^3} + q \frac{d\phi}{dr} = 0 \rightarrow J^2 = mr^3 q \frac{d\phi}{dr}. \quad (2.25)$$

Taking the second derivative of eqn.(2.23)

$$\frac{d^2U}{dr^2} = \frac{3J^2}{mr^4} + q \frac{d^2\phi}{dr^2} \quad (2.26)$$

and substituting in J from eqn.(2.25)

$$\frac{d^2U}{dr^2} = \frac{3q}{r} \frac{d\phi}{dr} + q \frac{d^2\phi}{dr^2} \quad (2.27)$$

Assuming $\phi = \kappa r^{-\alpha}$, where κ is a constant, we have

$$\frac{d^2U}{dr^2} = q\kappa\alpha(\alpha-2)r^{-\alpha-2}. \quad (2.28)$$

We are concerned with maxima in the effective potential. Maxima will occur when eqn.(2.28) is positive, this occurs for $\alpha > 2$. These maxima in the effective potential are commonly referred to as absorption radii or potential barriers. They

are called absorption radii as, for a given energy, an ion with angular momentum less than or equal to some critical angular moment, i.e. $J \leq J_{\text{crit}}$ will be absorbed/- collected by the grain and an ion with $J > J_{\text{crit}}$ will not be. The absorption radius concept is illustrated in Fig. 2.4, the radius of collection is not the grazing incidence on the dust grain surface, but the grazing incidence on some imaginary sphere.

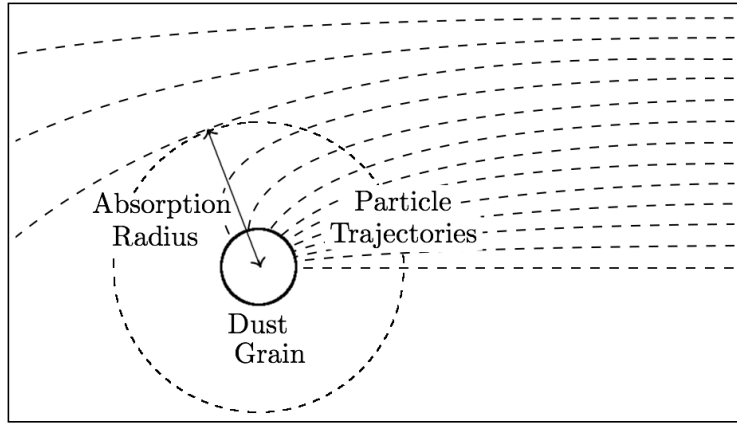


Figure 2.4.: Schematic representation of the absorption radius.

The effective potential U is shown in Figs. 2.5, 2.6 and 2.7 taking the potential to vary more steeply, equal to, and less steeply than $1/r^2$ respectively. In Fig. 2.5, where the potential is steeper than $1/r^2$, absorption radii are observed. We now examine the three graphs of effective potential, starting with Fig. 2.5. The $J^2 = 0$ line corresponds to those ions with $v_\theta = 0$ initially hence they all encounter the grain and the square of their velocity will increase proportionally with the potential. The effective potential curves with maxima are of particular interest, here the ions energy allows it to reach the grain providing it can overcome the effective potential barrier. If it has enough energy it will reach the maximum of the curve with minimum radial velocity, and then be accelerated onto the grain. If its maximum energy is that of, or less than, the effective potential at the maximum, it will be reflected. Fig. 2.6 has two curve types, for low J the curves of U become more negative will decreasing radius and ions "fall down" the effective potential and are absorbed. The U curves tending to positive values with decreasing radius represent the ions that may not have enough energy to reach the grain, depending on the radius of the grain. Finally, Fig. 2.7 contains U curves with minima. These minima do not change any of our definitions but relate again to ions that may not have the necessary energy to reach the grain, these minima occur at small r due to the r^{-2} term in the effective potential, eqn.(2.23). The key point regarding absorption radii is that the ions have the necessary energy to reach the grain but may be reflected purely due to the conservation of angular momentum.

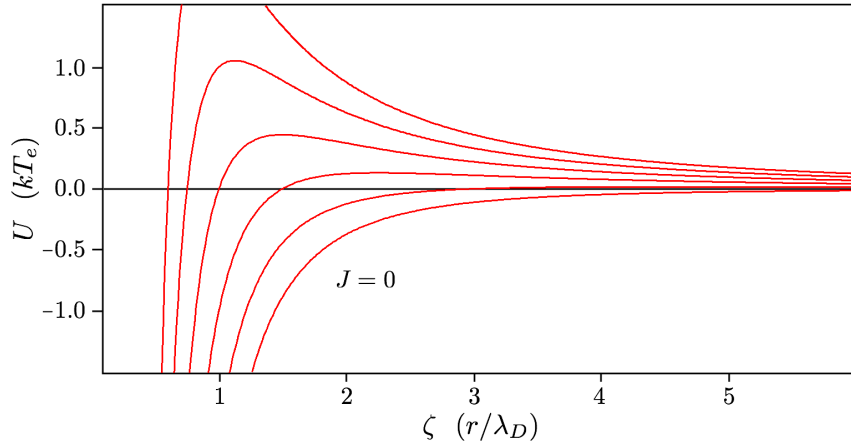


Figure 2.5.: Effective potential, eqn.(2.23), taking $\phi(r)$ steeper than an inverse square.

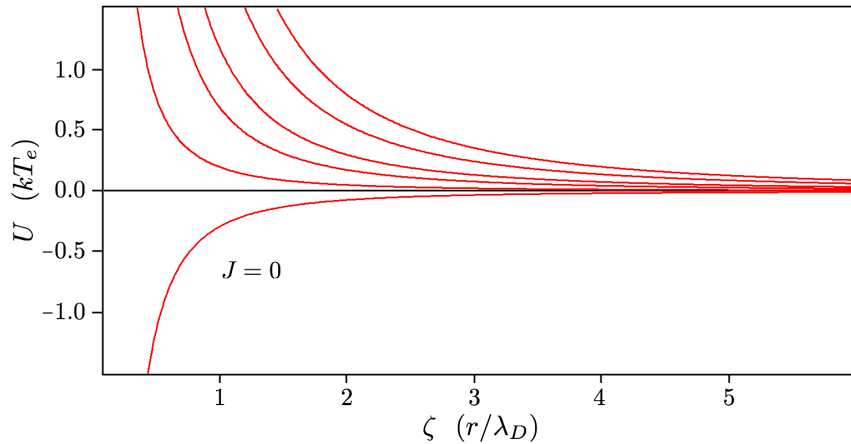


Figure 2.6.: Effective potential, eqn.(2.23), taking $\phi(r)$ proportional to an inverse square.

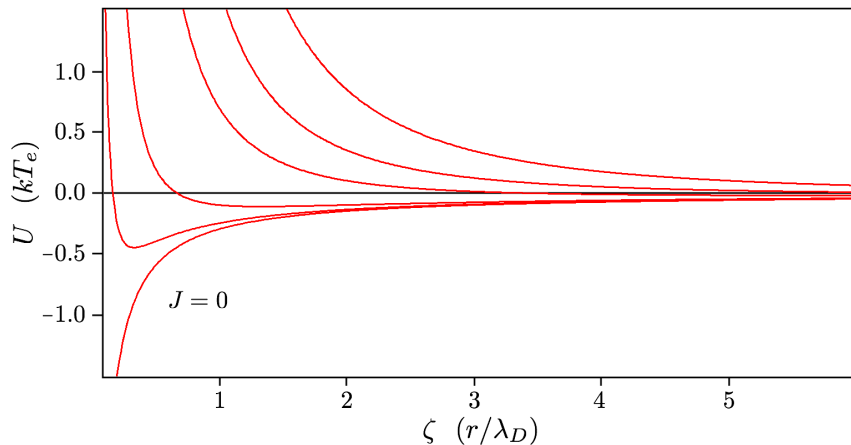


Figure 2.7.: Effective potential, eqn.(2.23), taking $\phi(r)$ to be less steep than an inverse square.

2.7 SHEATH AND PRESHEATH

We have discussed the behaviour of ions and electrons in various potentials, we now look at how and why these potentials form in the first place. The problem of sheath formation at plasma boundaries is one of the oldest problems in plasma physics. Much initial work was done by Langmuir, both individually [51] and with Tonks [52]. This work was extended by Bissell and Johnson [53, 54] however, the problem is still not fully understood [12].

In general, due to the higher mobility of the electrons, a floating wall (by floating we mean there are no external biases and the total current is zero) will be charged negative with respect to the surrounding plasma. Repulsion of electrons from this negative wall leads to a positive space charge region near the wall, the sheath, this sheath shields the main plasma body from the majority of the charge on the negative wall. The sheath width is typically on the scale of the electron Debye length, eqn.(1.5). Ions are continually lost from the sheath to the wall and this leads to a criterion on the ions at the sheath edge, the Bohm criterion.

The condition on the ions is that they enter the sheath with a minimum velocity that cannot be generated by thermal motion. An electric field due to the negative wall penetrates into the plasma to a distance much larger than the sheath width, this region is known as the presheath. The presheath is tasked with accelerating the ions sufficiently to satisfy the Bohm criterion. Tonks and Langmuir essentially included the Bohm criterion in their work in 1929 [52], but it was Bohm who explicitly formulated the condition in 1949 [55]. We now put this verbal description of plasma behaviour into a mathematical formalism following the excellent review article by Riemann [12].

2.7.1 The Bohm Criterion for Cold Ions

Taking a 1D case with a negative wall and assuming the electrons suffer negligible losses and are well described by the Boltzmann relation. In the sheath we have the following set of equations:

Ion continuity	$n_{se}v_{se} = nv$	(2.29)
Ion energy	$E^k = E_{se}^k - e\phi$	
Boltzmann electrons	$n_e = n_\infty e^{-e\phi/kT_e}$	
Poisson's equation	$\frac{d^2\phi}{dx^2} = -\frac{e}{\epsilon_\infty}(n_i - n_e)$	

where the subscript se indicates quantities at the sheath edge.

Introducing/using the normalised quantities

$$\Phi = -\frac{e\phi}{kT_e}, \quad X = \frac{x}{\lambda_D}, \quad E = \frac{1}{2} \frac{mv^2}{kT_e}, \quad (2.30)$$

and normalising the ion/electrons density with respect to the *sheath edge* (but keeping the same symbols for simplicity) we have

$$\left. \begin{array}{l} \text{Ion continuity} \quad n_i E^{1/2} = E_{se}^{1/2} \\ \text{Ion energy} \quad E = E_{se} + \Phi \end{array} \right\} \quad n_i = \left(1 + \frac{\Phi}{E_{se}} \right)^{-1/2} \quad (2.31)$$

$$\begin{aligned} \text{Boltzmann electrons} \quad n_e &= e^{-\Phi} \\ \text{Poisson's equation} \quad \frac{d^2\Phi}{dX^2} &= n_i - n_e. \end{aligned} \quad (2.32)$$

Substituting in the ion and electron densities, Poisson's equation becomes

$$\frac{d^2\Phi}{dX^2} = \left(1 + \frac{\Phi}{E_{se}} \right)^{-1/2} - e^{-\Phi},$$

this can be integrated once analytically using

$$\frac{d}{dX} \left(\frac{d\Phi}{dX} \right)^2 = 2 \frac{d\Phi}{dX} \frac{d^2\Phi}{dX^2}.$$

We now have

$$\begin{aligned} \left(\frac{d\Phi}{dX} \right)^2 &= 2 \left(\left(1 + \frac{\Phi}{E_{se}} \right)^{-1/2} - e^{-\Phi} \right) d\Phi \\ &= 4E_{se} \left(1 + \frac{\Phi}{E_{se}} \right)^{1/2} + 2e^{-\Phi} + C \end{aligned}$$

where C is the constant of integration. Using the boundary conditions $\Phi \rightarrow 0$ and $d\Phi/dX \rightarrow 0$ for $X \rightarrow 0$ then $C = -(4E_{se} + 2)$ hence

$$\left(\frac{d\Phi}{dX} \right)^2 = 4E_{se} \left[\left(1 + \frac{\Phi}{E_{se}} \right)^{1/2} - 1 \right] + 2(e^{-\Phi} - 1). \quad (2.33)$$

The right hand side of the above must be positive for a real solution hence the ion density must be larger than the electron density in the sheath. This is only going to

be an issue for small potentials. Setting the right hand side of eqn.(2.33) to be equal to or greater than zero and Taylor expanding

$$1 + \frac{\Phi}{E_{se}} \geq 1 + \frac{\Phi}{E_{se}} - \frac{1}{2} \frac{\Phi^2}{E_{se}} + \frac{1}{4} \frac{\Phi^2}{E_{se}^2} + O(\Phi^3). \quad (2.34)$$

The above reduces to

$$0 \geq -\frac{1}{2} \frac{\Phi^2}{E_{se}} + \frac{1}{4} \frac{\Phi^2}{E_{se}^2} \rightarrow E_{se} \geq \frac{1}{2}. \quad (2.35)$$

That is, the ions have to enter the sheath with a velocity equal to or greater than $(kT_e/m_i)^{1/2}$. The Bohm criterion is therefore

$$v_x \geq \sqrt{\frac{kT_e}{m_i}}. \quad (2.36)$$

2.7.2 The Bohm Criterion for Hot Ions

The Bohm criterion for hot ions is considerably more involved but has been derived by Harrison and Thompson [56], with a note on the physical meaning by Allen [57]. Here we only state the hot ion Bohm criterion and follow Stangeby [46] for our discussion.

The hot ion Bohm criterion is

$$\int_0^\infty \frac{f_{se}^i(v)}{v^2} dv \leq \frac{m_i}{kT_e},$$

where $f^i(v)$ is the 1D ion velocity distribution at the sheath edge. For monoenergetic ions the integral goes to v_{se}^{-2} and the cold ion Bohm criterion is recovered. Taking the ion velocity distribution to be a top hat with velocities ranging from $(v_{se} - v_{Ti})$ to $(v_{se} + v_{Ti})$, shown in Fig. 2.8, where v_{Ti} is the ion thermal velocity $(kT_i/m_i)^{1/2}$

$$f_{se}^i(v) = \begin{cases} (2v_{Ti})^{-1} & \text{for } v_{se} - v_{Ti} \leq v \leq v_{se} + v_{Ti} \\ 0 & \text{otherwise.} \end{cases} \quad (2.37)$$

The generalised Bohm criterion becomes

$$\frac{1}{2v_{Ti}} \int_{v_{se}-v_{Ti}}^{v_{se}+v_{Ti}} \frac{1}{v^2} dv = \left(\frac{1}{v_{se}^2 - v_{Ti}^2} \right) \leq \frac{m_i}{kT_e} \quad (2.38)$$

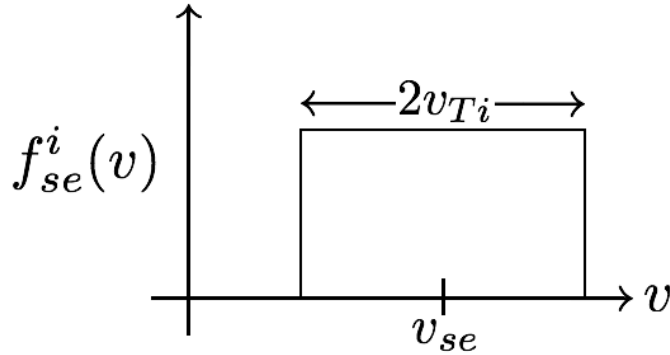


Figure 2.8.: The top-hat distribution function, eqn.(2.37)

so

$$v_{se} \geq \sqrt{\frac{kT_e}{m_i} + \frac{kT_i}{m_i}}. \quad (2.39)$$

There are no stationary or backwards going ions allowed in $f_{se}^i(v)$ as all ions entering the sheath are absorbed. In addition, the generalised Bohm condition is strongly weighted to the slower ions. This is an interesting point, we know from the cold ion case that the ion density must decrease more slowly than the electron density in the sheath [58]. The slower ions in a distribution are the most susceptible to acceleration-rarefaction. The slower ions must be accelerated in the presheath to prevent their having a significant detrimental effect on the ion density under large accelerations in the sheath.

Much work has been done by Riemann [12, 59, 60, 61] with regard to the sheath and presheath. In particular, in [12] Riemann discusses, for the case of warm ions, replacing the critical velocity at the sheath edge by the sound speed

$$v_{se} \geq c_s = \sqrt{\frac{kT_e + \gamma kT_i}{m_i}}, \quad (2.40)$$

γ is the ratio of specific heats. From a fluid point of view, warm ions introduce an additional pressure into the momentum balance, though what to assume for the value of γ is unclear.

2.7.3 Presheath Types

The description of the boundary plasma is not yet complete. The sheath currently ends at some “edge” which cannot be identified with the undisturbed plasma [12]. As seen from eqn.(2.36), ions must enter the sheath region with velocity equal to

or greater than $(kT_e/m_i)^{1/2}$. Typically $T_e > T_i$ and an electric field is required to accelerate the ions before they reach the sheath edge, the term presheath was coined by Hu and Ziering [62] to describe this region. The presheath is assumed to extend over a distance L much larger than the sheath width hence $L \gg \lambda_D = eL$. Taking $x = eX$ we can write Poisson's equation as

$$\epsilon^2 \frac{d^2\Phi}{dx^2} = n_i(\Phi, x) - n_e(\Phi).$$

As ϵ goes to zero the presheath is seen to be quasineutral. Using the ion current density j_i to give an expression for the ion density [12]

$$n_i = \frac{j_i}{E^{1/2}}, \quad j_i = \left(\frac{m_i}{2kT_e} \right)^{1/2} \frac{J_i}{n_\infty}.$$

Equating this with the electron density

$$e^{-\Phi} = \frac{j_i}{E^{1/2}}.$$

Taking logarithms of both sides and differentiating with respect to x yields

$$\frac{1}{2E} \frac{dE}{dx} - \frac{d\Phi}{dx} = \frac{1}{j_i} \frac{dj_i}{dx}. \quad (2.41)$$

Providing the Bohm criterion is not yet satisfied, $E < 1/2$ and

$$\frac{dE}{dx} - \frac{d\Phi}{dx} < \frac{1}{j_i} \frac{dj_i}{dx}. \quad (2.42)$$

Applying the ion energy equation, $E(x) = E(0) + \Phi$, to the presheath and differentiating with respect to position we find

$$\frac{dE}{dx} = \frac{d\Phi}{dx}.$$

Inequality (2.42) can only be satisfied if $dj_i/dx > 0$, i.e. the current density increases towards the sheath edge. Alternatively we can include a retarding force in the presheath so that $dE/dx < d\Phi/dx$, that is the ions gain energy as they approach the sheath edge at a slower rate than the potential increases. These requirements can be satisfied in a number of ways

- The presheath can be “geometric”, that is ion current density increases due to the geometric concentration of ions. Clearly this mechanism is present for dust grains.
- A collisional presheath can be used to introduce friction.

- Ionisation can be employed to both increase the ion current density directly and introduce friction via collisions.

It is interesting to note that in a planar case, ion continuity is not sufficient to satisfy the Bohm criterion as current density remains constant.

2.8 CHARGING MODELS

We have introduced the sheath and presheath and discussed the Bohm criterion and its consequences. A number of charging models are now reviewed with the aim of highlighting the work that has already been done, and what is left to do.

2.8.1 *Allen Boyd Reynolds*

The radial motion theory ABR is named after its creators, Allen, Boyd and Reynolds [63]. The problem is that of a spherical probe in a collisionless plasma of cold ions. The potential of the dust grain, $\phi(0)$, is initially unknown, and the grain is assumed to be floating, $I_e = I_i$. Assuming the ions start at infinity with zero kinetic energy

$$\frac{1}{2}m_i v_r^2 = -e\phi(r). \quad (2.43)$$

Poisson's equation is solved in ABR hence we know the form of the potential everywhere

$$\nabla^2\phi = -\frac{e}{\epsilon_0}(n_i - n_e).$$

The ion current as a function of radius is

$$I_i = 4\pi r^2 n_i(r) v(r) e \quad (2.44)$$

which we rearrange for the ion density

$$n(r) = \frac{I_i}{4\pi r^2 e v(r)}. \quad (2.45)$$

Assuming few electrons reach the grain (the grain is expected to be negative due to the higher mobility of the electrons), and taking the electrons to have a Maxwellian energy distribution due to collisions on a longer time scale than the ion-probe interaction, the electrons density may be well approximated by the Boltzmann relation

$$n_e(r) = n_\infty \exp\left(\frac{e\phi}{kT_e}\right). \quad (2.46)$$

Assuming the electrons to be Boltzmann incurs an error near the grain as we saw in section 2.3, in practise this error is small.

At the grain surface the electron thermal flux is

$$I_e = 4\pi r_d^2 n_\infty e \sqrt{\frac{kT_e}{2\pi m_e}} \exp\left(\frac{e\phi_p}{kT_e}\right), \quad (2.47)$$

the error due to assuming Boltzmann electrons is removed as we are taking a one-way flux.

In spherical coordinates, and assuming spherical symmetry, Poisson's equation is

$$\frac{1}{r^2} \frac{\partial}{\partial r} \left(r^2 \frac{\partial \Phi}{\partial r} \right) = -\frac{e}{\epsilon_0} (n_i - n_e).$$

Substituting eqn.(2.43) into eqn.(2.45) and normalising using $\zeta = r/\lambda_D$

$$\frac{n_i}{n_\infty} = \frac{I_i}{4\pi\zeta^2\lambda_D^2 n_\infty e} \sqrt{\frac{m_i}{2\Phi kT_e}} = \frac{J}{\zeta^2 \Phi^{1/2}}.$$

J is the ion current given by eqn.(2.44) normalised by $4\pi\lambda_D^2 n_\infty e \sqrt{2kT_e/m_i}$. The electron density is

$$\frac{n_e}{n_\infty} = e^{-\Phi}.$$

Substituting the above into poisson's equation

$$\frac{\partial^2 \Phi}{\partial \zeta^2} + \frac{2}{\zeta} \frac{\partial \Phi}{\partial \zeta} = \frac{J}{\zeta^2 \Phi^{1/2}} - e^{-\Phi}. \quad (2.48)$$

The above equation has a “vacuum” solution valid near the object where the right hand side is negligible compared with the left hand side. Setting the right hand side of eqn.(2.48) equal to zero we have

$$\frac{\partial^2 \Phi}{\partial \zeta^2} + \frac{2}{\zeta} \frac{\partial \Phi}{\partial \zeta} = 0. \quad (2.49)$$

A solution to this is

$$\Phi = \frac{A}{\zeta} + B, \quad (2.50)$$

where A and B are arbitrary constants, i.e. a $1/r$ behaviour.

Sufficiently far from the grain the plasma condition, $n_i = n_e$, may be applied. Setting the left hand side of eqn.(2.48) to zero

$$\frac{J}{\zeta^2 \Phi^{1/2}} = e^\Phi \text{ hence } \zeta = \frac{\Phi^{1/2}}{e^{\Phi/2} \Phi^{1/4}}. \quad (2.51)$$

Interestingly, for large ζ , i.e. far from the grain, $\Phi \rightarrow 0$ so $\Phi \propto 1/r^4$. Eqn.(2.51) is plotted in Fig.(2.9) and is seen to be double valued, only the lower value is correct. The turning point is marked, it is $\Phi = 0.5$ which corresponds to the Bohm speed for this cold ion case, i.e. the sheath edge.

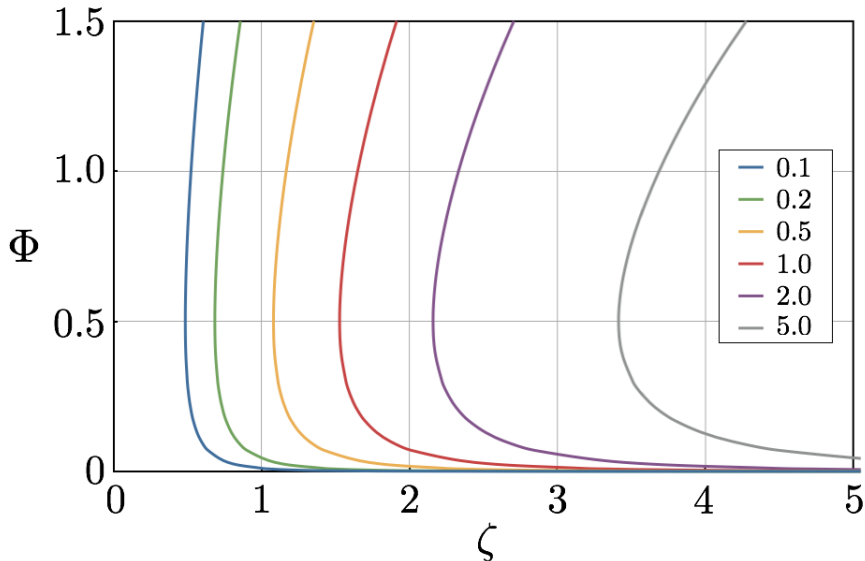


Figure 2.9.: Solution to eqn.(2.51) for various J (indicated on graph). The solution is double valued with the turning points at the sheath edge, $\Phi = 0.5$. $\zeta = r/\lambda_D$ and $\Phi = -e\phi/kT_e$.

Kennedy [64] put finding an appropriate outer boundary condition into a solid form, rather than starting at a large radius where the potential/potential gradient is approximately zero, giving the plasma condition as

$$\frac{J}{\Phi^{1/2}} \gg \frac{4\Phi(2\Phi-3)(2\Phi+1)}{(2\Phi-1)^3}. \quad (2.52)$$

Using eqn.(2.52) to find an appropriate value of potential, this potential is used in eqn.(2.51) to find ζ . Differentiating eqn.(2.51) gives

$$\frac{d\Phi}{d\zeta} = \frac{2\zeta}{J} \frac{\Phi^{3/2}}{\Phi - \frac{1}{2}} \exp(-\Phi). \quad (2.53)$$

This value for the gradient of the potential is used as the outer boundary condition for solving eqn.(2.48). Starting at a point satisfying the plasma condition we integrate eqn.(2.48) inwards towards the grain. The inner boundary condition is given by setting $I_i = I_e$, where I_e is given by eqn.(2.47). Normalising we have

$$\frac{J}{\zeta_d} = \sqrt{\frac{m_i}{4\pi m_e}} \exp(-\Phi_d), \quad (2.54)$$

where the subscript d indicates the value at the dust grain surface.

The solution to ABR is shown in Fig. 2.10. For $\rho \rightarrow 0$ (recall that $\rho = r_d/\lambda_D$) the potential goes to zero, and in the limit of $\rho \rightarrow \infty$ the potential goes to 3.34 [64] (for a hydrogen plasma).

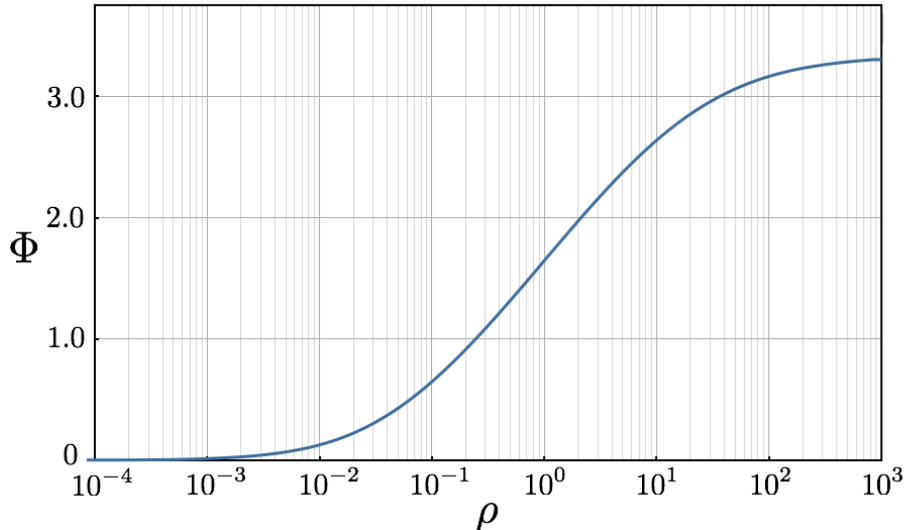


Figure 2.10.: Solution to ABR, $\rho = r_d/\lambda_D$ and $\Phi = -e\phi/kT_e$.

ABR is a pleasing theory thanks to its completeness however, the disregard of ion temperature, and hence angular momentum, makes it of limited practical value. We now turn to the orbital motion theories and consider their strengths and weaknesses.

2.8.2 Orbit Motion Theory

ABR was introduced as it is an elegant and complete theory for describing the potential on and around a spherical object of varying size when the ions are cold. We now introduce the orbital motion approach. The simplest (and consequently

the most widely used) is orbit-motion-limited (OML) which allows the potential of a dust grain to be calculated assuming the ions to have some velocity distribution at infinity, typically Maxwellian. An extension to this is to choose a shifted Maxwellian at infinity to represent a flowing plasma. The problem of absorption radii, introduced in section 2.6, is not encountered in ABR, due to the cold ion assumption, and not accounted for in OML. The final charging theory which we outline is typically referred to as full orbit motion and accounts for finite temperature ions, absorption radii, and solves for the potential everywhere. This then sounds ideal, the drawback being its complexity.

2.8.2.1 Orbital Motion Limited

OML was developed by Mott-Smith and Langmuir in 1926 [65] and, despite its limitations, remains the preferred charging model due to its simplicity. Allen, Annaratone and de Angelis [66] showed that for a negatively charged body residing in a Maxwellian plasma with $T_i \leq T_e$ OML is never valid. In the limit of small dust grains however, the error becomes negligible [67]. We now introduce OML and briefly discuss its limitations. The validity of OML is investigated in §4 and §5, and a modified version presented for large grains.

In summary, the ion and electron current to a spherical (or cylindrical) object are determined, both currents as a function of the potential on the dust grain. For a floating grain the currents are equated and the resulting equality solved (numerically) for the potential. Unlike the more “advanced” charging models we encounter, OML does not involve solving Poisson’s equation hence the potential distribution is unknown. However, OML contains the implied condition that the radial potential varies less steeply than $1/r^2$ everywhere as absorption radii are not accounted for. Our derivation of the OML currents follows Shukla and Mamun [11].

Consider a plasma particle j approaching a dust grain from infinity with impact parameter h_j . The dust grain has radius r_d and potential ϕ_d . For a given velocity we define a grazing orbit, a particle that just touches the grain surface but is not captured. For any impact parameter smaller than that of the grazing orbit, a plasma particle with the same initial velocity will be absorbed. The cross section for collision between a plasma particle and the dust grain is

$$\sigma_j = \pi h_j^2 \quad (2.55)$$

From conservation of angular momentum

$$m_j u_j h_j = m_j v_j r_d, \quad (2.56)$$

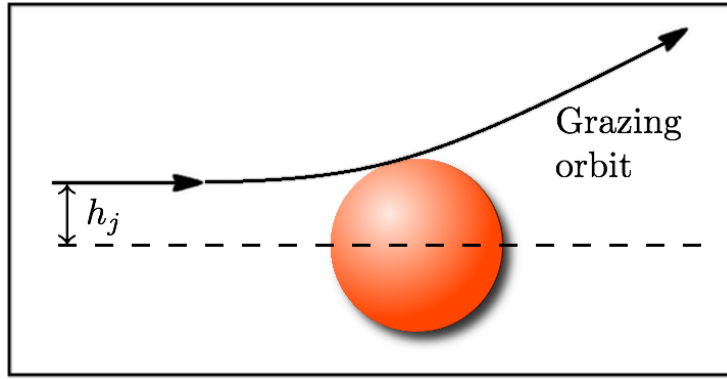


Figure 2.11.: A grazing orbit for a repelled particle with impact parameter h_j .

here u_j is the initial velocity and v_j the velocity immediately after the grazing collision. Conservation of energy reads

$$\frac{1}{2}m_j u_j^2 = \frac{1}{2}m_j v_j^2 + q_j \phi_d. \quad (2.57)$$

Combining eqn.(2.56) with eqn.(2.57) to find h_j , the cross section becomes

$$\sigma_j = \pi r_d^2 \left(1 - \frac{2q_j \phi_d}{m_j v_j^2} \right). \quad (2.58)$$

Taking a velocity distribution $f_j(v_j)$ for both plasma species the current may be written

$$I_j = q_j \int_{v_{j_{min}}}^{\infty} v_j \sigma_j f_j(v_j) dv_j. \quad (2.59)$$

For the attracted species (typically the ions), $v_{j_{min}} = 0$. For the repelled species only those with initial kinetic energy large enough to overcome the grain potential are collected. For the repelled species then

$$v_{j_{min}} = \left(\frac{2q_j \phi_d}{m_j} \right)^{1/2}.$$

Taking $f_j(v_j)$ to be a Maxwellian and assuming spherical symmetry, eqn.(2.59) may be solved analytically. The ion and electron currents are

$$I_i = 4\pi r_d^2 n_i q_i \left(\frac{kT_i}{2\pi m_i} \right)^{1/2} \left(1 - \frac{e\phi_d}{kT_i} \right) \quad (2.60)$$

$$I_e = 4\pi r_d^2 n_e q_e \left(\frac{kT_e}{2\pi m_e} \right)^{1/2} \exp \left(\frac{e\phi_d}{kT_e} \right) \quad (2.61)$$

Introducing the quantity β and recalling Φ

$$\beta = \frac{T_i}{T_e} \quad \text{and} \quad \Phi = -\frac{e\phi}{kT_e}$$

the above currents may be normalised and equated

$$\sqrt{\beta \frac{m_e}{m_i}} \left(1 + \frac{\Phi}{\beta} \right) = \exp(-\Phi). \quad (2.62)$$

The solution to this is shown in Fig. 2.12 as a function of β for a number of ion masses.

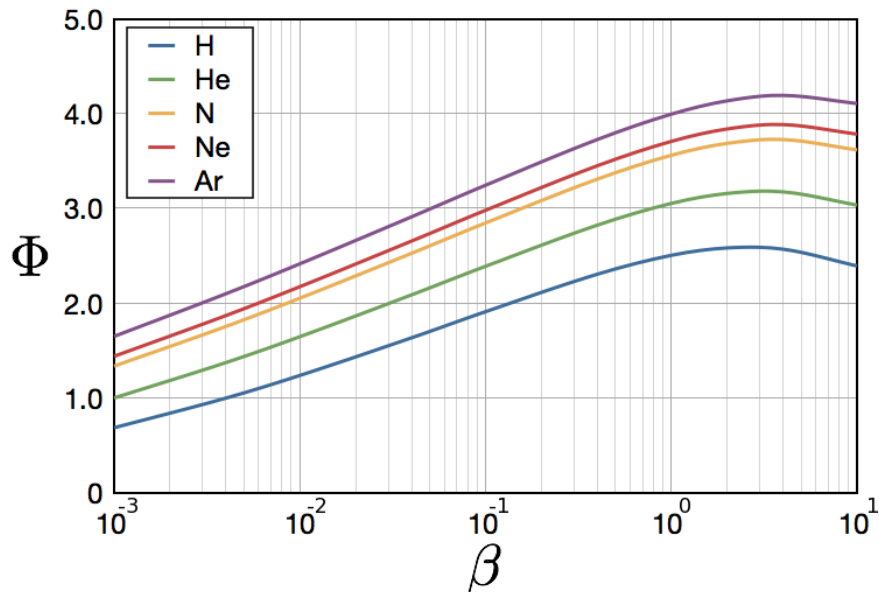


Figure 2.12.: Solution to eqn.(2.62) for various plasma ion species (indicated on the graph). $\beta = T_i/T_e$ and $\Phi = -e\phi/kT_e$.

2.8.2.2 Shifted Orbit Motion Limited (SOML)

To include flow in our charging model we replace the stationary Maxwellian of OML with a shifted Maxwellian velocity distribution. The electrons are still assumed to be well approximated by the Boltzmann relation.

The soml ion current is given by

$$I_i = 4\pi r^2 e n_i \left(\frac{kT_i}{2\pi m_i} \right) \left[F_1(v) - F_2(v) \frac{e\phi}{kT_i} \right] \quad (2.63)$$

where

$$F_1(v) = \frac{\sqrt{\pi}}{4v} (1 + 2v^2) \operatorname{erf}(v) + \frac{1}{2} \exp(-v^2) \quad (2.64)$$

and

$$F_2(v) = \frac{\sqrt{\pi}}{2v} \operatorname{erf}(v),$$

v is the flow speed normalised by $\sqrt{2kT_i/m_i}$. Here we have followed the notation of Shukla and Mamun [11], the work being originally due to Shull [68]. Normalising eqn.(2.63) and equating with the electron current, eqn.(2.60)

$$\begin{aligned} \exp(-\Phi) = & \sqrt{\beta \frac{m_e}{m_i}} \left\{ \frac{\sqrt{2\pi\beta}}{4u} \left(1 + \frac{u^2}{\beta} \right) \operatorname{erf}\left(\frac{u}{\sqrt{2\beta}}\right) \right. \\ & \left. + \frac{1}{2} \exp\left(-\frac{u^2}{2\beta}\right) + \sqrt{\frac{\pi\beta}{2u^2}} \operatorname{erf}\left(\frac{u}{\sqrt{2\beta}}\right) \frac{\Phi}{\beta} \right\}, \end{aligned} \quad (2.65)$$

u is the flow velocity normalised by the ion acoustic speed ($\sqrt{kT_e/m_i}$).

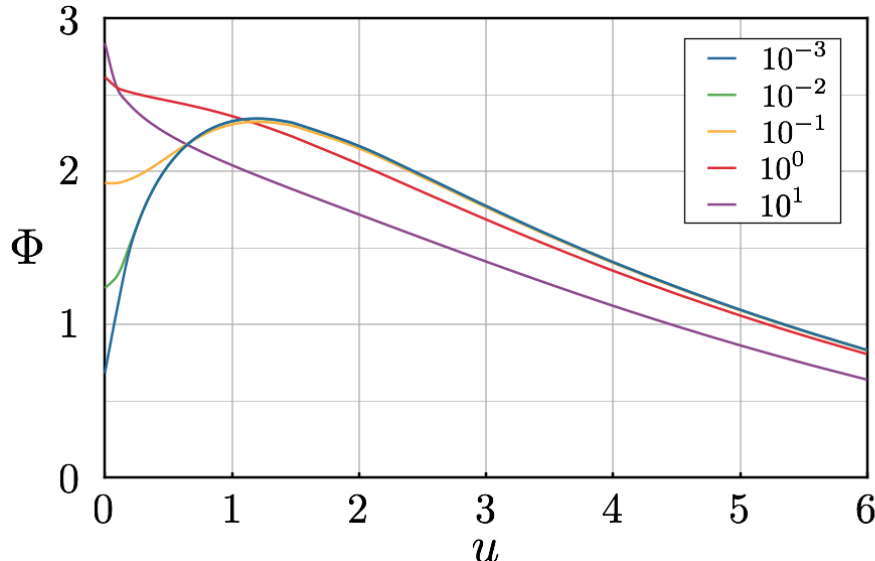


Figure 2.13.: soml floating potential as a function of flow for various β s (indicated on the graph). The ion species is hydrogen. u is the flow speed normalised by $\sqrt{kT_e/m_i}$ and $\Phi = -e\phi/kT_e$.

Equation (2.65) is solved for a range of β in Fig. 2.13, the ion species is hydrogen. It is worth noting that at low flow speeds the potential is strongly dependent on the

ion temperature, with increasing flow the potentials converge to a much smaller range of values as the ion current becomes flow dominated.

2.8.2.3 Full Orbit Motion and Absorption Radii

We have outlined the dominant theory for finding the floating potential, OML, and a radial motion theory for the cold ion case, ABR. OML is appropriate for small grains and has no dependance on object radius and ABR includes radius dependance for cold ions. For grains with $r_d \gtrsim \lambda_D$ and finite ion temperature we are stuck.

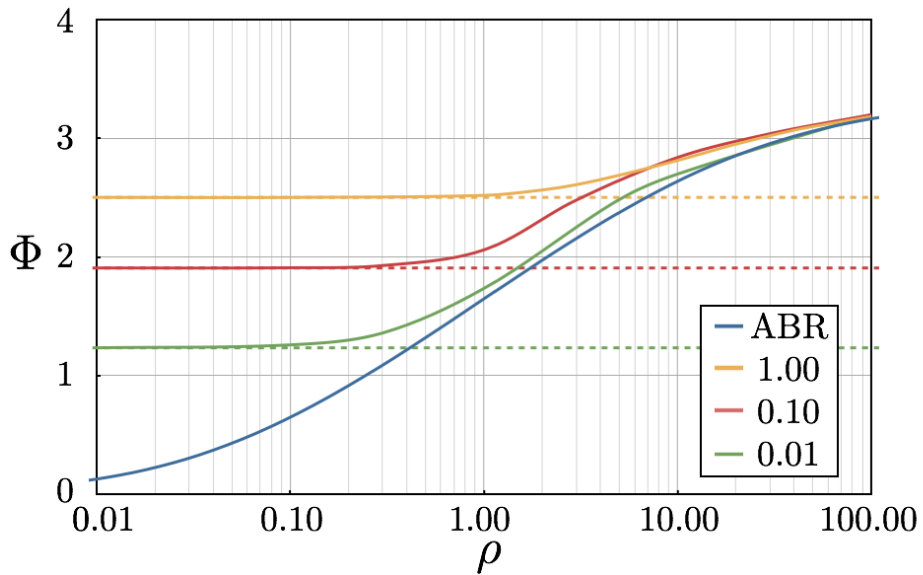


Figure 2.14.: A comparison of OM [48], OML (dashed) and ABR as a function of ρ for various β s (indicated on the graph). $\rho = r_d/\lambda_D$ and $\Phi = -e\phi/kT_e$.

The most complete description of the dust charging problem is given by full orbit motion, OM. As noted earlier, OM is complicated, as such we restrict ourselves to a verbal description of the theory. The full, self-consistent, collisionless Vlasov-Poisson problem has been solved in a number of regimes. The classic paper is that of Bernstein and Rabinowitz [50] following the work of Bohm, Burhop and Massey [69]. Subsequent full Vlasov-Poisson calculations have been done by Laframboise [70], Al'Pert *et al* [71] and Kennedy and Allen [67]. In the latter paper the approach is referred to as orbital motion (OM), the notation we follow.

Ion motion is described everywhere in OM and the Vlasov and Poisson equations are solved in the region $r_d \leq r \leq \infty$, the electrons are assumed to have a Boltzmann distribution. OM also assumes the system to be spherically symmetric and collisionless hence the system conserves energy and angular momentum.² OM finds that for dust grains large compared to the electron Debye length ($\rho > 1$), the ion current

² For a complete description of OM see [67].

is reduced due to absorption radii. Kennedy [48] has recently solved the full OM problem for a Maxwellian distribution of ions, his results are reproduced in Fig. 2.14 for three values of β as a function of ρ . The equivalent values of OML are shown for comparison, we see that $OM \rightarrow OML$ as ρ is reduced, and the departure from OM occurs at different ρ for different β . The OM values approach an asymptotic value for large ρ . The problem with OM is its complexity, values of the floating potential are only available for a limited number of cases.

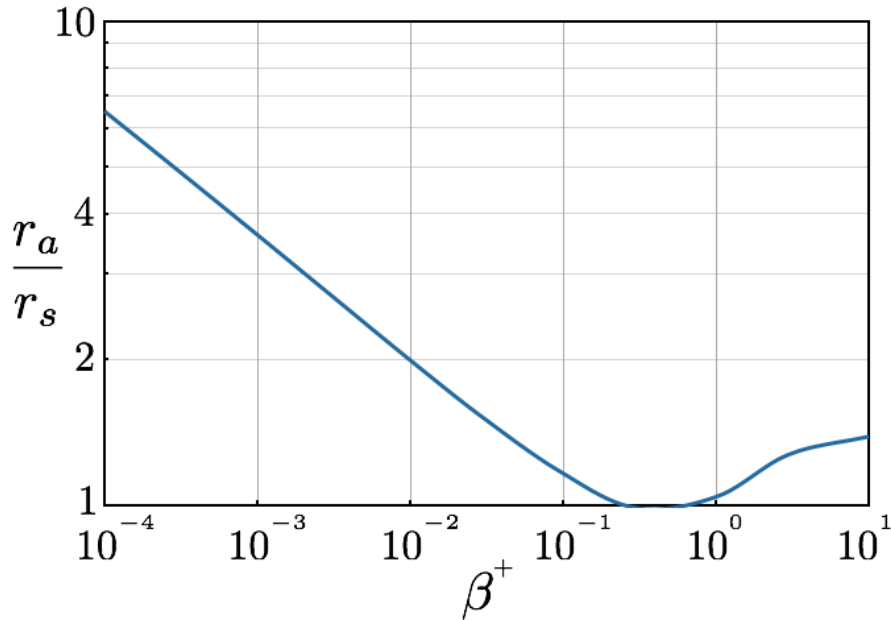


Figure 2.15.: Absorption radius position as a function of ion energy for monoenergetic ions following Bohm, Burhop and Massey [69]. β^+ is the monoenergetic ion energy normalised by kT_e .

As noted, for large ρ ABR and OM approach asymptotes (at least OM appears to). We think of the geometry of the sheath as approaching that of a planar wall, that is, the width of the sheath is small compared with the radius of the grain. As the curvature of the sheath is reduced, the sheath becomes essentially one-dimensional, we refer to this regime as the “thin sheath limit”. We will empirically define the transition to this limit in §4. To get a handle on the absorption radii in this thin sheath limit we refer to the work by Bohm, Burhop and Massey [69]. For the case of large ρ and monoenergetic ions they found the position of the absorption radii as a function of β^+ (β^+ is the monoenergetic ion energy normalised by kT_e). As the sheath is taken to be thin, the sheath radius r_s is effectively the dust radius r_d . The position of absorption radii are shown in Fig. 2.15 as a function of β^+ .³ For low energy ions the absorption radius is multiple dust radii into the presheath

³ Results have been obtained following the derivation by Swift and Schwar [49].

however, for $\beta^+ > 10^{-2}$, the position of the absorption radii are within a single grain radius of the surface. As can be seen from Fig. 2.15, for $\beta^+ \approx 0.01$ ($\beta \approx 0.01$ is the lowest we can reasonably investigate using our code due to numerical heating) the absorption radii are at $\approx 2r_d$, for increasing β^+ they move swiftly closer to the sheath/surface, towards a minimum around $\beta^+ = 0.45$.

SCEPTIC OUTLINE

Much of the simulation work we will present has been performed using the particle-in-cell (PIC) code SCEPTIC. SCEPTIC, Specialised Coordinate Electrostatic Particles and Thermals In Cell, was developed by Hutchinson primarily to investigate probes [72, 73, 74, 75, 76]. Fortunately SCEPTIC is also an excellent tool for studying spherical dust grains and freely available¹ via [77]. In this chapter we introduce the underlying principles of a PIC code and discuss some of the particulars of SCEPTIC.

3.1 PARTICLE-IN-CELL CODES

In a perfect world, we would simulate a plasma by tracking each constituent particle and calculating their interactions with their neighbours. In a tokamak plasma, this amounts to upwards of 10^{18} particles per cubic meter. Solving an n-body problem of this scale with todays computing power is altogether impossible.

A common approach to reduce the computational cost is the PIC method. Individual particles still move freely under the Lorentz force, but the electromagnetic fields are calculated on a grid. Despite this gross simplification of the field quantities, 10^{18} is still a considerably larger number of particles than we are happy to simulate. A typical desktop computer operating at 2.5Gflops would take approximately 10 years to move 10^{18} particles over a single time step. The largest supercomputers in the world (now in the petaflop range [78]), would still take a quarter of an hour to simulate one cubic meter of plasma over a single time step. The plasma frequency in a tokamak is $\gtrsim 5 \times 10^{10} \text{ Hz}$, and the inverse of this is roughly the time step we require. To simulate one second of tokamak operation would take thousands of years, even on todays most powerful computers. In practise we use macro-particles which each represent many ‘real’ particles. As these macro-particles represent a cloud of particles, they occupy a finite volume and have a shape, this is discussed in section 3.1.4.

A typical PIC cycle is shown in Fig. 3.1, from this we see the clear separation between particle motion and field solver. The ion distribution is fed into the code and plays no further role until a solution to a specific equation (Poisson’s equation in our case) is found. When a solution has been found, providing the boundary

¹ At the time of writing.

conditions are sufficiently well defined it will be a unique solution [79], the ions are allowed to move again for a short distance before the process is repeated.

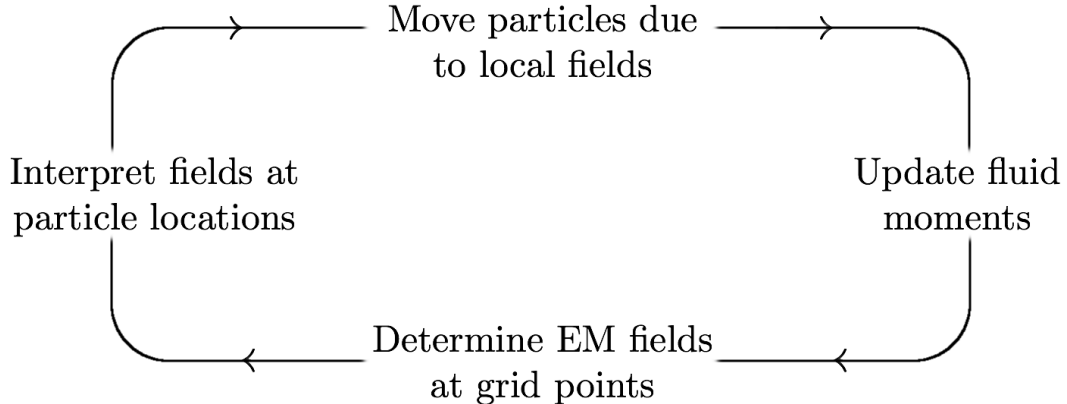


Figure 3.1.: A typical PIC cycle

3.1.1 The Computational Problem

With regard to SCEPTIC we wish to know [80]

- What are the variables
- What equation must be satisfied
- What are the boundaries to this equation (and what happens at these boundaries)

The partial differential equation central to this work is of course Poisson's equation. Starting from Gauss' law

$$\nabla \cdot \mathbf{E} = \frac{\rho_q}{\epsilon_0}, \quad (3.1)$$

where \mathbf{E} is the electric field and $\rho_q = n_i - n_e$, the charge density. Substituting $\mathbf{E} = -\nabla\phi$ into Gauss' equation we have Poisson's equation

$$\nabla^2\phi = -\frac{n_i - n_e}{\epsilon_0}, \quad (3.2)$$

the combination $\nabla \cdot \nabla$ is the Laplacian operator, written ∇^2 , the second order spatial derivative [81].

We require, for some distribution of charge $\rho_q(x, y, z)$, a solution $\phi(x, y, z)$, which satisfies eqn.(3.2) everywhere. By introducing Poisson's equation we have answered

our first and second questions, the variables are the ion and electron densities, $n_i(x, y, z)$ and $n_e(x, y, z)$, and the potential, $\phi(x, y, z)$. In the simulation, the ion density comes directly from the number of ions and the electron density comes from the Boltzmann relation. The field solver is in spherical coordinates with rotational symmetry assumed around some axis. In effect, our potential is only dependent on two spatial quantities, not three i.e. $\phi(r, \theta)$.

The set of equations:

$$\begin{aligned} \text{Ion Equation of Motion} \quad m_i \frac{d^2 \mathbf{x}}{dt^2} &= -Ze\nabla\phi \\ \text{Boltzmann electrons} \quad n_e &= Zn_{i\infty} \exp\left(\frac{e\phi}{kT_e}\right) \\ \text{Poisson's equation} \quad \nabla^2\phi &= -\frac{e}{\epsilon_\infty}(Zn_i - n_e) \end{aligned} \quad (3.3)$$

The ion equation of motion is solved in all three Cartesian coordinates for position and velocity. The following set of normalised quantities are used

$$\begin{aligned} \Phi &= -\frac{e\phi}{kT_e} & \hat{v} &= \frac{v}{\sqrt{ZkT_e/m_i}} \\ \hat{n}_i &= \frac{n_i}{n_{i\infty}} & r_d &= 1 \end{aligned}$$

As the grain radius is set to 1 and the units of velocity are $\sqrt{kT_e/m_i}$, the units of time are the grain radius divided by the velocity

$$\text{Time step} = r_d \sqrt{\frac{m_i}{kT_e}} = \rho \lambda_D \sqrt{\frac{m_i}{kT_e}} = \frac{\rho}{\omega_{pi}}.$$

SCEPTIC therefore resolves things to the ion plasma frequency, this is important for future work with SCEPTIC, discussed in §8. We also note that the unit of velocity, $\sqrt{kT_e/m_i}$, is less than the ion sound speed, but is well defined and independent of position.

Normalising the set of equations in 3.3:

$$\begin{aligned} \text{Ion Equation of Motion} \quad \frac{d^2 \hat{\mathbf{x}}}{d\hat{t}^2} &= \sqrt{Z}\nabla\Phi \\ \text{Boltzmann electrons} \quad \hat{n}_e &= Z\hat{n}_{i\infty} \exp(-\Phi) \\ \text{Poisson's equation} \quad \nabla^2\Phi &= \frac{1}{\lambda_D^2}(e^{-\Phi} - \hat{n}_i) \end{aligned}$$

The remaining question regarding boundaries will be addressed shortly, for now we just note that Poisson's equation is second order in space and will require two boundary conditions. Finally, as our problem must be satisfied everywhere simultaneously, we shall see it reduces to solving a large number of simultaneous equations.

3.1.2 Leap-Frog

We don't concern ourselves heavily with the particle pusher but note that a standard leap-frog method is employed [82]. Newton's second law is solved with the force determined by the field solver.

$$m \frac{dv}{dt} = F, \quad \frac{dx}{dt} = v$$

Applying finite differencing we have

$$m \frac{v_{new} - v_{old}}{\Delta t} = F_{old}, \quad \frac{x_{new} - x_{old}}{\Delta t} = v_{new},$$

with the velocity lagging half a step behind the position. This is shown schematically in Fig. 3.2.

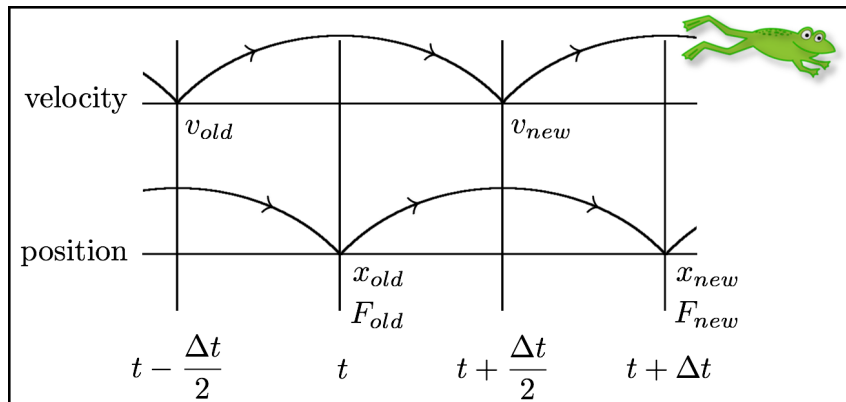


Figure 3.2.: Standard Leap Frog

3.1.3 Computational Mesh and Finite-Difference Scheme

The fields are calculated on a spherical grid with equal spacing in the radius and the cosine of the angle, see Fig. 3.3. The grid is two dimensional and assumed to be rotationally symmetric around the direction of flow.

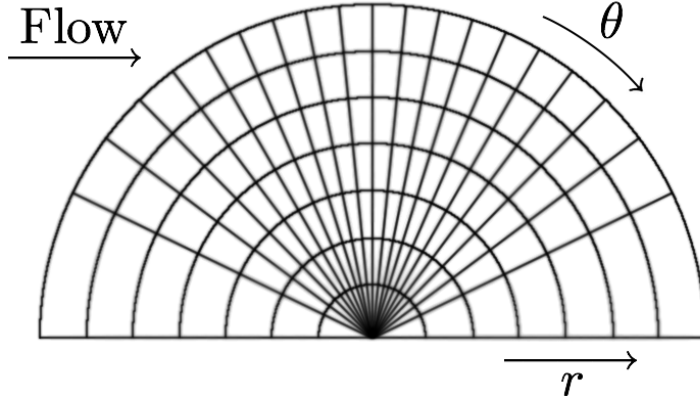


Figure 3.3.: The SCEPTIC grid. Cells at small r have a smaller area than those at large r . There is a lack of resolution along the axis of flow.

The ion equation of motion is solved in 3 cartesian coordinates for the position and velocity, this avoids numerical singularities. From Fig. 3.3 we see the cells at small radii have a smaller area than those at large radii, hence resolution is highest near the grain, we use lots of particles to ensure these smaller cells are adequately populated. Due to the choice of azimuthal grid spacing, the resolution is poorest along the flow axis. This is not ideal for simulating flowing plasmas as we are often interested in the downstream wake formation.

Rather than describing SCEPTIC's finite difference method in detail we choose to outline it using cartesian coordinates, this serves the same purpose but removes what would be a veil of notation. An important difference between the SCEPTIC grid and a cartesian grid is that the SCEPTIC grid cells vary in size, those at smaller radius having a smaller area than those at larger, see Fig. 3.3. This does not represent a problem providing it is properly accounted for.

The quantity $\phi(x, y)$ is represented as a grid made up of discrete points [80]. The grid points are at

$$\begin{aligned} x_j &= x_0 + j\Delta \\ y_l &= y_0 + l\Delta \end{aligned} \tag{3.4}$$

where Δ is the grid spacing and j and l are integers. SCEPTIC's grid points are described by

$$\begin{aligned} r_j &= j\Delta_1 \\ \theta_l &= \arccos(l\Delta_2), \end{aligned}$$

Δ_1 and Δ_2 indicate that the two grid spacings in SCEPTIC are independent of one another. The azimuthal spacing and lack of resolution along the axis of flow is illustrated in table 3.1.

In 2D cartesian coordinates Poisson's equation is

$$\frac{\partial^2 \phi}{\partial x^2} + \frac{\partial^2 \phi}{\partial y^2} = -\frac{\rho_q(x, y)}{\epsilon_0} \quad (3.5)$$

which can be represented using finite differencing. This problem may be solved using a Fourier method or a relaxation method. SCEPTIC employs a relaxation technique called Successive Over-Relaxation (SOR) which we outline in brief following [80].

Rewriting eqn.(3.5) as a diffusion equation

$$\frac{\partial \phi}{\partial t} = \frac{\partial^2 \phi}{\partial x^2} + \frac{\partial^2 \phi}{\partial y^2} + \frac{\rho_q(x, y)}{\epsilon_0}, \quad (3.6)$$

as $t \rightarrow \infty$, $\frac{\partial \phi}{\partial t} \rightarrow 0$ and a solution is “relaxed” towards. Using forward-time centred-space (FTCS) differencing we rewrite eqn.(3.6) as

$$\frac{\phi_{j,l}^{n+1} - \phi_{j,l}^n}{\Delta t} = \frac{(\phi_{j+1,l}^n - 2\phi_{j,l}^n + \phi_{j-1,l}^n)}{\Delta^2} + \frac{(\phi_{j,l+1}^n - \phi_{j,l}^n + \phi_{j,l-1}^n)}{\Delta^2} - \rho_{j,l}$$

Rearranging

$$\phi_{j,l}^{n+1} = \phi_{j,l}^n + \frac{\Delta t}{\Delta^2} (\phi_{j+1,l}^n + \phi_{j-1,l}^n + \phi_{j,l+1}^n + \phi_{j,l-1}^n - 4\phi_{j,l}^n) - \rho_{j,l} \Delta t. \quad (3.7)$$

This is an explicit scheme and, in 2D, only stable for $\Delta t / \Delta^2 \leq 1/4$. Setting $\Delta t = \Delta^2 / 4$ gives

$$\phi_{j,l}^{n+1} = \frac{1}{4} (\phi_{j+1,l}^n + \phi_{j-1,l}^n + \phi_{j,l+1}^n + \phi_{j,l-1}^n) - \frac{\Delta^2}{4} \rho_{j,l}. \quad (3.8)$$

cosine($90 - \theta$)	θ	Difference
0.0	0.00	
0.1	5.74	5.74
0.2	11.54	5.80
0.3	17.46	5.92
0.4	23.58	6.12
0.5	30.00	6.42
0.6	36.87	6.97
0.7	44.43	7.56
0.8	53.13	8.70
0.9	64.16	11.03
1.0	90.00	25.84

Table 3.1.: Spacing in the cosine of the angle.

We can write the above set of linear equations in matrix form

$$\mathbf{A} \cdot \Phi^{(n)} = \mathbf{b}, \quad (3.9)$$

where \mathbf{b} consists of the known information from the boundary conditions. SOR relies on splitting \mathbf{A} into two components, an easily invertible part \mathbf{E} and a remainder \mathbf{F}

$$\mathbf{A} = \mathbf{E} - \mathbf{F},$$

We then re-write eqn.(3.9)

$$\mathbf{E} \cdot \Phi^{(n)} = \mathbf{F} \cdot \Phi^{(n-1)} + \mathbf{b}.$$

An initial guess is chosen for $\Phi^{(0)}$ and we then solve successively. Over relaxation methods work by making an overcorrection to $\Phi^{(n)}$.

3.1.4 Particle Weighting

The charge density is calculated by assigning the ions onto a discrete grid, this is called weighting. SCEPtIC uses Nearest Grid Point or Cloud in Cell weighting, NGP and CIC respectively [82].

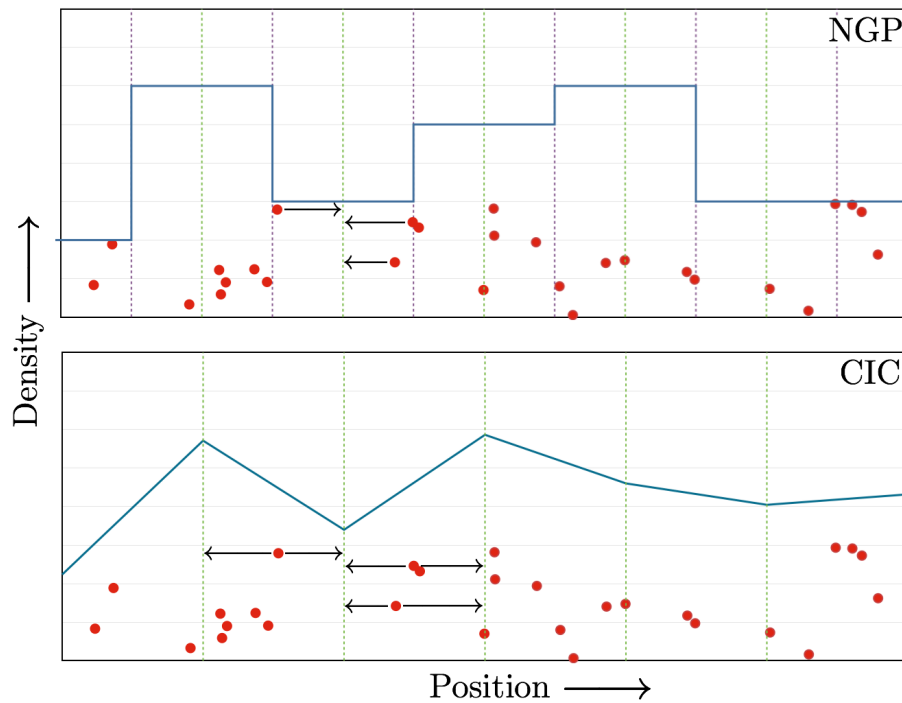


Figure 3.4.: Examples of particle weighting using NGP and CIC

NGP: Also known as zero-order weighting, the number of ions within $\pm\Delta x/2$ of a grid point are assigned to that grid point. This results in rectangular ‘particles’, illustrated in Fig. 3.4, and consequently results in noisy quantities.

CIC: First-order weighting smooths these fluctuations by attributing part of an ion to one grid point and part to another. The fractional contribution to a grid point depends on the ions relative distance from each, this is illustrated in Fig. 3.4.

The CIC method is computationally more expensive but results in smoother field quantities. We choose to use CIC as computational cost is not a priority.

3.1.5 *Instabilities*

As SCEPTIC has been extensively benchmarked [72, 73], we can be relatively confident in it producing sensible results however, there are are number of points to note. Finite size and finite particle numbers mean the current density is noisy, this may lead to heating. Quantities like the ion density can also be noisy, performing multiple runs and taking an ensemble average smoothes this. It is also important to resolve the Debye length to avoid rapid numerical heating, the plasma will self heat until the Debye length is resolved. Even when the Debye length is resolved there is still some heating, this is particularly a problem for low values of β . Results should be consistent when varying the grid spacing, this initially led to some erroneous results in some of our early simulations [83]. Simulations become difficult for very large grains, $\rho \gg 100$, as a simulation domain of a few grain radii requires a small radial mesh spacing to resolve the Debye length. A smaller mesh requires more PIC particles in order to sufficiently populate each cell.

3.1.6 *Inner Boundary*

We noted previously that SCEPTIC requires two boundary conditions. We outline these now starting with the simpler of the two, the inner boundary.

At each time step the grain is assumed to be at the floating potential, this is initially not true as the grain starts at a user defined potential. If the grain is floating then the number of ions striking it is equal to the number of electrons striking it. SCEPTIC counts the number of ions collected each time step, the number is in fact an average over the last N steps to smooth the ion flux. The number of ions is assumed to be the same as the number of electrons being collected and the flux from a 1-way

Maxwellian distribution is used to relate the electron flux to the potential of the grain.

$$I_i = I_e = 4\pi r_d^2 n_\infty e \left(\frac{kT_e}{2\pi m_e} \right)^{1/2} \exp\left(-\frac{e\phi}{kT_e} \right).$$

This is solved for the grain potential, with the ion flux being the number of ions striking the grain per time step. The potential that results is used as the inner boundary condition and, upon reaching steady state, produces a self-consistent floating potential. Providing the radial mesh spacing is sufficiently smaller than λ_D , no problems occur as the sheath is resolved [73].

3.1.7 Outer Boundary

The outer boundary in SCEPTIC is considerably more complex than the inner. When $\lambda_D > r_d$ the electric field varies on the length scale of the dust grain. To resolve the electric field we require many cells per Debye length and it becomes computationally expensive to resolve an appropriate number of Debye lengths. Ideally, the simulation should be large enough to resolve far enough away from the grain to allow the potential to vanish, we could then use $\Phi = 0$ as the outer boundary condition. For large Debye lengths (small grains), the potential at the outer boundary may be a significant fraction of the grain potential and hence the ion density will differ significantly from n_∞ . SCEPTIC handles the outer boundary in the following way [73]:

- The potential at the outer boundary is found by solving an approximate shielding equation outside the computational domain.
- Ions to be injected are chosen at random from a shifted Maxwellian distribution at infinity. The injected particles are “moved” through this approximate potential outside the computational domain.
- The density at infinity is deduced from the flux of ions into the domain via an analytic relation.

If there is a significant potential at the outer boundary, injecting an unperturbed, distant distribution is not sufficient. The potential at the outer boundary could be treated as a ‘step’ in the energy of the incoming ions at the outer boundary, assuming the ions to have been radially accelerated through some $\delta\Phi$, and simply increment the normal component of their velocity appropriately. Hutchinson finds such an approach to be inadequate [73], this may be due to the presence of absorption radii outside the computational domain. As we will see in §4, providing

the potential at the boundary is small, an OML approach outside the computational domain is probably quite sufficient.

3.1.7.1 Approximate Shielding Equation

As seen in section 2.2, a non-absorbing point charge gives rise to the Debye-Hückel potential. Far from the grain the Debye-Hückel potential falls as an exponential asymptotic decay, we saw in Fig. 2.1 that, if the grain has finite size and is absorbing, this is incorrect.

Accounting for ion absorption results in a modified form of Debye shielding. The electrons remain Boltzmann as they are strongly repelled and hence suffer little depletion. If we consider a point far from the grain, the cross in Fig. 3.5, and examine the density perturbation due to absorption by the grain, the ion phase space is unpopulated in regions whose orbits, when tracked backwards, intercept the grain [73]. In other words, the unpopulated orbits all have their velocities directed away from a solid angle towards the grain, the three ions indicated by the arrows in Fig. 3.5 represent ions that will be ‘missing’. The actual angle is relatively unimportant, the main point is that the solid angle it subtends is inversely proportional to the square of the distance to the grain. Using this argument Hutchinson introduces a version of Poisson’s equation including an ion depletion term. Starting with the normalised version of Poisson’s equation

$$\nabla^2 \Phi = \frac{1}{\lambda_D^2} \left(e^\Phi - \frac{n_i}{n_\infty} \right).$$

The potential at the boundary is small so the exponential may be expanded, $e^\Phi \rightarrow 1 + \Phi$

$$\nabla^2 \Phi = \frac{1}{\lambda_D^2} (1 + \Phi - (1 - \delta n)) = \frac{\Phi}{\lambda_D^2} + \frac{\delta n}{\lambda_D^2}$$

where δn is the density perturbation due to the absorbed ions. Taking $\delta n = a/r^2$, where a is a constant of proportionality representing the ion density depletion due to

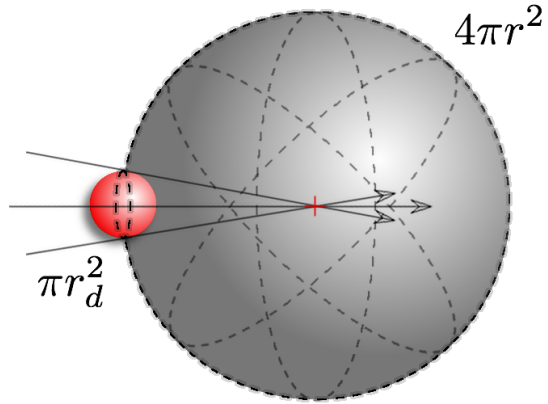


Figure 3.5.: A schematic illustrating ions, indicated by the three arrows, which will be missing in the phase space far from the dust grain, the red sphere.

absorption², Hutchinson's modified shielding equation outside the computational domain is

$$\nabla^2 \Phi - \frac{\Phi}{\lambda_D^2} = \frac{a}{r^2}.$$

Taking the boundary conditions $\Phi(r_b) = \Phi_b$ and $\Phi(\infty) = 0$ this can be solved analytically³. Ultimately the derivative of the potential (with respect to radius) is found from this solution, this is then used as the outer boundary condition.

3.1.7.2 Particle Rejection

In essence, the particle re-injection scheme chooses a random ion from a shifted Maxwellian distribution at infinity. Using the analytic solution to the approximate shielding equation, described above, a test is performed on the ion to determine if it reaches the computational domain i.e. does it encounter an absorption radius outside the domain. Providing the ion reaches the outer boundary of the simulation domain, it is injected with the appropriate position and velocity. If the ion does not reach the computational boundary, it is discarded, a new ion is randomly selected, and the test repeated. The subtleties and nuances of applying this approach correctly can be found in [73].

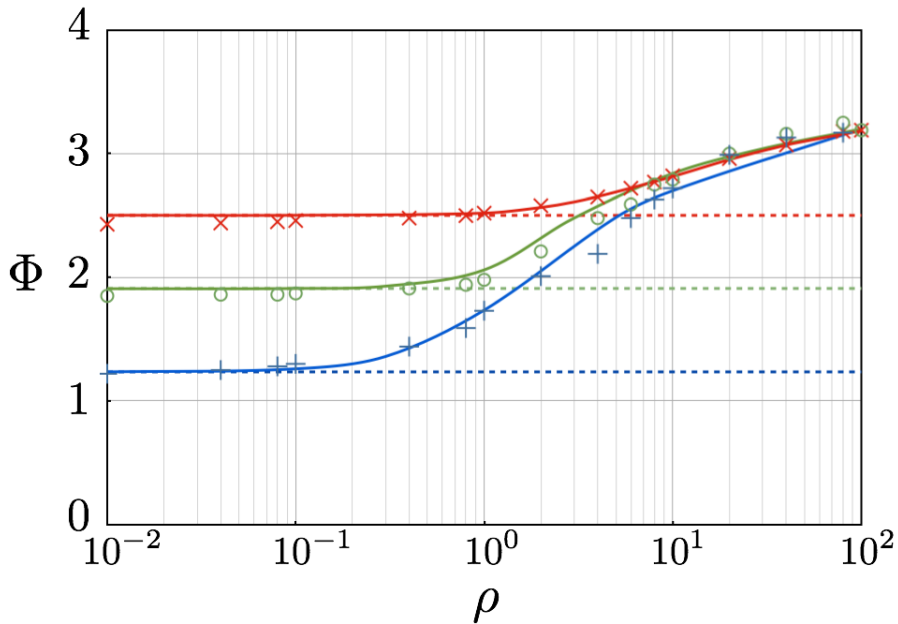


Figure 3.6.: Simulation values of the floating potential for $\beta = 0.01$ (blue), 0.10 (green) and 1.00 (red) for a hydrogen plasma. The solid curves are from OM theory and the dotted horizontal lines the corresponding OML values. $\rho = r_d/\Lambda_D$ and $\Phi = -e\phi/kT_e$.

² eqn.(7) of [73]

³ eqn.(8) of [73]

3.1.7.3 Density Calculation

The number of ions in the simulation is fixed. If we specify the ion density as a boundary condition we require an appropriate flux into the domain each time step. If this flux does not match the loss rate of the ions in the simulation, the number of simulated ions will fluctuate. To avoid this we inject an ion whenever one is lost (via either boundary) and calculate the ion density at infinity using the OML ion flux, eqn.(2.63), given below for reference

$$F_i = 4\pi r^2 n_{i_\infty} \left(\frac{kT_i}{2\pi m_i} \right) \left[\frac{\sqrt{\pi}}{4v} \left(1 + 2v^2 + 2\frac{\Phi}{\beta} \right) \operatorname{erf}(v) + \frac{1}{2} \exp(-v^2) \right].$$

3.1.8 Benchmark

As noted, `SCEPTIC` has been well benchmarked and so we have confidence in our results. As we will be primarily concerned with the floating potential we benchmark `SCEPTIC` against the OM theory. OM results for the floating potential are only available for hydrogenic plasma in the range $\rho = 0.01 \rightarrow 100.00$, and for the specific temperature ratios of $\beta = 0.01, 0.10$ and 1.00 [48]. As seen in Fig. 3.6, the agreement between `SCEPTIC` and OM is excellent over the whole range of ρ for each β .

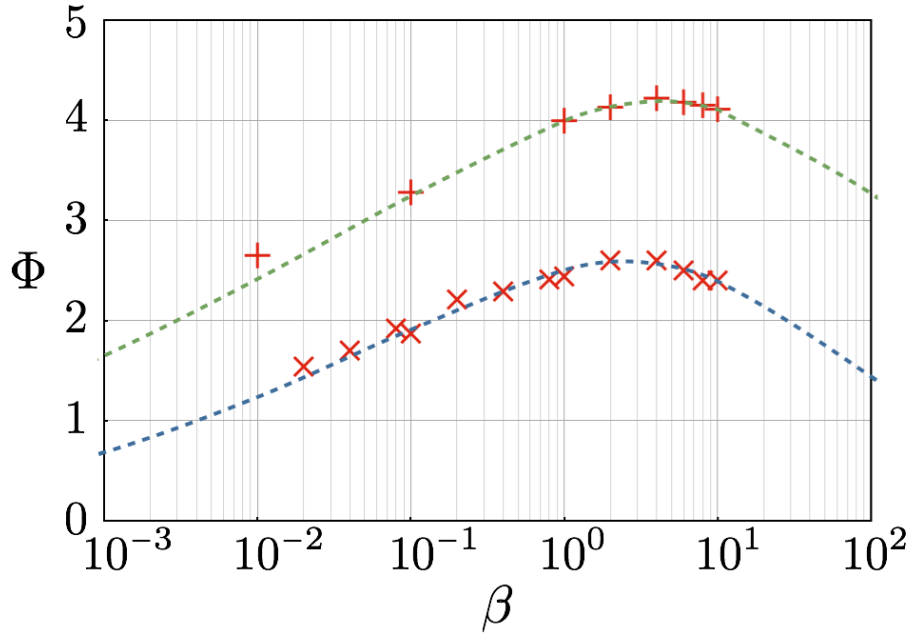


Figure 3.7.: The OML potential as a function of β . The top line is the OML result for argon and the bottom line for hydrogen. `SCEPTIC` values are also shown. $\Phi = -e\phi/k_B T_e$ and $\rho = 0.04$.

SCEPTIC encounters numerical instabilities for low ion temperatures, particularly when ρ is small ($\lesssim 0.1$). For $\beta \lesssim 1.0$ problems are also encountered for particularly large dust grains ($\rho \gtrsim 60$), this is attributed to difficulties in sufficiently resolving the sheath due to the small Debye length. The instabilities may be managed to an extent by careful parameter selection. OM is the most rigorous theory available and the excellent agreement in Fig. 3.6 between theory and simulation indicates that SCEPTIC may be used with confidence in the parameter range we are interested in.

For each value of β three regions are identifiable in Fig. 3.6. For low ρ SCEPTIC (and OM) reproduce the corresponding OML values closely. At some $\rho(\beta)$ the SCEPTIC curves depart from their respective OML values and enter a transition stage. The magnitude of the potential increases with a logarithmic dependence on ρ up to some value, typically around $\rho = 50$, when the gradient tends to zero. The potentials then approach some asymptotic values similar to that predicted by ABR. We refer to these three regions as the OML limit, the transition region and the thin sheath limit respectively. In ABR the thin sheath limit for a hydrogenic plasma is $\Phi = 3.34$. For OM calculation becomes difficult for large ρ [48] however, values for the floating potential appear to approach a limiting value around $\Phi = 3.2$ for the limited number of cases available.

In addition to reproducing the OM results accurately, for small particles SCEPTIC reproduces the OML potential over a large range of β s. This is not only true for hydrogenic plasma but for each species investigated, as shown in Fig. 3.7.

LARGE GRAINS IN A STATIONARY PLASMA

We introduced the orbital-motion-limited (OML) charging model in Chapter 2 and saw that the OML floating potential depends on the ion to electron temperature ratio and the plasma ion species. In reality, the floating potential also depends strongly on the size of the dust grain. Using the PIC code described in the previous chapter, dust is simulated in a fully ionised, collisionless plasma, the floating potential investigated, and expressions provided allowing fast and accurate prediction of the floating potential as a function of ion temperature, ion species and radius [86]. We then develop a modified version of OML for use when $\rho \gg 1$ and discuss its applicability.

4.1 NUMERICAL FITS TO THE FLOATING POTENTIAL

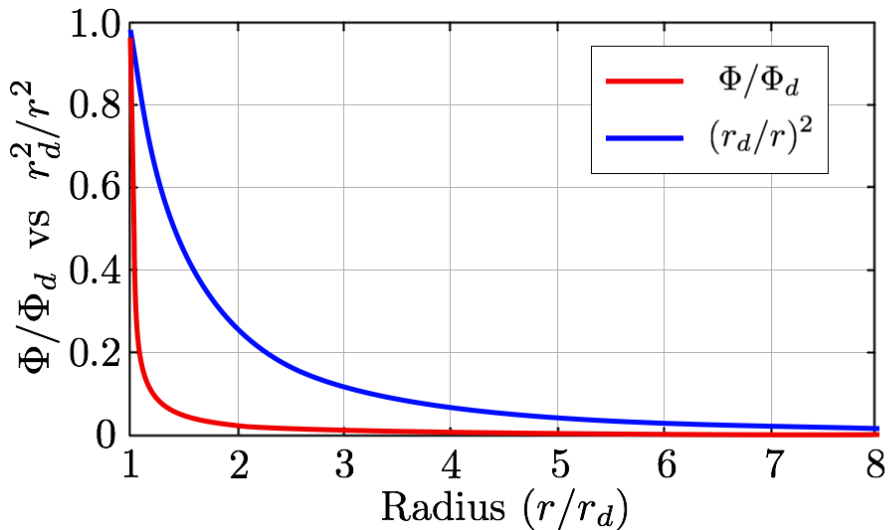


Figure 4.1.: The potential from SCEPTIC compared with $1/r^2$ testing the condition (4.1). $\beta = 0.2$, $\rho = 80$.

The ion current is only orbit-motion-limited if no ions encounter absorption radii before striking the dust grain [70]. We saw in section 2.6 that if the potential falls faster than $1/r^2$ absorption radii will be present. For a Maxwellian plasma, the condition for OML to be valid everywhere may be written [67]

$$\frac{\Phi(r)}{\Phi_d} > \frac{r_d^2}{r^2}. \quad (4.1)$$

We see the effects of the absorption radii in the OM results, the normalised potential increases with increasing ρ as absorption radii reduce the ion current. Using SCEPTIC we look at the radial potential for a large grain in Fig. 4.1. The potential is compared with r_d/ρ^2 , as in inequality (4.1), and we see OML is not valid.

4.1.1 Departure from OML

We begin by investigating the departure of the simulation floating potentials from OML. For a range of β , Fig. 4.2 shows the departure of the simulation floating potential from that of OML as a function of ρ ; ion temperature is seen to play a critical role. It is immediately apparent that the higher the value of β , the more reliable OML is at higher ρ , at $\rho = 100$ the case of $\beta = 10$ is still within 10% of the OML value. The reason for this is a much smaller fraction of the ion distribution function encountering absorption radii as β is increased, this will be addressed more thoroughly later in the chapter.

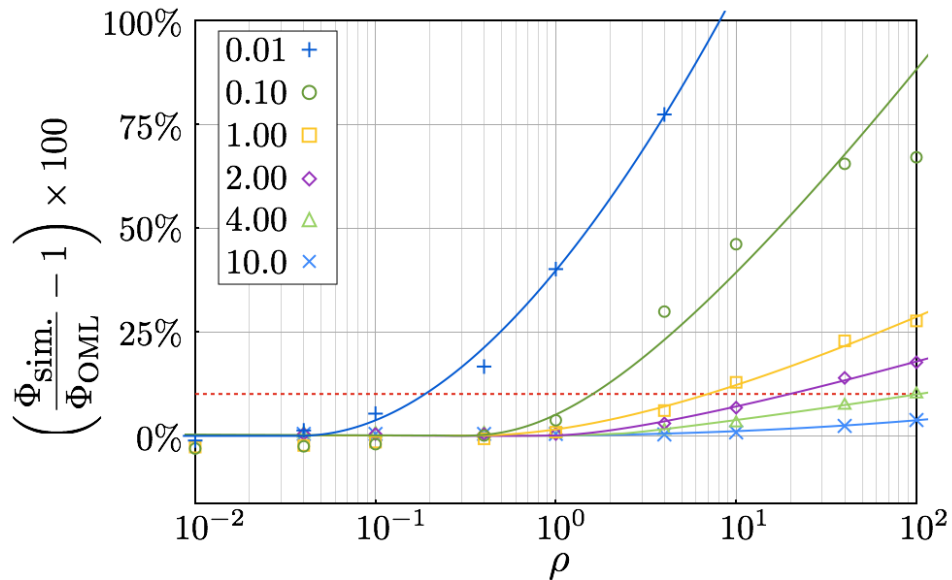


Figure 4.2.: The % difference between the floating potential from simulation ($\Phi_{\text{sim.}}$) and OML, a range of β are shown (indicated on the graph). The red, dashed line indicates a 10% departure, the solid lines indicate the data trend. $\rho = r_d/\lambda_D$.

4.1.2 Three Potential Regions

Recalling section 3.1.8, for each value of β we identified three regions of behaviour of the potential. For low ρ SCEPTIC (and OM) reproduce the corresponding OML values closely. At some $\rho(\beta)$ the SCEPTIC curves depart from their respective OML

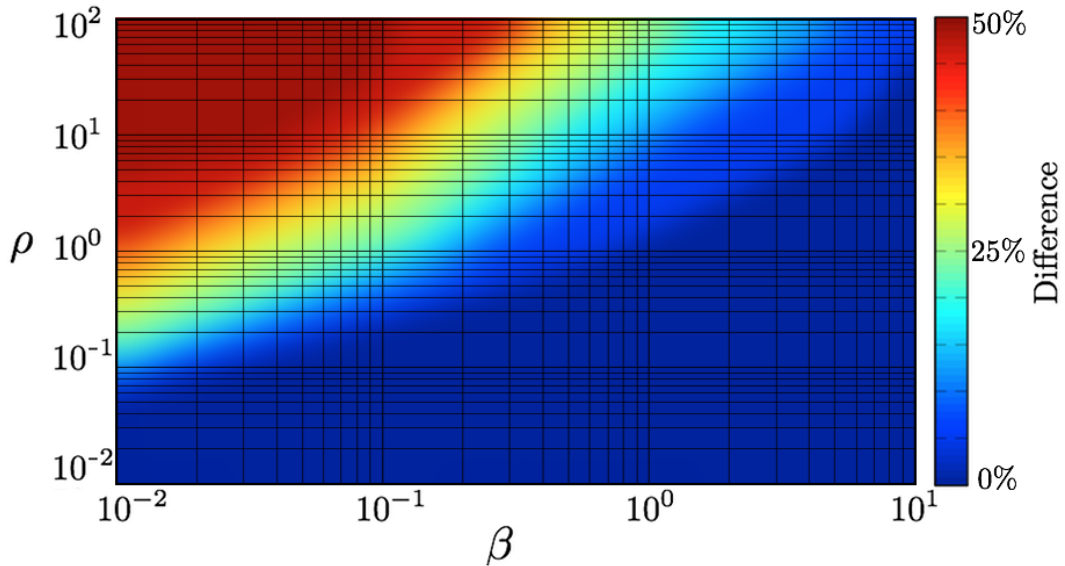


Figure 4.3.: β and ρ parameter space showing the difference between potential from simulation and OML, a range of β are shown. $\rho = r_d/\lambda_D$ and $\beta = T_i/T_e$.

values and enter a transition stage. The magnitude of the potential increases with a logarithmic dependence on ρ up to some value, typically around $\rho = 50$, when the gradient tends to zero. The potential then approaches some asymptotic value similar to that predicted by ABR. We refer to these three regions as the OML limit, the transition region and the thin sheath limit respectively. The surface plot in Fig. 4.3 shows the percentage difference between simulation and OML for a range of β and ρ , the departure from OML clearly depends on β and ρ .

4.1.3 Asymptotic Limit of the Floating Potential

Figure 4.4 indicates the asymptotic nature of the floating potential for large grains. Few simulations have been performed for $\rho > 100$ due to the computational cost and stability, see section 3.1.5. We saw in Fig. 2.12 that the potential encounters a maximum at $\beta \approx 2$ in the OML theory, this is due to the ion current being dominated by the potential when the ion temperature is low, and by the thermal ion flux when the ion temperature is high. This is also found to feature in the non-OML region (large dust grains), though the peak is less pronounced. The case of $T_i > T_e$ ($\beta > 1$) is less frequently encountered than $T_e > T_i$ but is found in the edge plasmas of Tokamaks.

For $\beta \leq 2$ the dependence of the potential on β in the thin sheath limit is weak and is excluded from the following expression, the result is a simple scaling with the mass of the ion species (ion temperature will be included later in the chapter),

this scaling is found to be proportional to $\frac{1}{2} \ln A$ where A is the mass number. The transition to the thin sheath limit happens at $\rho \approx 50$ for the low β case and it is more appropriate to use a single value than a complicated expression.

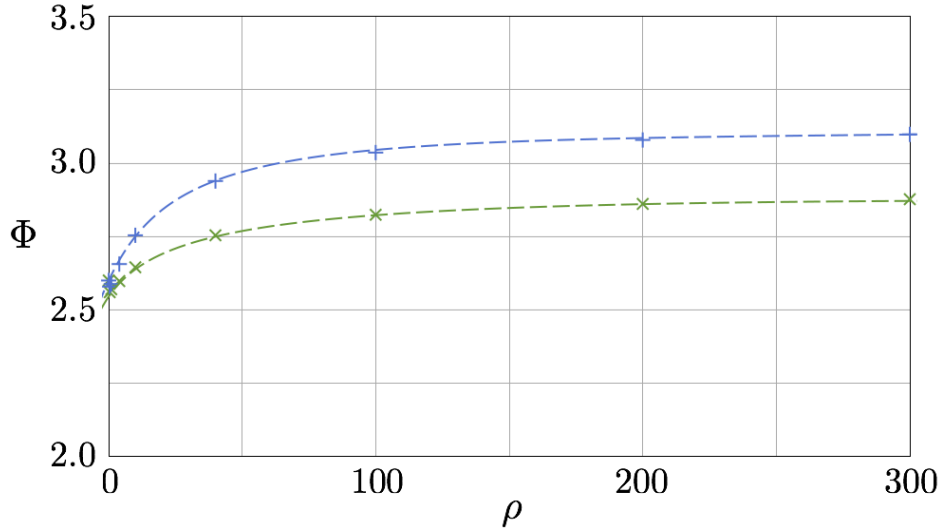


Figure 4.4.: Potential approaching an asymptote for $\beta = 2$ (top line) and 4 (bottom line) for large ρ . $\rho = r_d/\lambda_D$ and $\Phi = -e\phi/kT_e$.

The $\beta > 2$ thin sheath case is more interesting as the OML theory provides a good approximation of the potential to increasing ρ as β is increased, this is shown in Figs.4.2 and 4.3. For $\beta \gtrsim 4$ the potential returned from simulation does not deviate from the OML potential by more than 10%, even at $\rho = 100$.

4.1.4 Numerical Fits

SCEPTIC is now used to find the floating potential over a wide range of the parameters β , A and ρ . In the case of ion mass, hydrogen, helium, nitrogen, neon and argon plasmas are explicitly calculated. Simple numerical expressions for the potential, which include the dependence on β , A and ρ , are obtained empirically from fits to the simulation data. These expressions embody our results in a particularly succinct form, and also provide a quick and simple way of calculating the floating potential of an isolated, spherical dust grain in any collisionless, stationary plasma.

For both very small dust grains (the OML limit) and very large dust grains (the thin sheath limit) the potential is independent of radius. In these cases we find that the data can be well expressed by an equation of the form

$$\Phi = \eta \ln A + \mu \ln \beta + C \quad (4.2)$$

where η and C are constants, and μ in general has a logarithmic dependence on A . As mentioned above, for a given A , the function $\Phi(\beta)$ has a maximum at $\beta \approx 2$ for both OML and the thin sheath limit. We therefore require two sets of the parameters η , μ and C corresponding to $\beta \leq 2$ (Φ increases with β) and $\beta > 2$ (Φ decreases with β).

4.1.4.1 The OML Limit

In this limit the potential is, of course, given by OML. However, a numerical expression is given here for convenience, and to be consistent with the rest of our results. The parameters used in eqn.(4.2) have the values shown in Table 4.1.

	η	μ	C
$\beta \leq 2$	0.405	$0.253 + 0.021 \ln A$	2.454
$\beta > 2$	0.401	$-0.122 + 0.029 \ln A$	2.698

Table 4.1.: Values for the OML limit. Expression (4.2)

A second expression is required to specify the grain size above which OML fails, ρ_{OML} . For any β , $\rho_{\text{OML}} = 1.25\beta^{0.4}$ is found to be an appropriate limit.

4.1.4.2 Thin Sheath Limit

For the thin sheath limit, the values of the parameters used in eqn.(4.2) are given in Table 4.2.

	η	μ	C
$\beta \leq 2$	0.456	0	3.179
$\beta > 2$	0.557	$-0.386 - 0.024 \ln A$	3.399

Table 4.2.: Values for the thin sheath limit. Expression (4.2)

4.1.4.3 Transition Region

In addition to the OML and thin sheath limits there is the transition region. An acceptable approach to calculating the floating potential in this region is via a straight line fit, on a log plot, between the OML limit and the thin sheath limit. All the information required at these two points is given in the above expressions and may be written

$$\phi(\rho) = \frac{\phi_{\text{TS}} - \phi_{\text{oml}}}{\ln \rho_{\text{TS}} - \ln \rho_{\text{oml}}} \ln \left(\frac{\rho}{\rho_{\text{TS}}} \right) + \phi_{\text{TS}}, \quad (4.3)$$

the subscript TS indicated thin sheath quantities. Equation (4.3) is the equation of a straight line fit (on a log plot) between the OML value and OML limit and the thin sheath value and thin sheath limit.

Equation (4.2), with the appropriate parameters, and eqn.(4.3) are compared with SCEPTIC data for hydrogen in Fig. 4.5. Results for helium, nitrogen, neon and argon are shown in Figs.4.6, 4.7, 4.8, and 4.9 respectively, the agreement is seen to be very good.

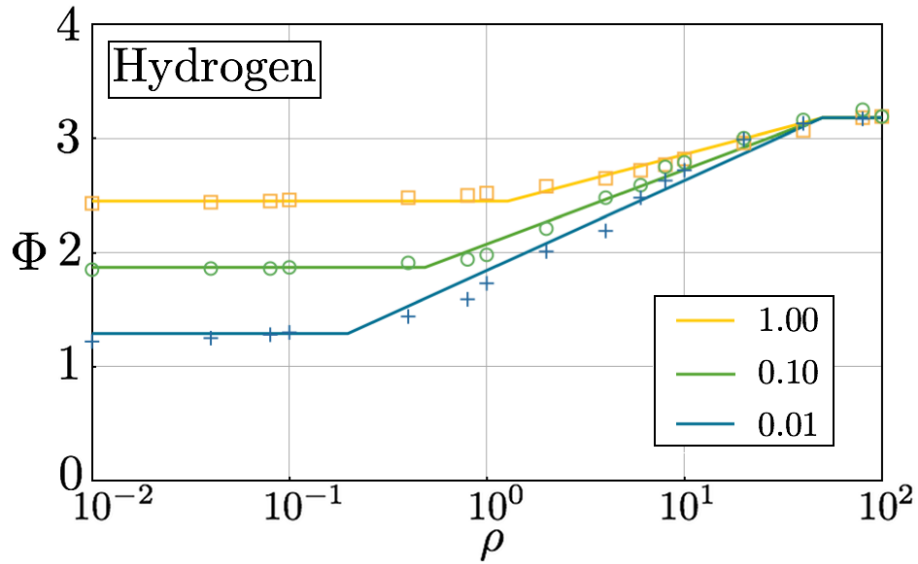


Figure 4.5.: OML and expressions (4.2) and (4.3) in the relevant regions compared with SCEPTIC data. $\beta = 1.00$ topmost line (\square), $\beta = 0.10$ middle line (\circ) and $\beta = 0.01$ bottommost line (+). $\Phi = -e\phi/kT_e$ and $\rho = r_d/\lambda_D$.

4.1.5 Recap on Numerical Fits

So far we have investigated the floating potential of spherical dust grains immersed in a stationary plasma as a function of dust grain size, ion mass and ion to electron temperature ratio. Simulation data agrees extremely well with OM for the limited number of cases for which data is available. Due to the impracticality of generating results with the analytic OM theory, simulation results have been analysed and several expressions for the floating potential as a function of ρ , β and A presented. Due to a maximum in the floating potential at $\beta \approx 2$, different expressions are required for the regions $0 < \beta \leq 2$ and $2 < \beta \leq 10$. In addition, as ρ is varied the results show three distinct regions. For small ρ the simulation results agree closely with OML. At some ρ , typically between 0.1 and 10, the potential departs from OML

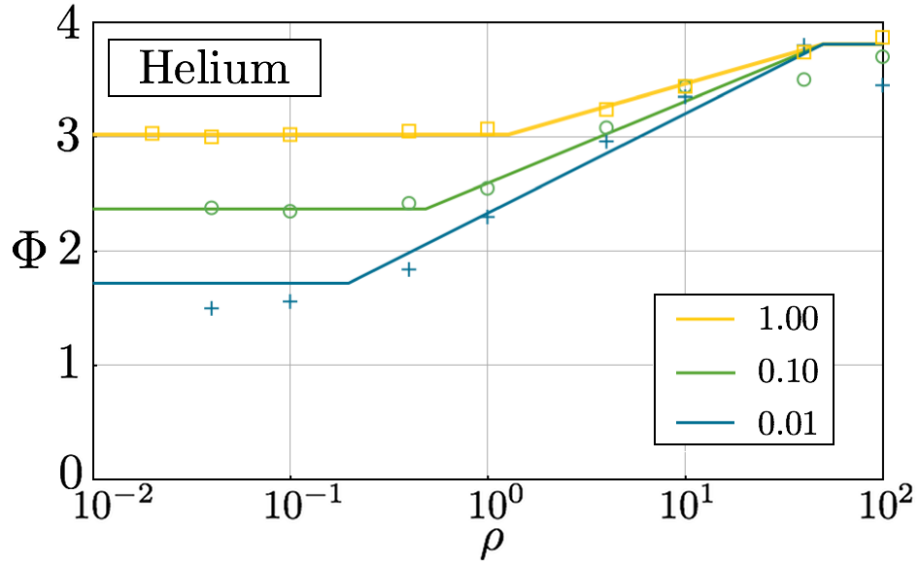


Figure 4.6.: OML and expressions (4.2) and (4.3) in the relevant regions compared with SCEPTIC data. $\beta = 1.00$ topmost line (\square), $\beta = 0.10$ middle line (\circ) and $\beta = 0.01$ bottommost line ($+$). $\Phi = -e\phi/kT_e$ and $\rho = r_d/\lambda_D$.

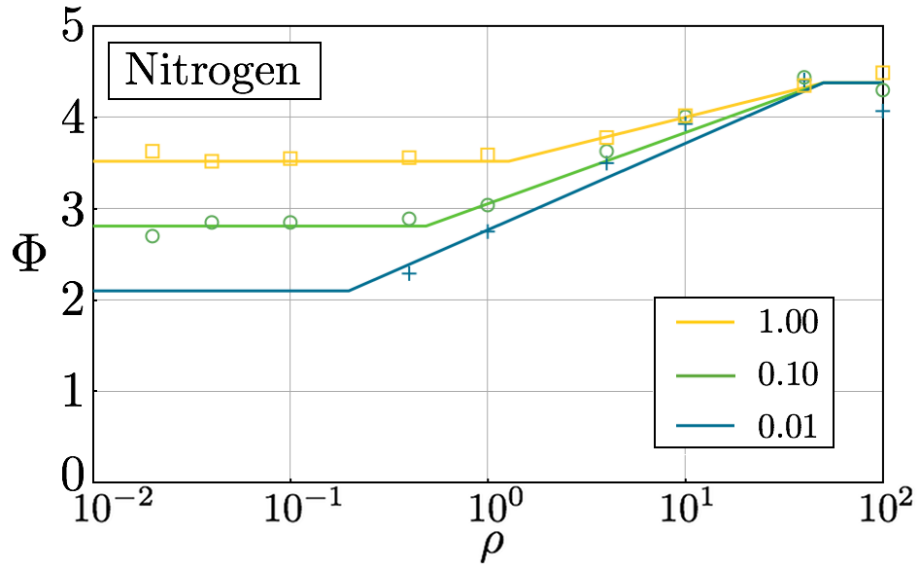


Figure 4.7.: OML and expressions (4.2) and (4.3) in the relevant regions compared with SCEPTIC data. $\beta = 1.00$ topmost line (\square), $\beta = 0.10$ middle line (\circ) and $\beta = 0.01$ bottommost line ($+$). $\Phi = -e\phi/kT_e$ and $\rho = r_d/\lambda_D$.

and increases in magnitude (becomes more negative). The potential continues to increase in this transition region until $\rho \approx 50$ and then approaches an asymptote.

The expressions presented agree with simulation to within 5% over most of the parameter range investigated, and allow the floating potential of a spherical object to be quickly determined for a large range of plasma parameters. In addition, the

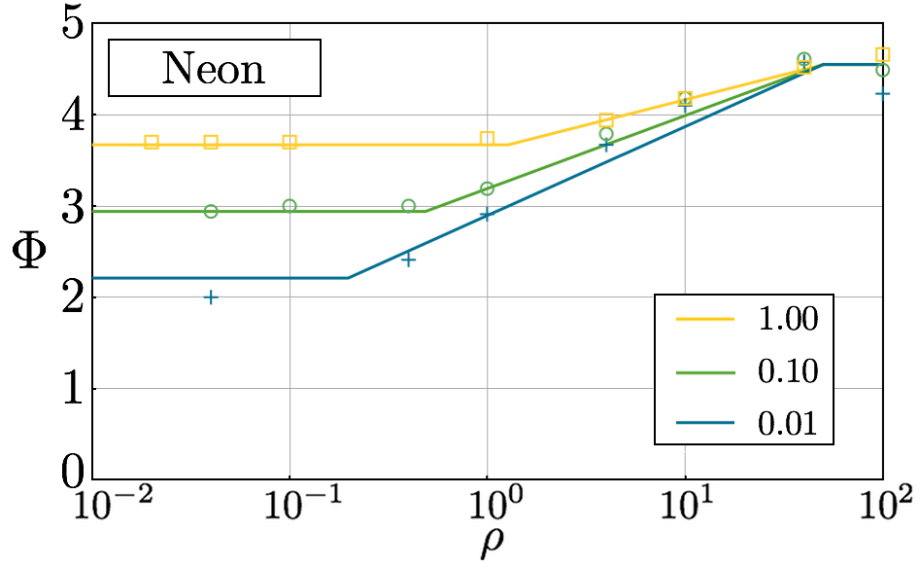


Figure 4.8.: OML and expressions (4.2) and (4.3) in the relevant regions compared with SCEPTIC data. $\beta = 1.00$ topmost line (\square), $\beta = 0.10$ middle line (\circ) and $\beta = 0.01$ bottommost line ($+$). $\Phi = -e\phi/kT_e$ and $\rho = r_d/\lambda_D$.

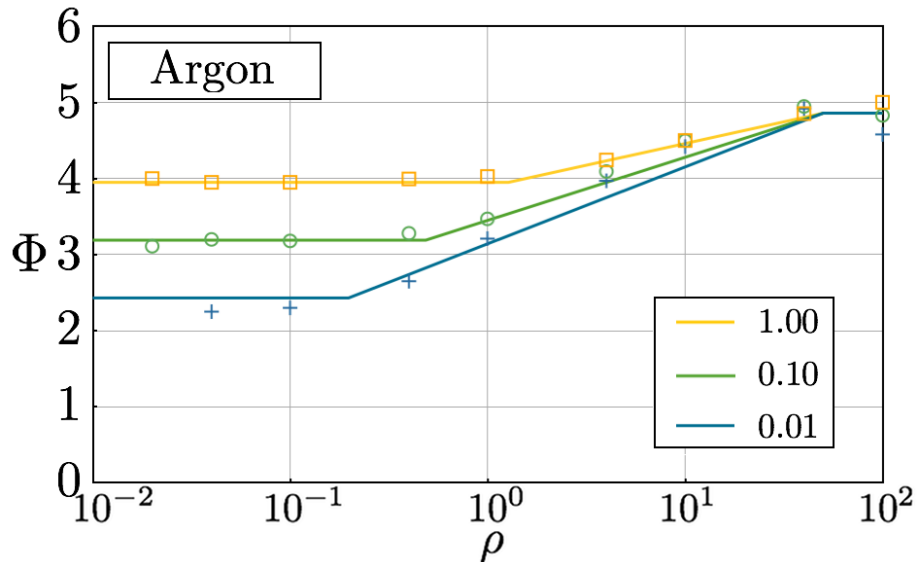


Figure 4.9.: OML and expressions (4.2) and (4.3) in the relevant regions compared with SCEPTIC data. $\beta = 1.00$ topmost line (\square), $\beta = 0.10$ middle line (\circ) and $\beta = 0.01$ bottommost line ($+$). $\Phi = -e\phi/kT_e$ and $\rho = r_d/\lambda_D$.

expressions include a dependence on dust size which is lacking from the OML theory. The expressions have also been tested against simulations for a Mercury plasma and found to be within 10% of simulation results over the whole range of parameters mentioned above, see Fig. 4.10.

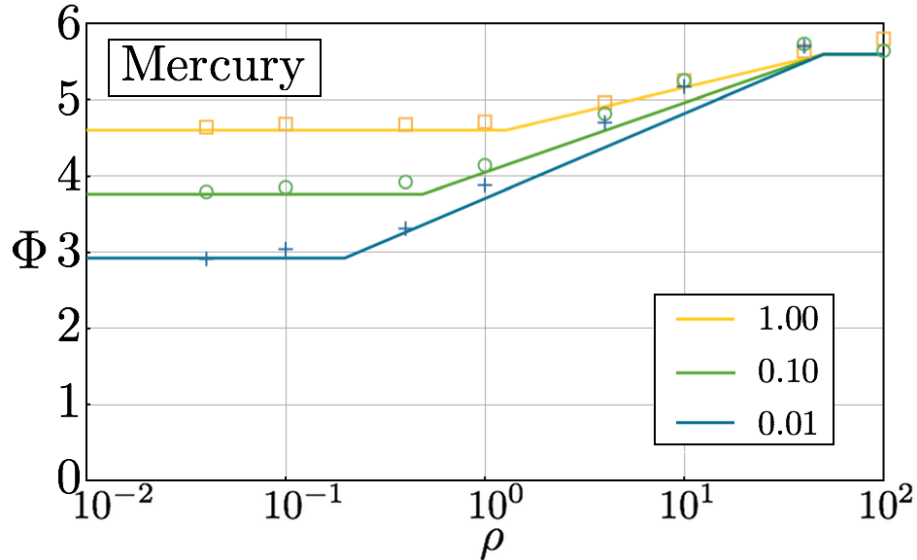


Figure 4.10.: OML and expressions (4.2) and (4.3) in the relevant regions compared with SCEPTIC data. $\beta = 1.00$ topmost line (\square), $\beta = 0.10$ middle line (\circ) and $\beta = 0.01$ bottommost line (+). $\Phi = -e\phi/kT_e$ and $\rho = r_d/\lambda_D$.

4.2 MODIFYING OML

The numerical fits tell us a lot about the behaviour of the potential, but not much about the underlying physics. In addition, if we wish to introduce flow into the problem we will be faced with an even larger parameter space. Perhaps the most important information to come out of the numerical fits is the departure from OML and the transition to the thin sheath region. If we had an analytic model of the plasma/potential behaviour in the thin sheath limit we could both understand the physics better and still describe the potential as a function of ρ using eqn.(4.3).

In this section we outline a possible choice of model for use in the thin sheath limit. We conclude that the failing of this model is its treatment of the presheath and go on to develop our own model based on OML.

4.2.1 Large Dust Grains

For dust grains large with respect to the Debye length the sheath becomes approximately planar but the presheath does not; an appropriate theoretical comparison for this limit is not easily found. In order for ions approaching the sheath to satisfy the Bohm criterion the ion current density in the presheath must increase towards the sheath and/or the ions must feel a retarding force. In plane geometry this is achieved by including ionisation or collisions in the presheath. The spherical geom-

etry used in SCEPTIC gives rise to ion focusing towards the grain and a consequent increase in the ion current density.

To obtain a rigorous comparison the problem must be treated kinetically. The previously described OM would be an ideal comparison in the large ρ limit if more data were available. As no obvious analogy exists for the presheath between SCEPTIC and theory, a comparison is made with simple approximations. Taking an isothermal, planar presheath, and taking the ion velocity to be the isothermal sound speed at the sheath edge the potential drop from bulk plasma to sheath edge is found to be $\ln(2)kT_e/e$ [84].

For non-zero T_i there is no universally valid expression for the Bohm speed, even in the planar case. Nevertheless, to provide an estimate of the potential drop across the sheath for $T_i \neq 0$ we assume the Bohm speed is equal to the sound speed at the sheath edge

$$v_{se} = \sqrt{\frac{(kT_e + \gamma kT_i)}{m_i}}, \quad (4.4)$$

the subscript se indicates quantities at the sheath edge and γ is the ratio of specific heat capacities. Here we find *a posteriori* that $\gamma = 5/3$ fits simulation data most closely. In §6 we find that for strongly flowing plasmas $\gamma = 3$ is more appropriate.

The ion flux density (Γ) at the sheath edge is

$$\Gamma_{se}^i = n_{se} v_{se}, \quad (4.5)$$

where n_{se} and v_{se} are the density and velocity at the sheath edge. The ion current at the sheath edge is assumed to be equal to the ion current at the grain surface, $\Gamma_{se}^i = \Gamma_{grain}^i$.

As the electrons are in a repulsive potential, their one-way flux is given by

$$\Gamma_{grain}^e = \frac{1}{4} n_{se} \left(\frac{8kT_e}{\pi m_e} \right)^{1/2} \exp \left(\frac{e\phi_{wall}}{kT_e} \right) \quad (4.6)$$

where ϕ_{wall} is the potential relative to the sheath edge i.e. the potential drop across the sheath. Equating the electron and ion flux to the grain surface

$$n_{se}^i \left(\frac{kT_e + \gamma kT_i}{m_i} \right)^{1/2} = \frac{1}{4} n_{se}^e \left(\frac{8kT_e}{\pi m_e} \right)^{1/2} \exp \left(\frac{e\phi_{wall}}{kT_e} \right). \quad (4.7)$$

At the sheath edge the ion density equals the electron density as the plasma is quasineutral (i.e. it's a plasma). Normalising and rearranging we have

$$\Phi_{\text{wall}} = \frac{1}{2} \ln \left[2\pi \frac{m_e}{m_i} (1 + \gamma\beta) \right]. \quad (4.8)$$

Assuming that the ion flux at the sheath edge is the same as at the wall, and equating it with a one-way Maxwellian flux for the electrons, the floating potential is found to be

$$\Phi = \frac{1}{2} \ln \left[2\pi \frac{m_e}{m_i} (1 + \gamma\beta) \right] + \ln(2), \quad (4.9)$$

where the potential drop in the isothermal, planar presheath has been included.

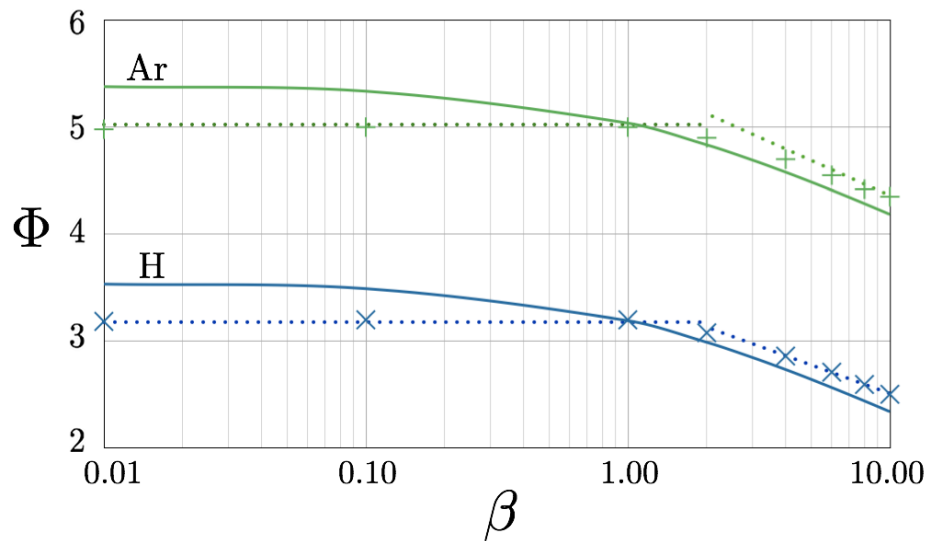


Figure 4.11.: Simulation results for hydrogen and argon, $\rho = 100$. The solid lines are from the analytic treatment, eqn.(4.9). The dotted lines are eqn.(4.2) with the thin sheath parameters, Table 4.2. $\beta = T_i/T_e$ and $\Phi = -e\phi/kT_e$.

Equation (4.9) is compared with SCEPTIC and the numerical fits in Fig. 4.11, for large grains and $\beta < 1$ the SCEPTIC results for the floating potential are relatively independent of temperature. The simple analytic model agrees well, this is perhaps not surprising as the assumptions going into it are all sensible. As seen in Fig. 4.11, the simple model is least accurate for $\beta < 1$. This is unfortunate as the majority of plasmas lie in this range. The main point of contention with the simplistic model is the presheath potential drop as a single value, independent of ion temperature is used.

A modified version of OML is now presented for large dust grains. This modified version includes an ion temperature dependence in the presheath. Initially we

investigate the stationary case and then in §5 the flowing case. This modified OML is compared with simulation and found to be in good agreement.

4.2.2 Introduction to Modified OML

Hutchinson [87] has noted, whilst using SCEPTIC to investigate the ion drag force, that for large dust grains there is a separation of length scales. There is the presheath extending for many dust radii into the plasma, and the thin sheath of just a few Debye lengths, and the OML approach can only be used in the presheath where the potential varies slowly. For small grains the transition between the two is “fuzzy” but for large grains it can be well defined. In the thin sheath limit we specify the sheath edge as the point where the ion and electron densities differ from each other by 3%. Figure 4.12 shows the behaviour of the ion and electron densities and the potential for a large grain. The subplot in Fig. 4.12 shows a closer view of the densities and their separation is seen to be well defined. The sheath edge is generally found to be around $1.08r_d$ for $\rho = 100$, i.e. $\sim 8\lambda_D$.

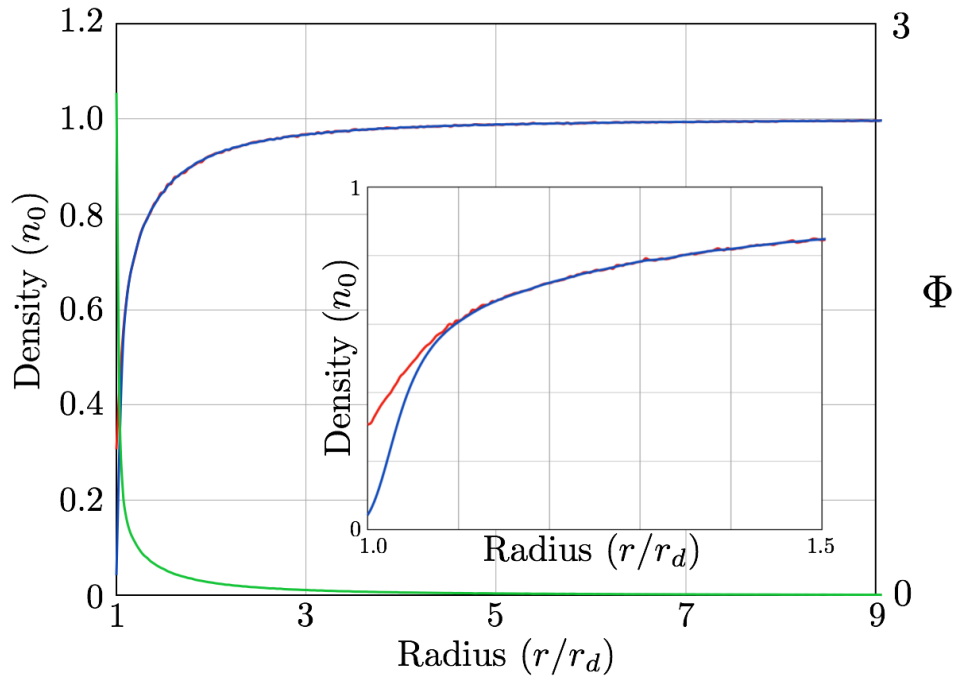


Figure 4.12.: The ion (red) and electron (blue) densities and the potential (green) as a function of radius for a large dust grain. $\Phi = -e\phi/kT_e$.

The main assumption we make is that all ions entering the sheath are collected by the dust grain. The ion current at the sheath edge is therefore equal to the ion current at the grain surface, the validity of this assumption is tested in section 4.2.4.

In the sheath region OML cannot be applied due to the large gradient of the radial potential. In the presheath however, OML may still be reasonably applied as the potential is varying slowly, although there is no guarantee it is less steep than $1/r^2$ everywhere. Fig. 4.13 shows the gradient of the potential for a large dust grain ($\rho = 80$) compared with the modulus of the gradient of $1/r^2$ ($| -2/r^3 |$). Near the grain the gradient of the potential is much larger than that of $1/r^2$ invalidating OML. The gradient of the potential falls below that of $1/r^2$ at approximately $1.25 r_d$ indicating the OML is applicable further out. Looking at the point of quasineutrality break down the sheath edge is found to be around $1.08 r_d$ so absorption radii in the region $1.08 < r/r_d < 1.25$ will be unaccounted for and result in an error.

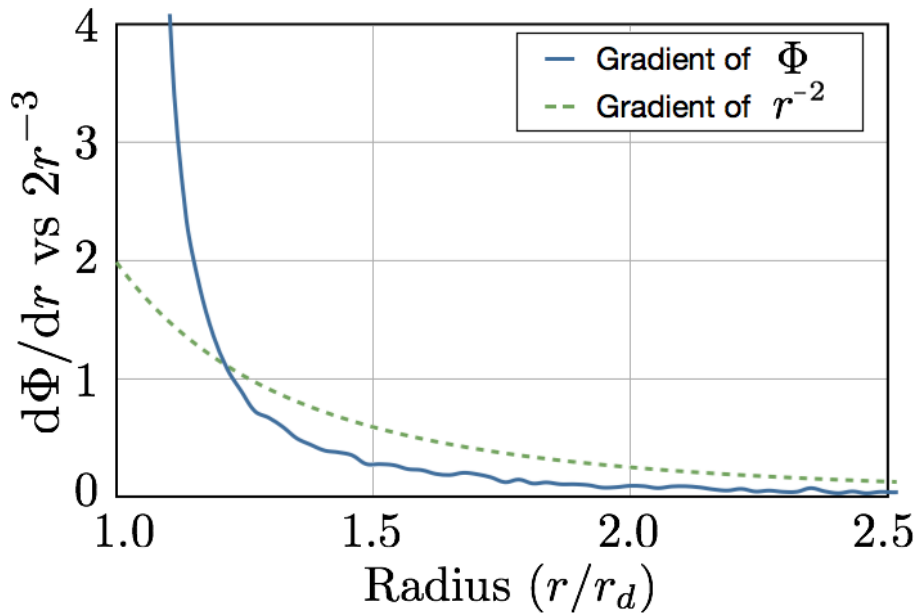


Figure 4.13.: Gradient of the potential (solid) and the gradient of $1/r^2$ (modulus).
 $\beta = 0.2, \rho = 80$.

Assuming OML to be valid up to the sheath edge includes the assumption that all absorption radii are at or within the sheath edge. This is never likely to be 100% accurate, Fig. 4.13 shows the position where the gradient of the potential becomes less than the gradient of $1/r^2$ to be approximately $1.25 r_d$ for $\beta = 0.2$, that is $20\lambda_D$ from the grain surface. The sheath is typically only a few λ_D so there will be some absorption radii unaccounted for. The absorption radii are expected to have a greater impact for lower β however, we will find that only an error of $< 10\%$ is introduced.

The upper limit of ρ for which OML is still a good approximation, introduced in 4.1.4.2, is well described by the empirically determined formula $\rho_{\text{oml}} = 1.25\beta^{0.4}$.

For dust grains with $\rho > 50$ the sheath around the grain becomes thin and a limiting value of the floating potential is approached asymptotically with increasing ρ , this can be seen in both simulation data [86] and more advanced charging models such as ABR [63] and OM [67].

We start with the standard OML currents

$$I_e = -4\pi r_d^2 n_e e \left(\frac{kT_e}{2\pi m_e} \right)^{1/2} \exp \left(\frac{e\phi}{kT_e} \right) \quad (4.10)$$

$$I_i = 4\pi r_d^2 n_i e \left(\frac{kT_i}{2\pi m_i} \right)^{1/2} \left(1 - \frac{e\phi}{kT_i} \right). \quad (4.11)$$

The electrons, being repelled, do not encounter absorption radii (from eqn.(2.25), the angular momentum would be imaginary) and the OML electron current is assumed to be correct for large grains. Instead of determining the ion current from the potential of the dust grain, we choose to determine it from the potential at the sheath edge, recalling our assumption that the ion current at the sheath edge is equal to the ion current at the grain surface. Taking the potential drop across the sheath to be $\Delta\phi$ we write a modified OML ion current

$$I_i = 4\pi r_d^2 n_i e \left(\frac{kT_i}{2\pi m_i} \right)^{1/2} \left(1 - \frac{e(\phi - \Delta\phi)}{kT_i} \right). \quad (4.12)$$

The ion current is therefore reduced and as a result, the floating potential will be more negative (the normalised floating potential Φ will increase in magnitude). Equating the OML electron current with this new ion current we have

$$\left(\frac{kT_e}{2\pi m_e} \right)^{1/2} \exp \left(\frac{e\phi}{kT_e} \right) = \left(\frac{kT_i}{2\pi m_i} \right)^{1/2} \left(1 - \frac{e(\phi - \Delta\phi)}{kT_i} \right). \quad (4.13)$$

Normalising and rearranging

$$\exp(-\Phi) = \left(\beta \frac{m_e}{m_i} \right)^{1/2} \left(1 + \frac{\Phi}{\beta} - \frac{\Delta\Phi}{\beta} \right). \quad (4.14)$$

The remaining problem is what to take as the potential drop across the sheath. In this thin sheath limit we assume the potential drop across the sheath is the same as the sheath drop for a planar wall. We therefore use the simple model for the sheath outlined in section 4.2.1 with $\Delta\Phi$ given by eqn.(4.8). In effect, the presheath geometry remains spherical as its width is large. The presheath is described adequately by the OML theory with any error introduced by unaccounted for absorption radii

present in the presheath. We are basically treating the grain surface as being held at a lower potential as far as the ions are concerned. In addition, the geometrical concentration of the ions towards the grain is required in the presheath in order to satisfy the Bohm condition as there is no other mechanism employed for increasing ion current density towards the sheath.

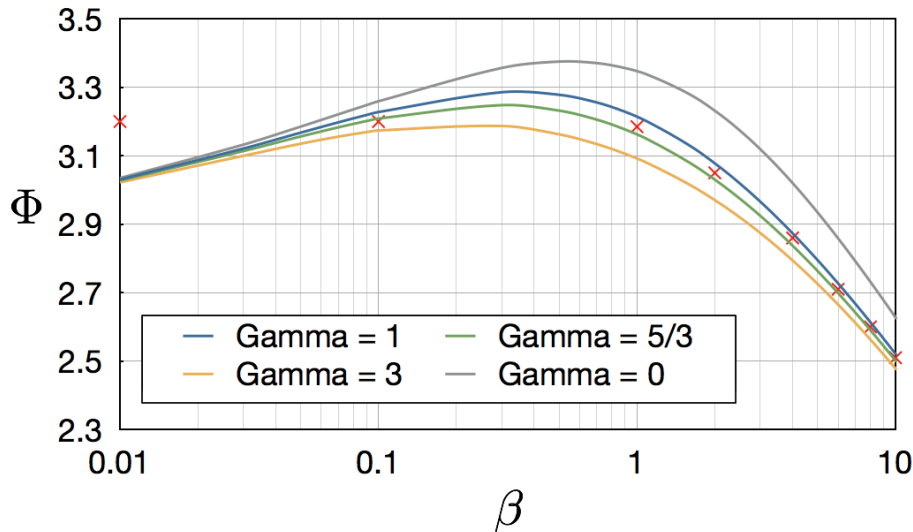


Figure 4.14.: The floating potential (\times) as a function of β for large grains ($\rho = 100$) in a stationary, hydrogenic plasma. The solution to eqn.(4.15) is shown for a number of γ s. $\Phi = -e\phi/kT_e$.

Replacing $\Delta\Phi$ in eqn.(4.14) with Φ_{wall} from eqn.(4.8) we have a modified OML equation valid in the thin sheath limit

$$\exp(-\Phi) = \left(\beta \frac{m_e}{m_i} \right)^{1/2} \left(1 + \frac{\Phi}{\beta} + \frac{1}{2\beta} \ln \left(2\pi \frac{m_e}{m_i} (1 + \gamma\beta) \right) \right). \quad (4.15)$$

As with OML, this must be solved numerically. Equation (4.15) is compared with simulation data in Fig. 4.14 for a number of γ s, $\gamma = 5/3$ is chosen as the most appropriate.

Equation (4.15) is compared with normal OML in Fig. 4.15 for varying β . Equation (4.15) is seen to be a good approximation over the whole range of β , and clearly provides a more appropriate estimate than OML for determining the floating potential of large dust grains, regardless of the unaccounted for absorption radii. Although absorption radii have an effect for low β the error introduced is minor (< 10%) compared with the error in using OML for large grains. Also shown in Fig. 4.15 is the sheath drop and the potential assuming the ions ignore the electric field. The sheath drop provides a graphical representation of how modified OML handles the presheath. The difference between the red and green curves is the modified OML

potential drop across the presheath, and is clearly a function of ion temperature as required. We see modified OML indicates a larger presheath drop with increasing β and underestimates the presheath drop for low β .

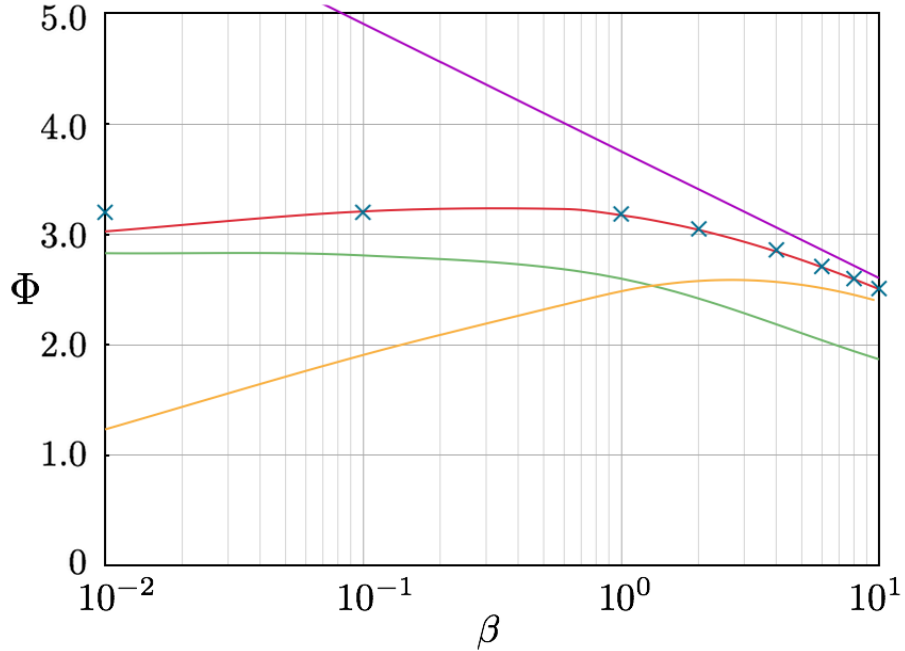


Figure 4.15.: Floating potential as a function of β for large grains ($\rho = 100$) in a stationary, hydrogenic plasma. SCEPTIC data (\times), OML potential (yellow), solution to eqn.(4.15) (red), the sheath drop given by eqn.(4.8) (green) and the grain potential assuming the ions ignore the electric field (purple). $\beta = T_i/T_e$ and $\Phi = -e\phi/kT_e$.

4.2.3 Intermediate Values of ρ

The modified version of OML we have presented provides a means of simply estimating the floating potential of dust grains large with respect to the electron Debye length more closely than OML. When discussing the numerical fits in section 4.1.4.3, eqn.(4.3) was used to find the potential in the transition region. To use this approach with our thin sheath model requires solving a transcendental equation in both the thin sheath limit and the OML limit. Instead, we let the $\Delta\Phi$ term in eqn.(4.14) vary with ρ . In other words, $\Delta\Phi$ is zero in the OML case and given by eqn.(4.8) in the thin sheath case. $\Delta\Phi(\rho)$ is then a straight line (on a log) plot between the two. As before, $\rho_{upper} = 50$ is taken as the thin sheath limit and the OML limit, empirically found to be well approximated by $\rho_{lower} = 1.25\beta^{0.4}$. In the transition region then we have

$$\Delta\Phi(\rho) = \Delta\Phi \left(\frac{\ln(\rho/\rho_{upper})}{\ln(\rho_{upper}/\rho_{lower})} + 1 \right). \quad (4.16)$$

In the transition region we now have to solve the following equation once, not twice.

$$\exp(-\Phi) = \left(\beta \frac{m_e}{m_i}\right)^{1/2} \left(1 + \frac{\Phi}{\beta} - \frac{\Delta\Phi(\rho)}{\beta}\right). \quad (4.17)$$

An example using this method is shown in Fig. 4.16. The thin sheath value for $\beta = 0.01$ is too low, as seen in Fig. 4.15 due to absorption radii in the presheath.

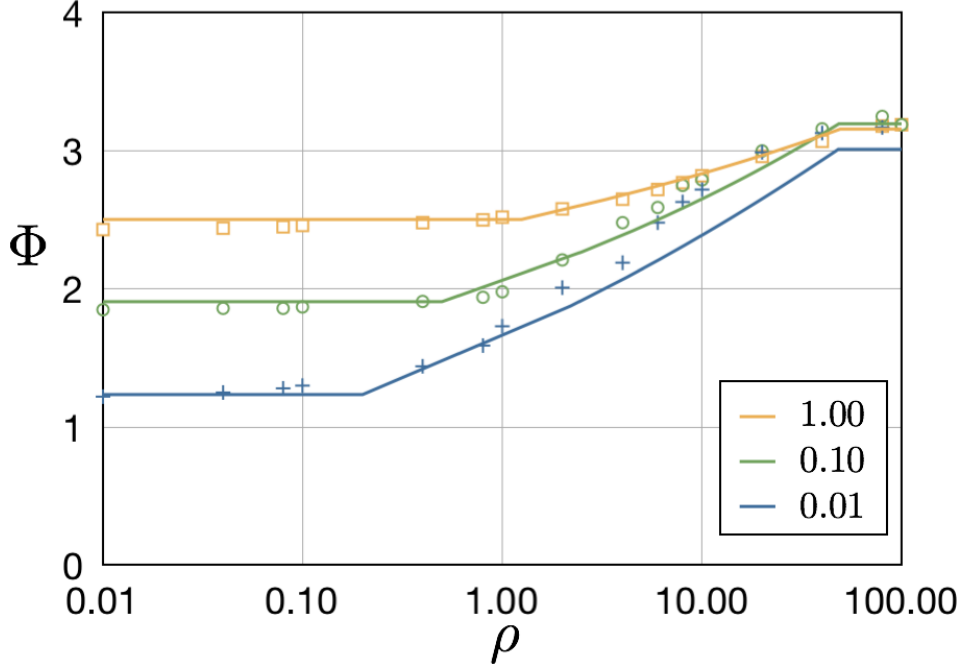


Figure 4.16.: The floating potential according to Modified OML vs SCEPTIC data, the Transition region is calculated using eqn.(4.17). $\rho = r_d/\lambda_D$ and $\Phi = -e\phi/kT_e$.

4.2.4 The Validity of Modified OML

Despite the existence of unaccounted for absorption radii, modified OML has furnished us with some encouraging results. We now investigate the errors introduced by ignoring the absorption radii. This will serve to further clarify the problem, and convince us that using OML in the presheath only introduces a small error.

One result from our simulations is the steady state potential as a function of position. We use this to investigate absorption radii and the plausibility of using

OML up to the sheath edge. As we saw in section 2.5, the energy of an ion may be written as

$$E = \frac{1}{2}m_i v_r^2 + \underbrace{\frac{1}{2} \frac{J^2}{m_i r^2} + q\phi(r)}_U$$

where U is an effective potential. Writing U as

$$U = \frac{1}{2}m_i \frac{J^2}{m_i^2 r^2} + e\phi$$

we normalise to find

$$\hat{U} = \frac{\hat{J}^2}{2\hat{r}^2} - \Phi$$

where

$$\hat{J} = \frac{J}{m_i v_{is} r_d} = \frac{m_i v_\theta r}{m_i r_d} \sqrt{\frac{m_i}{kT_e}}, \quad \Phi = -\frac{e\phi}{kT_e},$$

v_{is} is the ion sound speed. We drop the hats from now on.

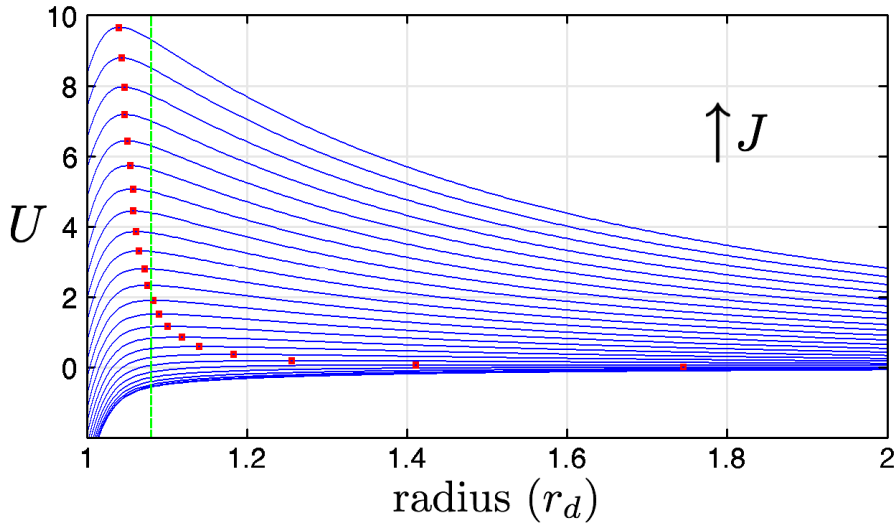


Figure 4.17.: Effective Potential contours shown in blue for increasing J , the red squares indicate maxima and the green dashed line represents the sheath edge at $1.08r_d$. $\rho = 100$, $\beta = 1.0$ and U is normalised by kT_e .

We have used OML to describe the ion current up to the sheath edge, all ions entering the sheath assumed to be collected. Ions encountering absorption radii outside the sheath will invalidate OML so we wish to know if absorption radii exist in the presheath and, if they do, what error they introduce. Figure 4.17 shows

the effective potential U for the case of $\rho = 100$ and $\beta = 1.0$. Clearly absorption radii are present, they occur at the maxima in the effective potential curves and are marked by the red squares. The majority of the absorption radii are within the sheath however, a number of absorption radii are seen in the presheath.

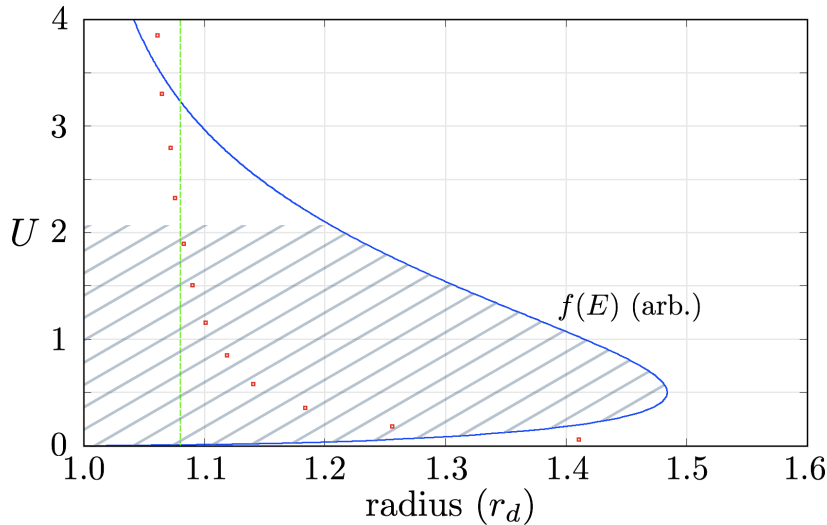


Figure 4.18.: Effective Potential maxima (red \square) and energy distribution of the ions for $\beta = 1.0$ (blue line), the green dashed line represents the sheath edge. U is normalised by kT_e

To determine what fraction of the ions these absorption radii potentially effect we look at the ion energy distribution in relation to the absorption radii. In the case of Fig. 4.17, the value of U corresponding to the effective potential curve with its maximum at the sheath edge is approximately $2.1kT_e$, any ion with E greater than this *cannot* encounter an absorption radii in the presheath. Figure 4.18 shows the maxima in the effective potential and the distribution of ion energies. Clearly a large proportion of the ion distribution can potentially encounter absorption radii, approximately 76% (the crosshatched area). Initially then, trying to use OML up to the sheath edge does not look plausible for $\beta = 1.0$. If we do the same thing for $\beta = 10.0$ however, this simple estimate shows only $\sim 3\%$ of the ion distribution encounter effective potential maxima in the presheath and OML hence be used confidently in the presheath.

Note: Just because an ion has E such that it may encounter an absorption radius does not mean it will, it depends on both E AND J .

We investigate the case of $\beta = 1.0$ further by looking at the critical value of angular momentum, the angular momentum above which no more ions are absorbed,

as a function of energy, $J_{\text{crit}}(E)$. The integral for the ion current may be rewritten as an integral over J and E [67], after normalisation it reads

$$I_i = \beta^{-3/2} \int_0^E \int_0^{J_{\text{crit}}} J e^{-E/\beta} dJ dE, \quad (4.18)$$

the current is normalised by $4\pi r_d^2 e n_0 \sqrt{\frac{kT_e}{2\pi m}}$. The ion current given by this integral is correct, the subsequent error in the OML approach is solely introduced by the assumption of the form of $J_{\text{crit}}(E)$. If we know the correct form of $J_{\text{crit}}(E)$ then eqn.(4.18) will give the correct ion current. Equation (4.18) only becomes the OML ion current when $J_{\text{crit}}(E)$ is determined from the cross-section assuming grazing incidence ion orbits.

For a given ion energy in OML there is a critical impact parameter corresponding to the grazing incidence trajectory of an ion on the dust grain, this determines $J_{\text{crit}}(E)$. In reality, depending on the form of the potential, an ion with the same energy will have a critical impact parameter, and subsequently a critical angular momentum, at which it grazes some imaginary surface which may be larger than the dust grain.

When performing the OML integral for the ion current over the ion velocities, eqn.(2.59), an impact parameter for a grazing incidence ion is specified as a function of the grain potential, ϕ_d , and the velocity at infinity, v_∞ . When integrating over E and J this is replaced with a critical angular momentum, J_{crit} . For a given energy, J_{crit} represents the angular momentum of the grazing incidence ion, it is simply the impact parameter, eqn.(2.58), multiplied by $m_i v_\infty$. The critical angular momentum for the ions in OML is given by [67]

$$J_{\text{crit}}^{\text{OML}} = m_i v_\infty r_d \sqrt{1 - \frac{2e\phi_d}{Mv_\infty^2}}.$$

This may be normalised to

$$J_{\text{crit}}^{\text{OML}} = \sqrt{2E} \sqrt{1 + \frac{\Phi_d}{E}}. \quad (4.19)$$

Recalling that to solve OML for the floating potential we equate the ion and electron currents and find the root. Instead, if we take the floating potential from simulation data for a large grain and feed this into the OML current components we will find the respective currents. From simulation data, the floating potential of a

grain is 3.18 for $\beta = 1.0$ and $\rho = 100.0$, using this in the normalised OML currents we have

$$I_i^{OML} = \beta^{-3/2} \int_0^E \int_0^{J_{crit}^{OML}} J e^{-E/\beta} dJ dE = \sqrt{\beta} \left(1 + \frac{\Phi}{\beta} \right) = 4.18$$

$$I_e^{OML} = \sqrt{\frac{m_i}{m_e}} \exp(-\Phi) = 1.78.$$

The electron current is correct, but the ion current is too large due to the unaccounted absorption radii, as expected.

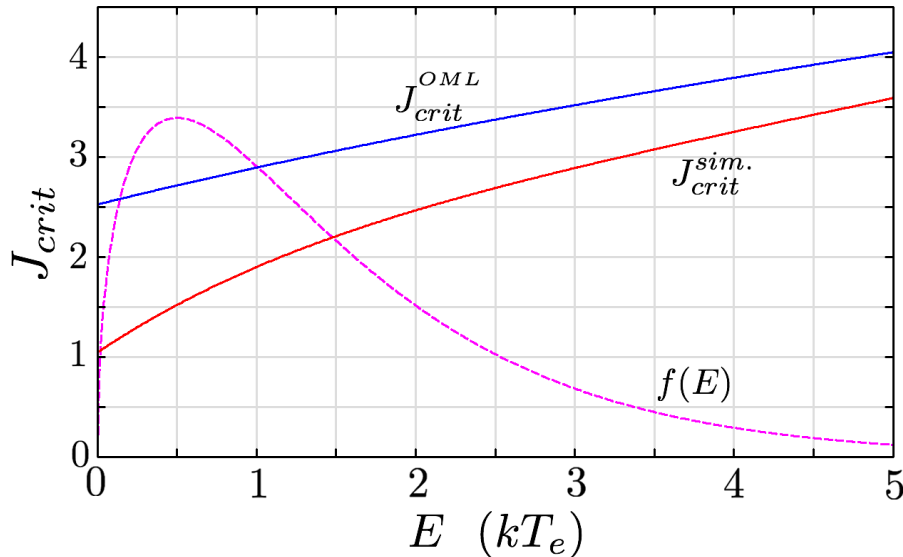


Figure 4.19.: J_{crit} from OML, eqn.(4.19) (blue) and J_{crit} from SCEPTIC data (red) for $\beta = 1.0$, the ion energy distribution is also shown. J is normalised by $m_i r_d \sqrt{kT_e/m_i}$.

In general $J_{crit}(E)$ is unknown however, for specific cases we can determine it from simulation data and compare it with the critical angular momentum in OML. In Fig. 4.18 the maxima in the effective potential marked by the red squares show the minimum energy an ion of a given angular momentum must have to overcome the barrier in the effective potential. Conversely, we can take a given energy and ask what the critical angular momentum is for that energy, any ion with angular momentum larger than this will encounter a potential barrier. Fitting a curve to the red squares in Fig. 4.18 we can therefore find $J_{crit}(E)$, for a specific case, from simulation data, we dub this J_{crit}^{sim} . Figure 4.19 is a comparison between J_{crit}^{sim} and J_{crit}^{OML} for the case of $\beta = 1.0$, $\rho = 100$. Over the range of energies shown OML overestimates $J_{crit}(E)$.

If we now take the integral form of the ion current, eqn.(4.18), and integrate from $J = 0$ to $J_{\text{crit}}^{\text{sim}}$, the red line in Fig. 4.19, we find

$$I_i = \beta^{-3/2} \int_0^E \int_0^{J_{\text{crit}}^{\text{sim}}} J e^{-E/\beta} dJ dE = 1.77 \approx I_e^{\text{OML}}.$$

Using $J_{\text{crit}}^{\text{sim}}$ therefore gives the correct ion current, the error being purely due to the quality of the fit.

We see then that J_{crit} is the crux of the problem. The further from the grain we wish to employ OML, the smaller the error. We can convince ourselves of this using the OML critical angular momentum

$$J_{\text{crit}}^{\text{OML}} = \sqrt{2E} \sqrt{1 + \frac{\Phi_d}{E}}.$$

Applying OML at the sheath edge we are effectively using $\Phi_d \approx 0.8$. Taking $\Phi_d = 0.8$ we plot a new $J_{\text{crit}}^{\text{OML}}$ in Fig. 4.20 and compare it with $J_{\text{crit}}^{\text{sim}}$. By using a smaller Φ_d the OML critical angular momentum has been lowered sufficiently to make it acceptable. The error introduced by ignoring the absorption radii up to the sheath edge is now seen to be minimal (for lower β s the error is larger). The majority of the error now comes from the simple model we assume for the sheath drop.

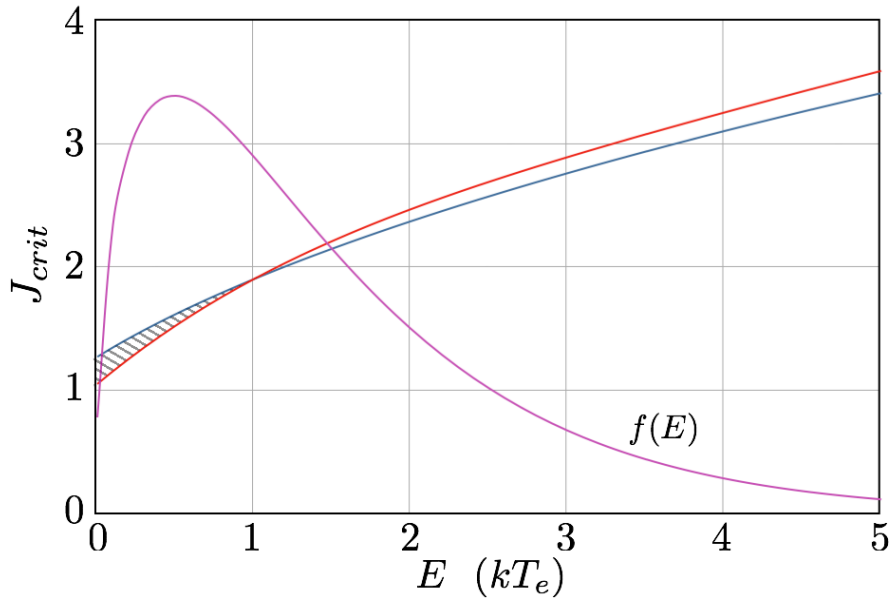


Figure 4.20.: The blue line is $J_{\text{crit}}^{\text{OML}}$ with $\Phi_d = 0.80$ and the red line is $J_{\text{crit}}^{\text{sim}}$, the critical angular momentum found from simulation. The shaded area highlights the difference between the two. J is normalised by $m_i r_d \sqrt{kT_e}/m_i$.

4.3 SUMMARY

Providing we accurately know the potential drop between the dust grain surface and the point at which we wish to apply OML, we can use modified OML at any radius after $J_{\text{crit}}^{\text{OML}}$ has dropped below $J_{\text{crit}}^{\text{sim}}$. We see that the error introduced by the unaccounted for absorption radii is small and the results shown in Fig. 4.15 agree well with simulation. This modified version of OML will really come into its own in the next chapter as we include flow in the problem.

LARGE GRAINS IN A FLOWING PLASMA

Having investigated the behaviour of the floating potential in the stationary case, we look now at the flowing case. For small grains Hutchinson [44] has presented results on the floating potential in flow using SCEPTIC. For the parameters investigated, $\beta = 1.0$ and 0.1 , $\rho \leq 1.0$ and flow velocities up to $5u$ (where u is the flow velocity normalised by $\sqrt{kT_e/m_i}$). Hutchinson finds good agreement between simulation and SOML.

We begin by testing shifted OML (SOML) for small grains even though, as in the previous chapter, it is primarily the large grain/thin sheath limit in which we are interested. SOML, like OML, assumes a spherically symmetric potential. As flow is introduced we would therefore expect SOML to make increasingly inaccurate predictions. What we find however, is that SOML provides a good estimate of the floating potential, even at large flows. As such, we first analyse the SOML ion current in order to understand the importance of assuming a spherically symmetric potential. We then investigate the behaviour of the potential as ρ is increased. As in the stationary case, absorption radii reduce the ion current leading to the magnitude of the potential increasing. We modify the SOML ion current in the same manner as in the stationary case and discuss why this is appropriate in the flow case. Finally we compare simulation results for large grains with our modified version of SOML.

5.1 SOML FOR SMALL GRAINS

The stationary OML ion current is

$$I_i = \sqrt{\beta \frac{m_e}{m_i}} \left(1 + \frac{\Phi}{\beta} \right). \quad (5.1)$$

The integral for the SOML ion current is [68]

$$I_i = 2\pi e \int_0^\infty \int_0^\pi \sigma(v) v^3 f(v, \theta) \sin \theta d\theta dv \quad (5.2)$$

where the cross section $\sigma(v)$, as in OML, is given by

$$\sigma(v) = \pi r_d^2 \left(1 - \frac{2e\phi_d}{m_i v^2}\right), \quad (5.3)$$

and the distribution is that of a shifted Maxwellian

$$f(v, \theta) = n_i \left(\frac{m_i}{2\pi k T_i}\right)^{3/2} \exp\left[-\frac{m_i}{2k T_i}(v^2 + w^2 - 2vw \cos \theta)\right]. \quad (5.4)$$

Performing this integration and equating the ion current with the electron current, eqn.(4.10), we have

$$e^{-\Phi} \left(\beta \frac{m_e}{m_i}\right)^{-1/2} = \underbrace{\frac{\sqrt{2\pi\beta}}{4u} \text{erf}\left(\frac{u}{\sqrt{2\beta}}\right)}_1 + \underbrace{\frac{1}{2} \exp\left(-\frac{u^2}{2\beta}\right)}_2 + \underbrace{\frac{\sqrt{2\pi\beta}}{2u} \text{erf}\left(\frac{u}{\sqrt{2\beta}}\right) \frac{\Phi}{\beta}}_3 + \underbrace{\frac{u}{4} \sqrt{\frac{2\pi}{\beta}} \text{erf}\left(\frac{u}{\sqrt{2\beta}}\right)}_4. \quad (5.5)$$

The right hand side of this equation is the normalised ion current, the flow speed is typically normalised by $\sqrt{2kT_i/m_i}$. However, in the above equation the flow speed u is normalised by $\sqrt{kT_e/m_i}$, this accounts for the factors of $\sqrt{2\beta}$ which may look unfamiliar. We choose this normalisation scheme as it is inline with the rest of this thesis.

5.1.1 Low Flow Limit

As $u \rightarrow 0$, $\text{erf}(\frac{u}{\sqrt{2\beta}}) \rightarrow \frac{2u}{\sqrt{2\pi\beta}}$ and we have

$$e^{-\Phi} \left(\beta \frac{m_e}{m_i}\right)^{-1/2} = \underbrace{\frac{\sqrt{2\pi\beta}}{4u} \frac{2u}{\sqrt{2\pi\beta}}}_1 + \underbrace{\frac{1}{2} \exp\left(-\frac{u^2}{2\beta}\right)}_2 + \underbrace{\frac{\sqrt{2\pi\beta}}{2u} \frac{2u}{\sqrt{2\pi\beta}} \frac{\Phi}{\beta}}_3 + \underbrace{\frac{u}{4} \sqrt{\frac{2\pi}{\beta}} \frac{2u}{\sqrt{2\pi\beta}}}_4. \quad (5.6)$$

Cancelling terms, then as $u \rightarrow 0$

$$e^{-\Phi} \left(\beta \frac{m_e}{m_i}\right)^{-1/2} = \underbrace{\frac{1}{2}}_1 + \underbrace{\frac{1}{2}}_2 + \underbrace{\frac{\Phi}{\beta}}_3 + \underbrace{0}_4. \quad (5.7)$$

Clearly then as the flow speed goes to zero the stationary OML ion current is recovered. We see that terms 1 and 2 are the are one-way flux due to thermal motion onto the grain surface. This is easily confirmed for a stationary Maxwellian by taking the ion current to simply be the one-way flux, eqn.(2.4), onto the grain surface

$$I_i = 4\pi r_d^2 \frac{1}{4} n \bar{c} = 4\pi r_d^2 \frac{1}{4} n \left(\frac{8kT_i}{\pi m_i} \right)^{1/2}. \quad (5.8)$$

Equating this with the electron current

$$\begin{aligned} 4\pi r_d^2 e \frac{1}{4} \left(\frac{8kT_i}{\pi m_i} \right)^{1/2} &= 4\pi r_d^2 e \left(\frac{kT_e}{2\pi m_e} \right)^{1/2} e^{-\Phi} \\ e^{-\Phi} \left(\beta \frac{m_e}{m_i} \right)^{-1/2} &= 1. \end{aligned} \quad (5.9)$$

This component of the ion current is herein referred to as the *thermal contribution*.

Recalling the OML ion current,

$$I_i = \sqrt{\beta \frac{m_e}{m_i}} \left(1 + \frac{\Phi}{\beta} \right), \quad (5.10)$$

the underlined term can now be understood to be the thermal contribution to the ion current. In the SOML case the thermal contribution can be found by performing the integral given by eqn.(5.2) with the potential set to zero in the cross section term.

$$I_i = 2\pi e n_i \int_0^\infty \int_0^\pi \pi r_d^2 v^3 \left(\frac{m_i}{2\pi k T_i} \right)^{3/2} \exp \left[-\frac{m_i}{2kT_i} (v^2 + w^2 - 2vw \cos \theta) \right] \sin \theta d\theta dv. \quad (5.11)$$

Equating with the electron current we find

$$e^{-\Phi} = \left(\beta \frac{m_e}{m_i} \right)^{1/2} \underbrace{\left[\frac{\sqrt{2\pi\beta}}{4u} \operatorname{erf} \left(\frac{u}{\sqrt{2\beta}} \right) + \frac{1}{2} \exp \left(-\frac{u^2}{2\beta} \right) \right]}_1 + \underbrace{\frac{u}{4} \sqrt{\frac{2\pi}{\beta}} \operatorname{erf} \left(\frac{u}{\sqrt{2\beta}} \right)}_4. \quad (5.12)$$

Terms 1, 2 and 4 are recovered but term 3 is lost. Again, terms 1 and 2 are herein referred to as the thermal contribution. We now investigate term 4.

5.1.2 Large Flow Limit

In the limit of u becoming large, when $\frac{u}{\sqrt{2\beta}} \gtrapprox 2$ then $\text{erf}(\frac{u}{\sqrt{2\beta}}) \rightarrow 1$ and we have

$$e^{-\Phi} \left(\beta \frac{m_e}{m_i} \right)^{-1/2} = \underbrace{\frac{\sqrt{2\pi\beta}}{4u}}_1 + \underbrace{\frac{1}{2} \exp\left(-\frac{u^2}{2\beta}\right)}_2 + \underbrace{\frac{\sqrt{2\pi\beta}}{2u} \frac{\Phi}{\beta}}_3 + \underbrace{\frac{u}{4} \sqrt{\frac{2\pi}{\beta}}}_4. \quad (5.13)$$

If we further increase the flow then terms 1, 2 and 3 all tend to zero

$$\lim_{u \rightarrow \gg 2} e^{-\Phi} \left(\beta \frac{m_e}{m_i} \right)^{-1/2} = \underbrace{0}_1 + \underbrace{0}_2 + \underbrace{0}_3 + \underbrace{\frac{u}{4} \sqrt{\frac{2\pi}{\beta}}}_4. \quad (5.14)$$

This is simply the ion current due to flow using the geometric cross-section of the grain. We can convince ourselves of this by equating the electron current with an ion flux of vne through the surface πr_d^2 ,

$$\begin{aligned} \pi r_d^2 vne &= 4\pi r_d^2 e \left(\frac{kT_e}{2\pi m_e} \right)^{1/2} e^{-\Phi} \\ \frac{u}{4} \sqrt{2\pi} &= \left(\frac{m_e}{m_i} \right)^{-1/2} e^{-\Phi}. \end{aligned} \quad (5.15)$$

Term 4 is herein referred to as the *flow contribution*.

5.1.3 The Potential Contribution

Finally, term 3 can be understood as the *potential contribution* to the ion current, if the potential is zero it disappears. Term 3 contains a factor of β , physically this represents the thermal motion of the ions “fighting” the pull of the potential. As β is increased the thermal contribution will be increased and the potential contribution decreased.

As a last exercise, it is interesting to determine the OML current for a monoenergetic beam and see which terms are recovered. The orbit-motion-limited current for a monoenergetic beam is trivial as it does not require an integration over velocity.

$$I_i = \sigma(v)n ev = \pi r_d^2 \left(1 - \frac{2e\phi}{m_i v^2} \right) n ev. \quad (5.16)$$

Equating this with the electron current

$$e^{-\Phi} = \frac{u}{4} \left(1 + \frac{2\Phi}{u^2} \right) \sqrt{\frac{2\pi m_e}{m_i}}. \quad (5.17)$$

Rearranging this as

$$e^{-\Phi} \left(\frac{m_e}{m_i} \right)^{-1/2} = \underbrace{\frac{\sqrt{2\pi}}{2u} 2\Phi}_{3} + \underbrace{\frac{u}{4} \sqrt{2\pi}}_{4}$$

we see eqn.(5.13) is recovered without terms 1 and 2.

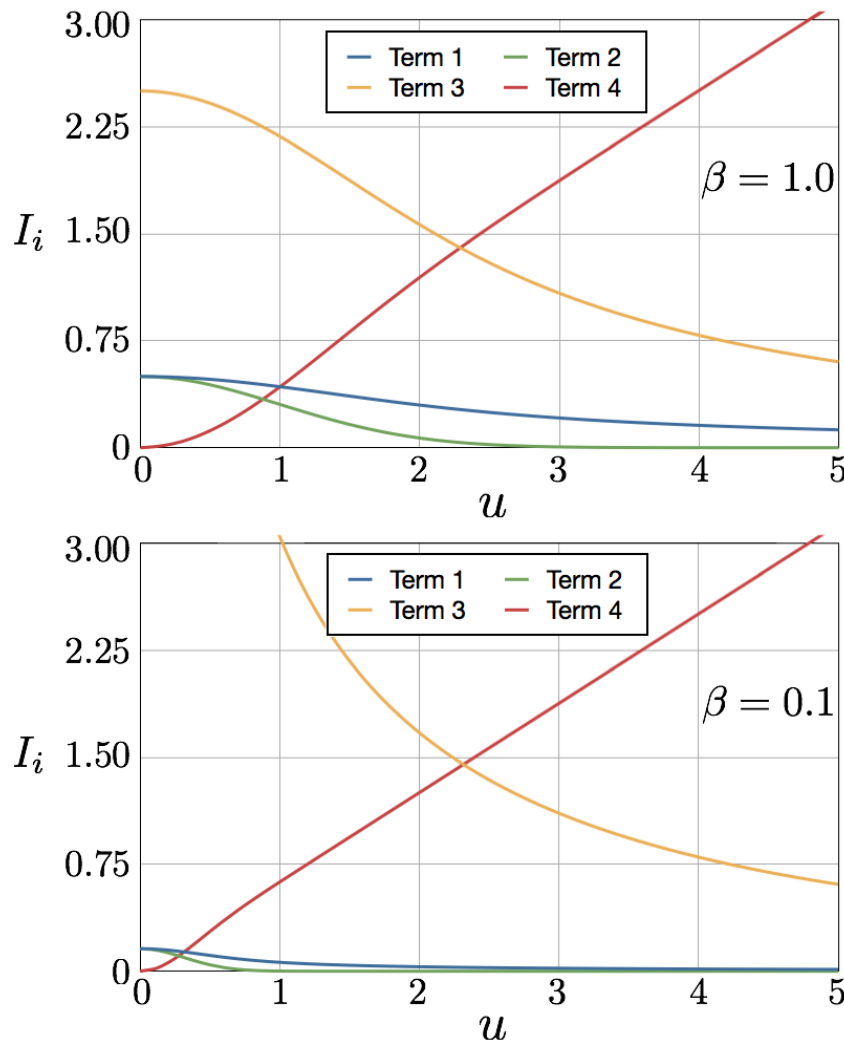


Figure 5.1.: Terms 1, 2, 3 and 4 in the soml ion current from eqn.(5.5).
 u is normalised by $\sqrt{kT_e/m_i}$ and I_i by $4\pi r_d^2 n_i e \sqrt{kT_i/2\pi m_i}$.

The potential contribution in OML “blows up” when the ion temperature goes to zero. However, providing $\frac{u}{\sqrt{2\beta}} \gtrapprox 2$, we see from eqn.(5.13) that the error function $\rightarrow 1$ and the temperature dependence in the potential contribution cancels. Terms 3 and 4 therefore reproduce the the OML monoenergetic current providing $\frac{u}{\sqrt{2\beta}} \gtrapprox 2$, that is, the flow is strong enough to dominate the thermal motion.

The four terms we have been discussing are plotted in Fig. 5.1 for $\beta = 1.0$ and 0.1 . We now know that the assumption of spherical symmetry is only required by term 3, the potential contribution. The other terms we now understand to be due to thermal motion and the plasma flow; in addition, absorption radii will only effect the contribution of term 3.

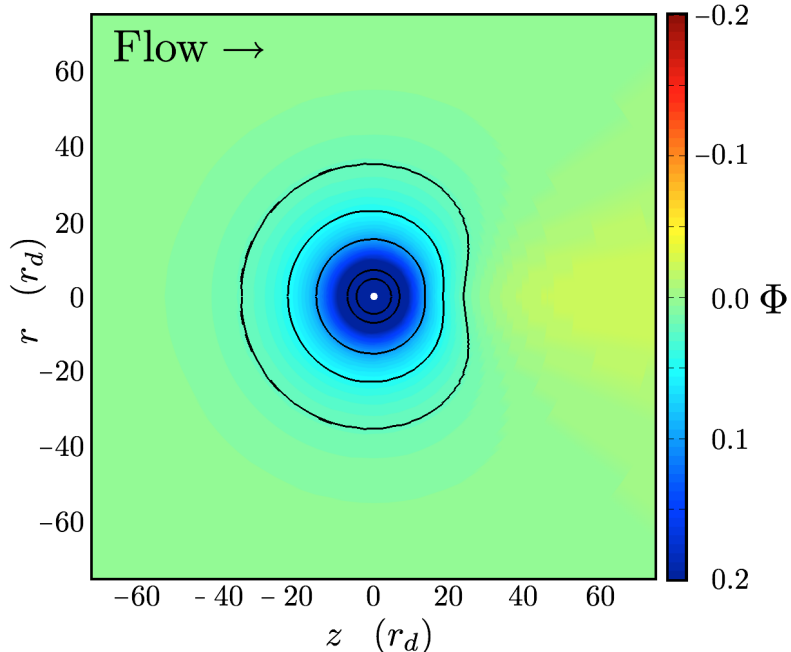


Figure 5.2.: The potential distribution around a grain of $\rho = 0.04$, $u = 3.0$ and $\beta = 0.3$. The contours indicate equipotentials, the outermost is for $\Phi = 0.02$, and moving inwards, 0.05 , 0.1 , 0.3 and 0.5 . $\Phi = -e\phi/kT_e$ and u is normalised by $\sqrt{kT_e/m_i}$.

We see from Fig. 5.1 that above some flow velocity the ion current due to the flow contribution (term 4) dominates the ion current due to the potential contribution (term 3). It is therefore reasonable to expect SOML to be correct for large flows. When the spherical symmetry of the potential distribution is lost depends strongly on ρ . Fig. 5.2 shows the potential around a small grain, $\rho = 0.04$, and clearly the symmetry is well preserved despite the large flow velocity of $u = 3.0$. For small grains the potential remains relatively spherically symmetry whilst the potential contribution is the dominant term, hence SOML remains valid. A comparison

between simulation and soml for small grains is shown in Fig. 5.3 for a range of β , the agreement is seen to be very good. As we are primarily interested in large grains we conclude that soml adequately describes the floating potential of small grains and move on.

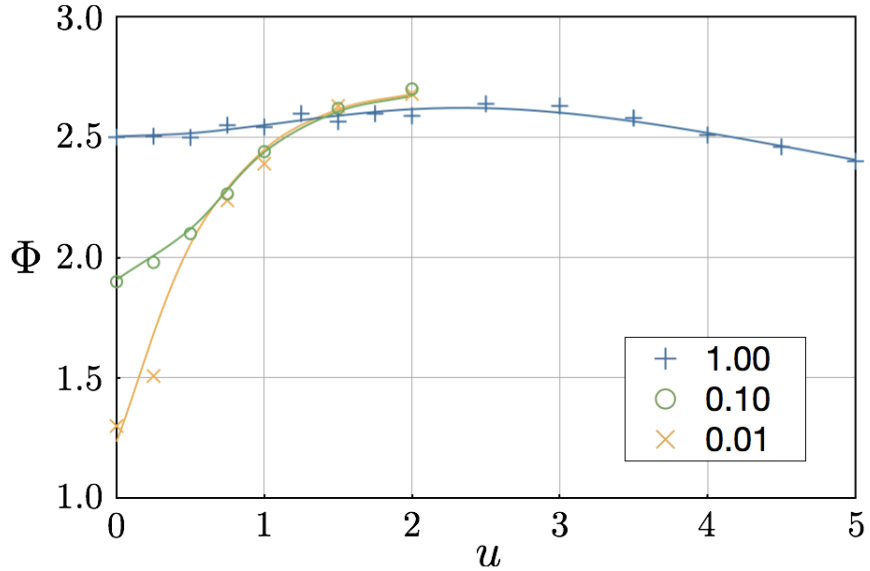


Figure 5.3.: The floating potential from SCEPTIC for small ρ ($\rho = 0.04$) as a function of flow velocity for a number of β s. The solid lines are the solutions to soml. u is normalised by $\sqrt{kT_e/m_i}$ and $\Phi = -e\phi/kT_e$.

5.2 SOML FOR LARGE GRAINS

5.2.1 The Breakdown of SOML

In the previous section we analysed the components of the soml ion current thoroughly. For small grains soml is a very good approximation due to the resilience of the potentials spherical symmetry, even with substantial flows. For large grains two problems are encountered. The first of these is that for large grains soml encounters the same problem as oml, an increasing number of ions encounter absorption radii. Simulation data reflects this, departing from the soml prediction as ρ increases, this is shown in Fig. 5.4 for $\beta = 1$. For $\rho = 0.1$ and 1.0 soml is seen to provide a good estimate of the floating potential. For $\rho = 10$ and 100 however simulation data departs strongly from soml.

The second problem is that the spherical symmetry of the potential around large grains is lost at much lower flow speeds than for small grains. The potential distribution around a large grain is shown for various flow speeds in Fig. 5.5. For $u = 0.3$ the symmetry is well maintained however, by $u = 0.9$ the potential distribution is

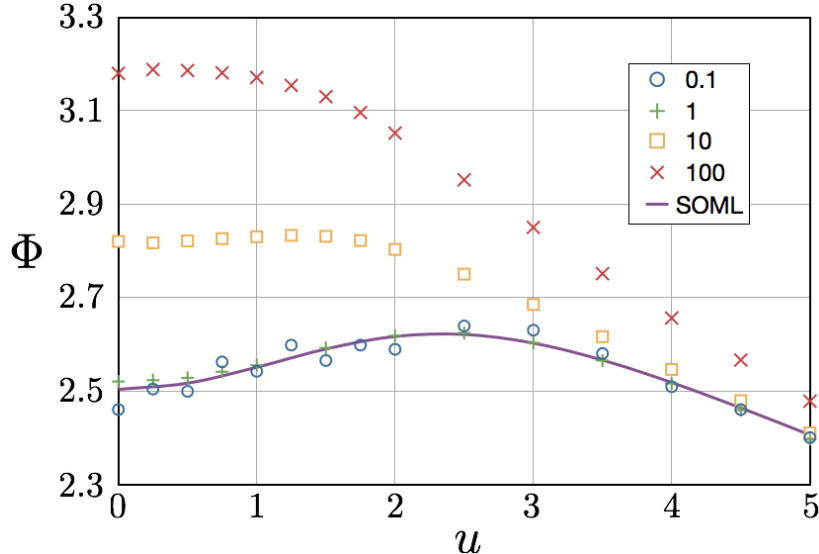


Figure 5.4.: The floating potential from SCEPTIC for various ρ (indicated on the figure) and $\beta = 1$. The solid line is SOML. u is normalised by $\sqrt{kT_e/m_i}$ and $\Phi = -e\phi/kT_e$.

distinctly skewed. In contrast, the symmetry of the potential distribution around the small grain in Fig. 5.2 is well maintained at $u = 3$.

We consider two regimes, the first being when the flow velocity is low and the potential well approximated as spherically symmetric. The second being when the potential is no longer spherically symmetric. The transition between these two regimes is smooth providing $\beta \gtrsim 0.5$, i.e. the potential is slowly deformed; for lower β the transition is alarmingly sudden. Hutchinson [73, 87] has already observed this sudden transition reporting a sudden drop in the average potential around the grain when the flow speed $u \approx 0.6$. This he attributes to the formation of an azimuthal asymmetry in the potential. By averaging the potential distribution and thus introducing an artificial symmetry he finds that the average potential evolves comparably but far more gradually. The suddenness of the transition he explains physically as being due to the ion orbits. At low flow velocities many orbits pass around the grain before returning to infinity. These returning orbits do not aid the density increase behind the grain due to ion focusing and in fact have the opposite effect and increase the density upstream. Both of these effects serve to damp any density/potential asymmetry, Fig. 5.6 illustrates this effect¹. The incoming ions all have the drift velocity and the potential is averaged azimuthally hence the orbits are to be regarded as illustrative.

¹ Fig. 7 in [87]

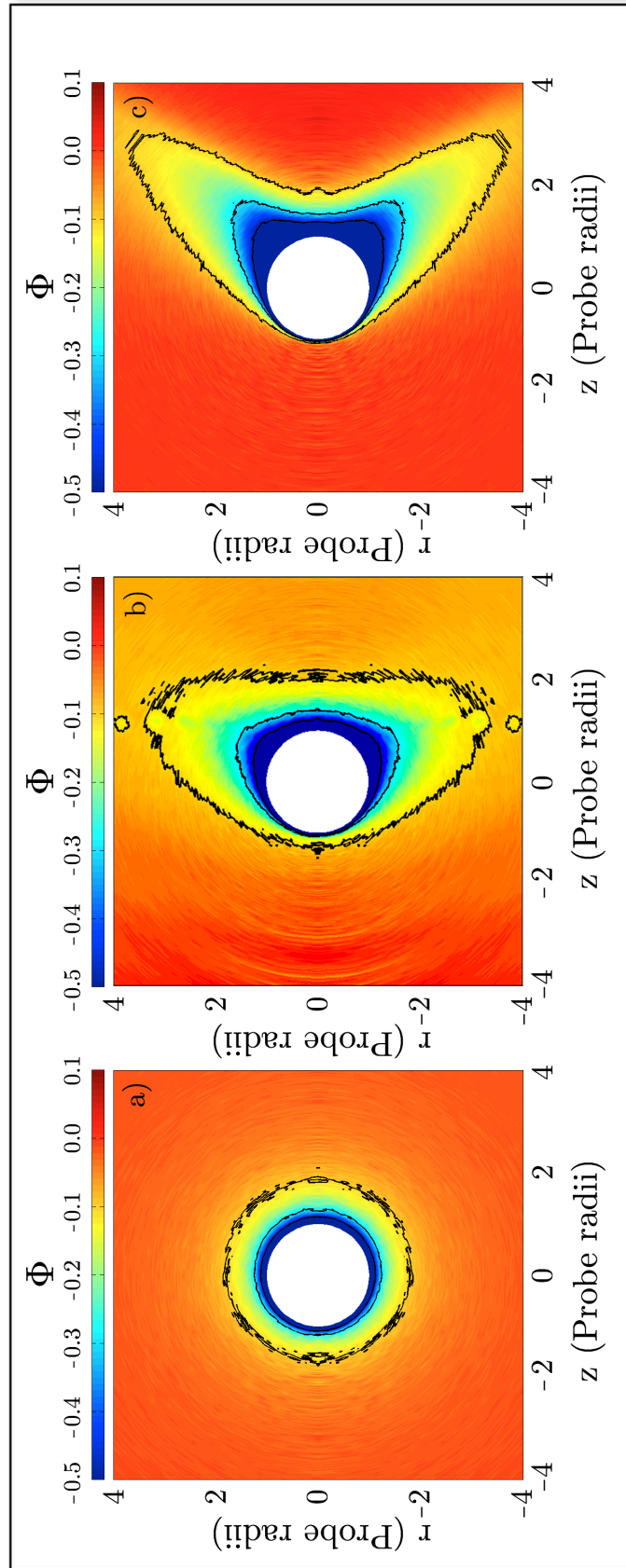


Figure 5.5.: The potential distribution around a large dust grain, $\rho = 80$, for flow speeds of a) $u = 0.3$, b) $u = 0.9$ and c) $u = 1.3$. $\beta = 0.2$. u is normalised by $\sqrt{kT_e/m_i}$ and $\Phi = -e\phi/kT_e$.

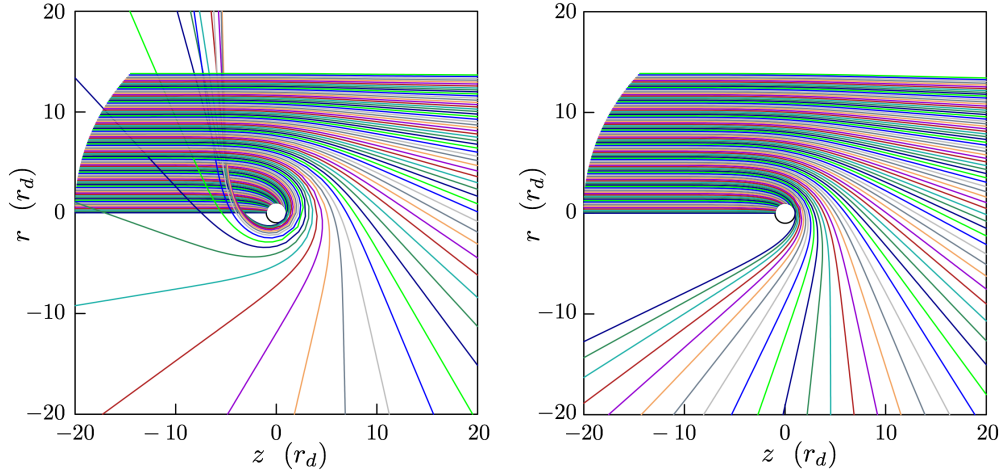


Figure 5.6.: The original is Fig. 7 in [87]. Typical ion orbits below the transition ($u = 0.5$) and above the transition ($u = 0.8$). u is normalised by $\sqrt{kT_e/m_i}$

We now modify soml as we did regular oml in the previous chapter. In the flow case we must address the absorption radii and the breakdown of the potential symmetry however, after investigating the soml ion current, we are well placed to do this.

5.2.2 Modified SOML

In section 4.1.4 we empirically fit the simulated floating potentials of dust grains of varying size, plasma species and ion temperature. Even in the stationary case, the number of independent parameters made the task a daunting one and the resulting expressions cumbersome. Introducing flow to the problem makes the empirical approach less than practical, even if the ion current varied linearly with flow velocity. Instead we look to modify soml in the same way we modified oml.

Recalling eqn.(5.5), the soml current balance is

$$e^{-\Phi} \left(\beta \frac{m_e}{m_i} \right)^{-1/2} = \underbrace{\frac{\sqrt{2\pi\beta}}{4u} \operatorname{erf}\left(\frac{u}{\sqrt{2\beta}}\right)}_1 + \underbrace{\frac{1}{2} \exp\left(-\frac{u^2}{2\beta}\right)}_2 + \underbrace{\frac{\sqrt{2\pi\beta}}{2u} \operatorname{erf}\left(\frac{u}{\sqrt{2\beta}}\right) \frac{\Phi}{\beta}}_3 + \underbrace{\frac{u}{4} \sqrt{\frac{2\pi}{\beta}} \operatorname{erf}\left(\frac{u}{\sqrt{2\beta}}\right)}_4 \quad (5.18)$$

We know that in the limit of $u \rightarrow 0$ term 3 reduces to what we have labeled the standard oml potential contribution. As such, modifying term 3 in exactly the same

way as we modified the OML case will produce the same result as in the stationary case as $u \rightarrow 0$. For low flow velocities we assume that the symmetry of the potential will be maintained and all of the absorption radii will be at or within the sheath. As in the stationary case, SOML is only applied to the presheath and we assume the potential drop across the sheath is well described by the planar wall sheath potential drop, eqn.(4.8).

$$\Phi_{\text{wall}} = \frac{1}{2} \ln \left[2\pi \frac{m_e}{m_i} (1 + \gamma\beta) \right].$$

As in the stationary case, we will try various choices for γ and see which gives the best agreement.

Including a sheath drop of $\Delta\Phi$ in the SOML ion current

$$e^{-\Phi} = \sqrt{\beta \frac{m_e}{m_i}} \left[\frac{\sqrt{2\pi\beta}}{4u} \left(1 + \frac{u^2}{\beta} \right) \operatorname{erf}\left(\frac{u}{\sqrt{2\beta}}\right) + \frac{1}{2} \exp\left(-\frac{u^2}{2\beta}\right) + \sqrt{\frac{\pi\beta}{2u^2}} \operatorname{erf}\left(\frac{u}{\sqrt{2\beta}}\right) \frac{\Phi - \Delta\Phi}{\beta} \right]. \quad (5.19)$$

In the limit of small flow we expect this modified SOML to be a good approximation. Unaccounted for absorption radii will produce the same error as in the stationary case. The maximum discrepancy is therefore expected to be for low β and approximately 10%.

The second problem is that of the breakdown of spherical symmetry at much lower flow velocities than in the small grain case. The potential contribution (term 3), seen in Fig. 5.1, dominates the flow contribution (term 4) up to $u \approx 2.3$ in the normal SOML case. For large dust grains the potential symmetry is lost at much lower flow speeds, as seen in Fig. 5.5. Critically, our modification to term 3 in modifying SOML significantly lowers the ion current contribution of the potential. Plotting the SOML ion current terms and comparing term 3 with the modified term 3, we see that the flow contribution dominates the potential contribution at a much lower value of u , this is shown in Fig. 5.7 for $\beta = 0.1$. We see from Fig. 5.7 that the flow contribution in modified SOML dominates the potential contribution at $u \approx 1.1$ for the case of $\beta = 0.1$. In effect, the range of flow speeds over which the assumption of a spherically symmetric potential is important has been reduced.

To recap, modified SOML is expected to estimate the potential well for $u \lesssim 0.5$, here the symmetry of the potential is well maintained and the majority of the error is due to the unaccounted for absorption radii in the presheath. For $u \gtrsim 1.5$ the ion current is dominated by the flow contribution and modified SOML is again expected

to be a good approximation. The region where modified SOML may be expected to fall down is $u \approx 1$. However, in this region the potential, particularly for low β , undergoes a transition between relatively spherically symmetric and strongly asymmetric [73]. Our simple model does not attempt to predict this behaviour and errors are to be expected here.

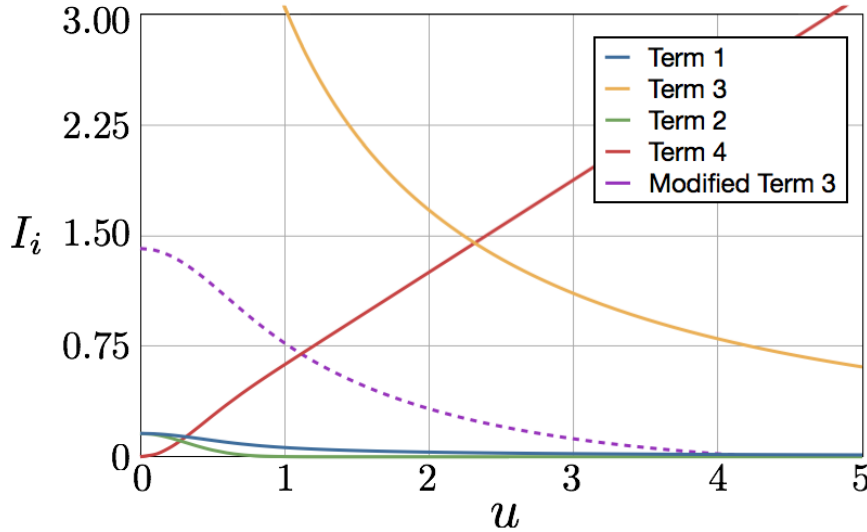


Figure 5.7.: Terms 1, 2, 3, 4 (from eqn.(5.5)) and the modified version of term 3, $\beta = 0.1$. u is normalised by $\sqrt{kT_e/m_i}$ and I_i by $4\pi r_d^2 n_i e \sqrt{kT_i/2\pi m_i}$.

5.2.3 Comparison with Simulation

We now compare modified SOML with simulation results. Figure 5.8 shows the case of $\beta = 1.0$ and $\rho = 100$. The solution to the modified SOML equation, eqn.(5.19), is shown for a number of γ s. The value of γ required to follow simulation data more closely is a function of the flow speed. Clearly modified SOML describes the floating potential as a function of flow velocity much more accurately than normal SOML, also shown, in this case. We choose $\gamma = 5/3$ in the subsequent results.

To begin with we investigate the case for $\beta \geq 1$. Here the absorption radii are expected to be at or within the sheath edge (hence we expect good agreement between simulation and modified SOML) and the spherical symmetry to be maintained to flow velocities approaching $u = 1$. The transition between symmetric and asymmetric potentials is gradual at these ratios of β . A comparison between eqn.(5.19) and SCEPTIC for $\beta = 1.0$ and 10.0 is shown in Fig. 5.9. Despite the simplifying assumptions, the agreement is good, particularly for flow velocities less than $u \approx 2$. For larger flows there is a small deviation attributed to the breakdown of

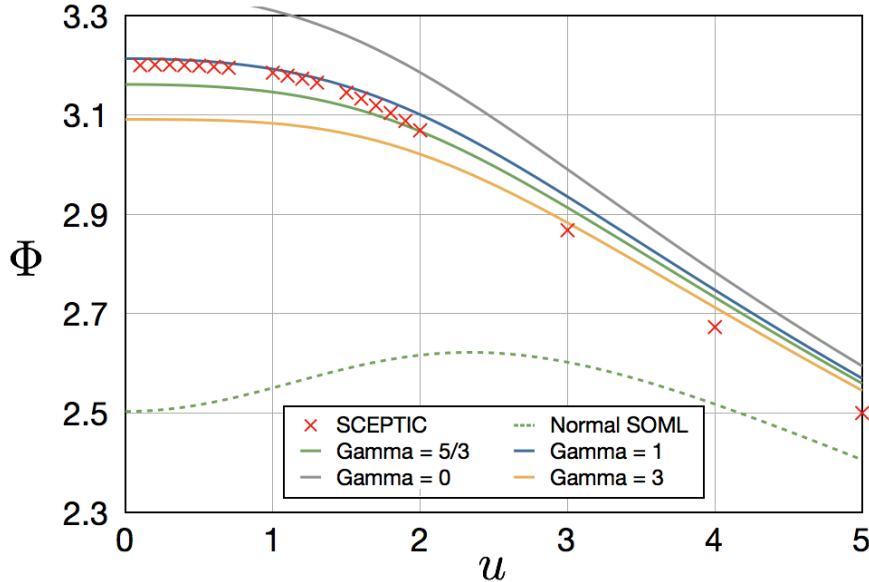


Figure 5.8.: SCEPTIC values for the floating potential of a large dust grain in a flowing plasma. The solid lines are the solutions to eqn.(5.19) for various γ , the dashed line is normal SOML, $\beta = 1.0$ and $\rho = 100$. $\Phi = -e\phi/kT_e$ and the flow speed u is normalised by $\sqrt{kT_e/m_i}$.

the symmetry assumption. Normal SOML is shown, as well as the floating potential assuming the ions to be hot/cold and ignoring the electric field. Referring back to eqn.(5.18), assuming the ions are hot but ignore the electric field amounts to using terms 1, 2 and 4 for the ion current. If the ions are assumed to be cold and ignoring the electric field, only term 4 is required. The three lines converge for large flows as electrostatic and thermal motion effects are dominated by the flow.

For the case of $\beta < 1.0$ the problem is complicated both by the absorption radii and the sudden transition from symmetric to asymmetric potential distribution, as mentioned earlier. Fig. 5.5 shows the azimuthal symmetry breakdown in the potential for $\beta = 0.2$. Hence, for some $u \lesssim 1.0$ we expect a sudden transition from the potential dominated regime to the flow dominated regime for these low β cases. For low flow velocities, absorption radii are expected to produce an error of $\lesssim 10\%$ as in the stationary case. Fig. 5.10 shows the comparison between eqn.(5.19), SOML and hot/cold ions ignoring the electric field for $\beta = 0.1$ and 0.01 . At low flow speeds the agreement between SCEPTIC and eqn.(5.19) is good, with some error due to absorption radii. For both $\beta = 0.01$ and 0.1 a pronounced change in the behaviour of the floating potential is seen at some flow velocity $u \lesssim 1.0$ and this is attributed to the sudden change in regime which our simple model does not include. The $\beta = 0.01$ case is ‘noisy’ due to the code being susceptible to numerical heating for very low ion temperatures. For $\beta = 0.1$ the floating potential varies more smoothly but also undergoes a dramatic change in behaviour. The lower the ion temperature the lower the value of u at which this happens. Our modified SOML

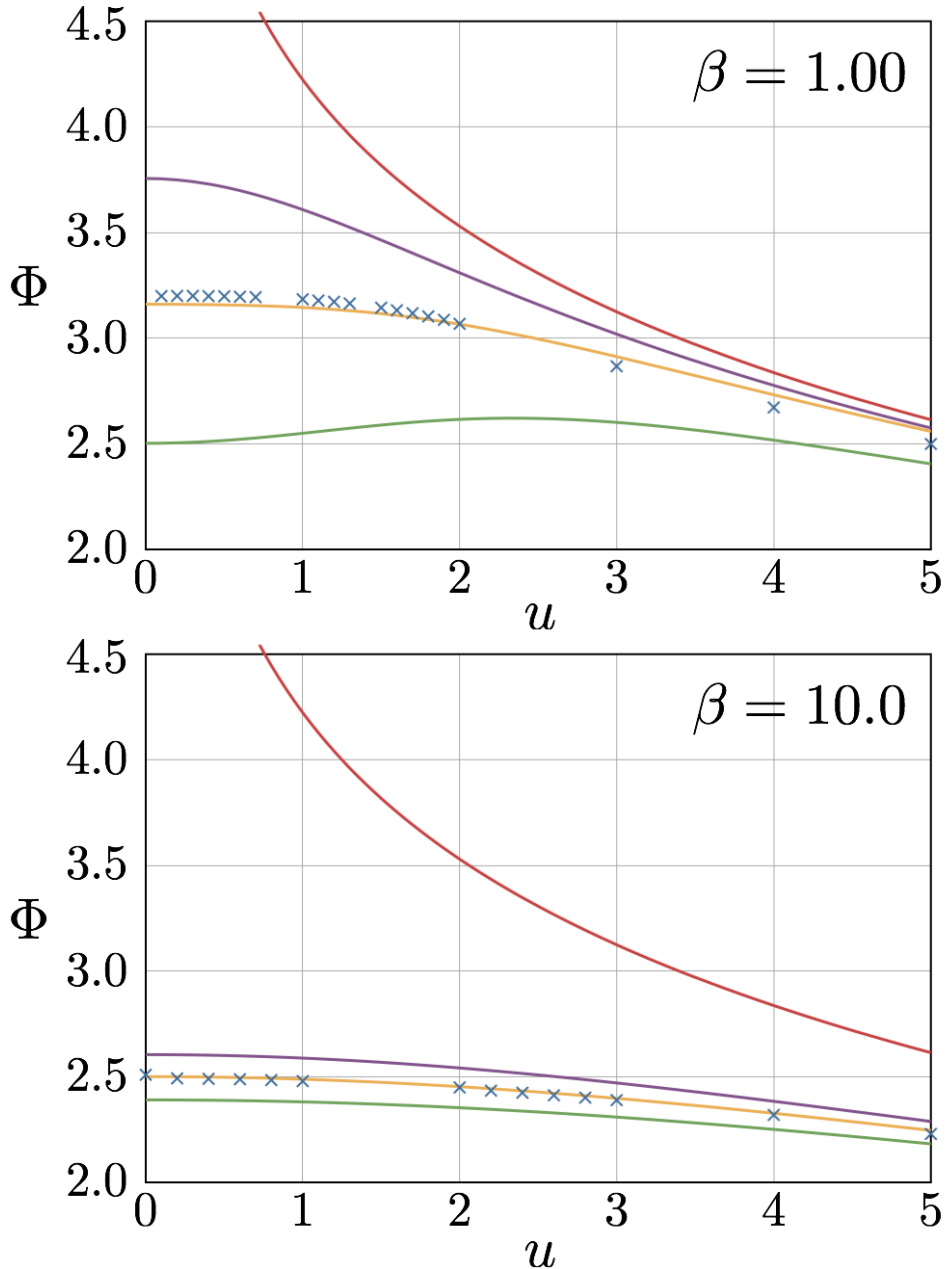


Figure 5.9.: SCEPTIC values (\times) for the floating potential of a large dust grain in a flowing plasma. The topmost, red and purple lines assume the ions are cold/hot respectively, and ignore the electric field. The middle, yellow line is modified soml, eqn.(5.19) with $\Delta\Phi$ from eqn.(4.8), and the bottom, green line is soml. $\rho = 100$, u is normalised by $\sqrt{kT_e/m_i}$ and $\Phi = -e\phi/kT_e$.

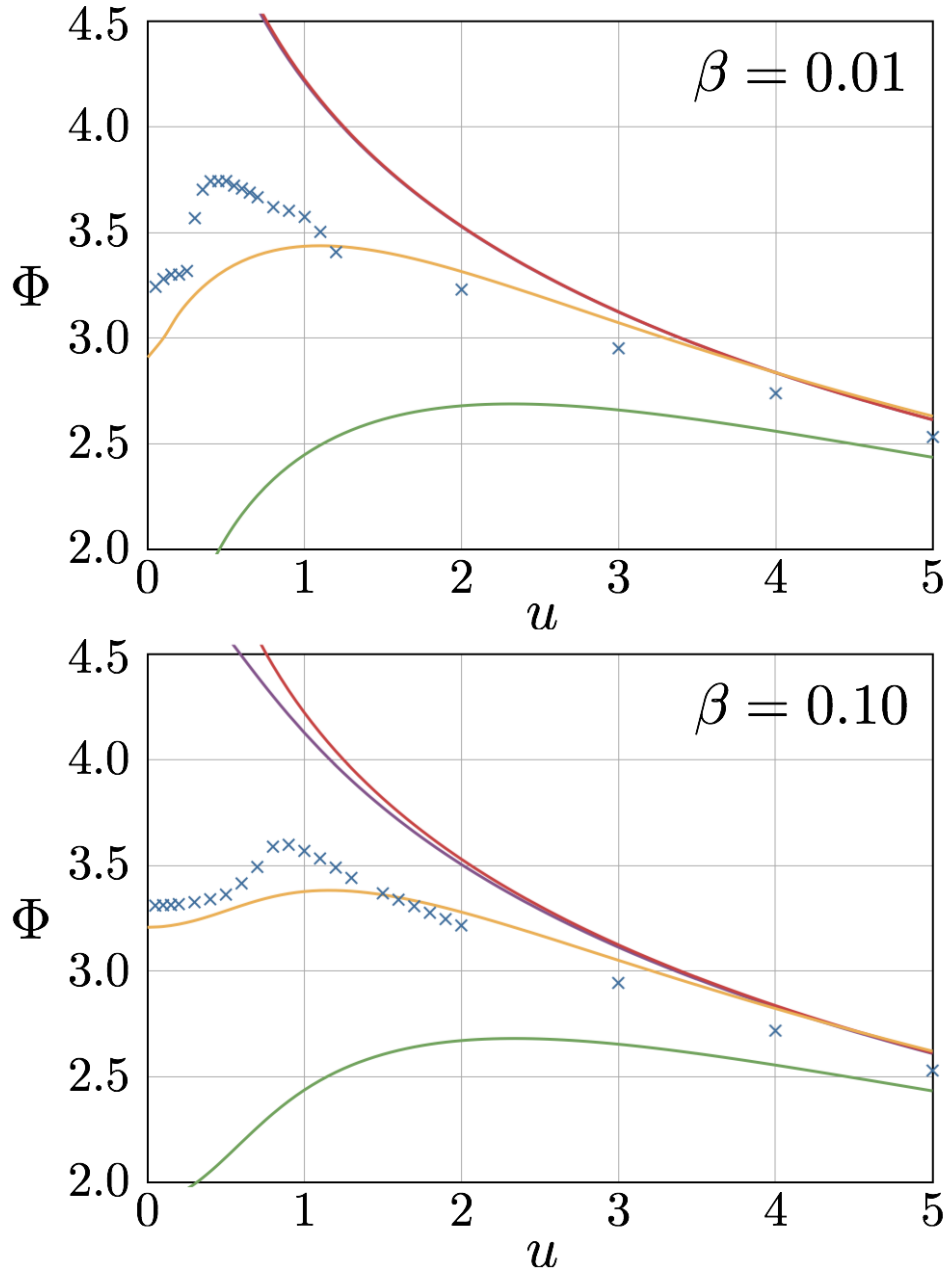


Figure 5.10.: SCEPTIC values (\times) for the floating potential of a large dust grain in a flowing plasma. The topmost, red and purple lines assume the ions are cold/hot respectively, and ignore the electric field. The middle, yellow line is modified soml, eqn.(5.19) with $\Delta\Phi$ from eqn.(4.8), and the bottom, green line is soml. $\rho = 100$, u is normalised by $\sqrt{kT_e/m_i}$ and $\Phi = -e\phi/kT_e$.

does not closely reproduce this non-linear behaviour however, it does follow the data's general trend and provides a much better estimate of the floating potential than normal SOML.

Modified SOML is compared with simulation data for a large dust grain in a helium plasma in Fig. 5.11 for $\beta = 1.0$, normal SOML is also included. We see that modified SOML again gives a much better representation of the data.

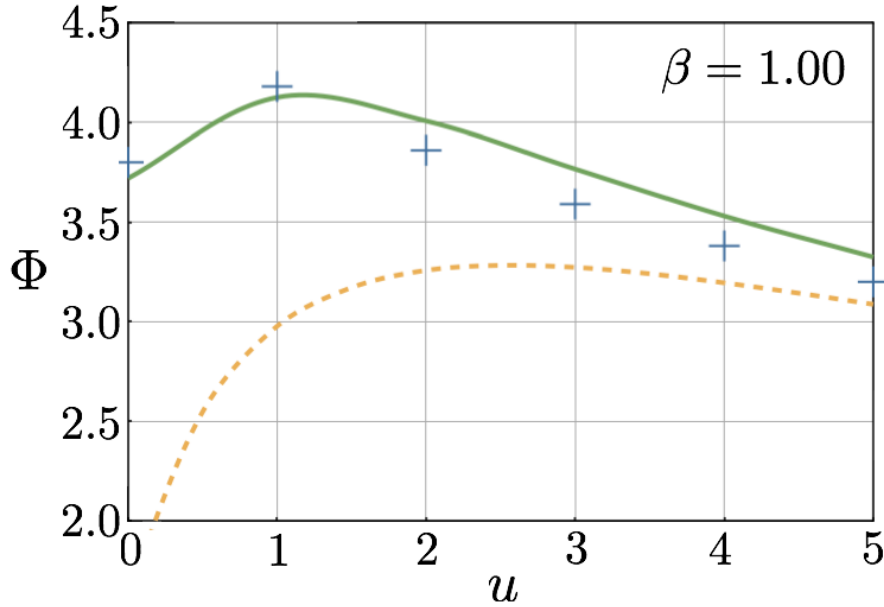


Figure 5.11.: Floating potential of a large grain in a helium plasma. $\beta = 1.0$, $\rho = 80$. The dashed line is normal SOML, the solid line is modified SOML, eqn.(5.19), and (+) is data from SCEPTIC. u is normalised by $\sqrt{kT_e/m_i}$ and $\Phi = -e\phi/kT_e$.

5.2.4 Intermediate Values of ρ

As with the stationary OML case, section 4.2.3, we describe the transition region by introducing a ρ dependence in $\Delta\Phi$. As before, $\rho_{upper} = 50$ is taken as the thin sheath limit. The SOML limit, $\rho_{lower} = 1.25\beta^{0.4}$ in the stationary case, now requires a dependence on u . This is simply understood, when the flow term sufficiently dominates the other contributions normal SOML may be used as the result is equivalent to a monoenergetic beam with a cross section of πr_d^2 . Analysing the departure of the simulated floating potential from the SOML prediction leads to an empirically found upper limit on when SOML can be used of

$$\rho_{SOML} = 1.25\beta^{0.4} + 0.37u^{2.1}. \quad (5.20)$$

This is then ρ_{lower} in

$$\Delta\Phi(\rho) = \Delta\Phi\left(\frac{\ln(\rho/\rho_{\text{upper}})}{\ln(\rho_{\text{upper}}/\rho_{\text{lower}})} + 1\right). \quad (5.21)$$

Resulting in

$$\begin{aligned} e^{-\Phi} = & \sqrt{\beta \frac{m_e}{m_i}} \left[\frac{\sqrt{2\pi\beta}}{4u} \left(1 + \frac{u^2}{\beta} \right) \operatorname{erf}\left(\frac{u}{\sqrt{2\beta}}\right) \right. \\ & \left. + \frac{1}{2} \exp\left(-\frac{u^2}{2\beta}\right) + \sqrt{\frac{\pi\beta}{2u^2}} \operatorname{erf}\left(\frac{u}{\sqrt{2\beta}}\right) \frac{\Phi - \Delta\Phi(\rho)}{\beta} \right]. \end{aligned} \quad (5.22)$$

5.3 COMPARISON WITH EXPERIMENT

The majority of prior work in this field is for grains much smaller than the Debye length. This makes our predictions of the floating potential difficult to test. Meltzer *et al* [88] and Trottenberg *et al* [89] have measured the charge of small grains experimentally. In both of these experiments the dust is suspended in the sheath of a radio-frequency discharge. Comparison is difficult as the plasma conditions experienced by the dust here are considerably different from those in the bulk plasma, primarily due to the directed ion flow required to satisfy the Bohm criterion at the sheath edge of the discharge. Similar work in a direct current discharge has been performed by Fortov *et al* [90], here the charge is given as a function of grain size but still for small grains. Walch *et al* [91] investigated the charge of grains in the bulk plasma by dropping dust into a plasma filled chamber and allowing it to fall under gravity into a Faraday cup located at the bottom of the experiment. Again the dust is much smaller than the Debye length making comparison difficult. Similarly, other approaches, both analytic [92, 93] and computational [94, 95], with which we may compare are only valid for small grains. Alternatively we could look to the potential measurements made by spacecraft. The size of a spacecraft may be larger than the Debye length however, the potential can vary strongly depending on the nature of the craft [96]. Further difficulties arise as the parameters of the surrounding plasma are unknown.

5.4 SUMMARY

A simple modification to the well known SOML model has been presented. It allows the floating potential of objects large with respect to the electron Debye length to be calculated in a flowing plasma. This is achieved by assuming all absorption radii to be at or within the sheath edge. A simple planar wall model is used to describe the

sheath drop and SOML is used to describe the potential drop across the presheath where the potential varies slowly. The results presented in Figs. 5.9 and 5.10 clearly show that modified SOML provides a much better approximation of the floating potential of large grains than normal SOML.

An empirically derived limit, eqn.(5.20), dependent on ρ and u is used to indicate when the grain is small enough to allow OML/SOML to be used reliably. Specifying modified OML/SOML to be used in the large grain limit of $\rho > 50$, an expression is also given to determine the floating potential between these two regions, eqn.(5.22).

MACH CONES

Wake effects are encountered in many areas of physics with varying length scales and complexity. The effect of an object in a stream of neutral gas moving with supersonic flow velocity is one of the most important and well studied problems of compressible hydrodynamics, not least because of its application to supersonic flight. As is well known, for an object immersed in a supersonic flow there are two distinct regions. Upstream there is a “zone of silence” which is unaffected by the presence of the object, downstream is a roughly conical region in which the flow is considerably modified. This latter region is usually termed the “Mach cone”, although it only forms a true cone with a sharp vertex for a pointed object aligned with the flow.

In the corresponding dusty plasma situation, complex wake effects have been observed in dust crystal lattices [15, 18] and investigated theoretically [97]. In the case of a single small object immersed in a supersonically flowing plasma, simulations have suggested interesting and complicated wake behaviour [98][99]. The motion of the dust relative to the plasma may be supersonic in a number of situations ranging from astrophysical dust and spacecraft, to dust present in fusion devices such as tokamaks and stellarators. It has become customary to use the term “Mach cone” rather indiscriminately to describe the wake phenomenon in these situations. Detailed simulations of such structures show that the Mach cones formed in neutral gas and plasma have significant differences. These differences reflect underlying differences in the basic physics of the interaction between the object and the high velocity medium. The study of this problem is important for many practical reasons ranging from industrial application to fusion. As we saw in §4 and §5, the problem of dust charging is non-trivial, plasma temperature and constituent components, dust grain size, temperature and velocity all play critical roles.

Miloch [100] has investigated grains with radii similar to the Debye length using a PIC code, and we find similar results using SCEPTIC. An example of the potential around a dust grain of $\rho = 1$ ($\rho = r_d/\lambda_D$) is shown in Fig. 6.1. The potential around the grain is seen to extend out to a number of grain radii as well as persisting for some distance in two tails behind the grain. In addition, a region of positive potential is seen directly behind the grain due to focussing of the ions. This ion

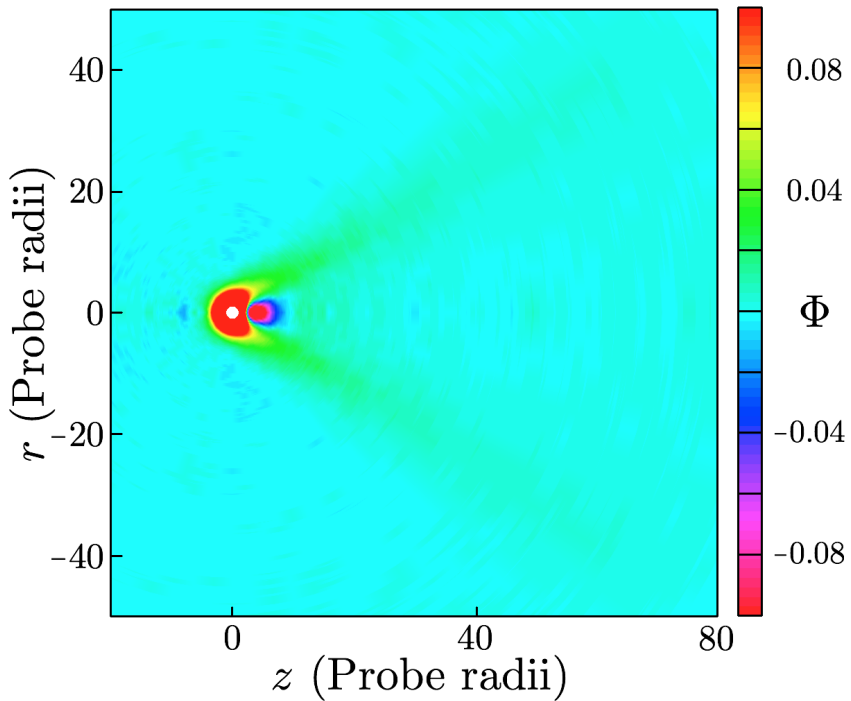


Figure 6.1.: The potential around a grain of $\rho = 1$ in a flowing plasma, $u = 2.5$ and $\beta = 0.3$. A region of positive space charge is seen directly behind the grain.
 $\Phi = -e\phi/kT_e$ and u is normalised by $\sqrt{kT_e/m_i}$.

focussing has been used in experiments investigating the interaction of two grains, one sitting in the wake of another [101]. A laser is used to push one grain and the other is seen to follow. The wake behind multiple grains has also been studied computationally. Melandø and Goree [102] observed an ion rarefaction wake followed by a region of ion focus when the flow is supersonic leading to a dipole. Miloch *et al* [103] include photoemission and find regimes where multiple grains coagulate. The wake behind non-spherical grains has also been studied [104, 105, 106] with complex wakes observed, if the inter-grain distance is less than a Debye length the two objects form a single wake. The above experimental, computational and analytic work [107] typically assumes small or point like particles, that is $r_d \ll \lambda_D$. We are primarily concerned with the opposite limit.

We now investigate the problem of a single dust grain with radius much larger than the electron Debye length, that is $\rho \gg 1$ [108]. Due to recombination at the dust grain surface the grain is effectively absorbing. The ions are warm and collisionless and the electrons are isothermal.

6.1 THE WARM ION SOUND SPEED

We introduced the problem of the warm ion sound speed in §1. In order to close the chain of fluid equations¹ requires an assumption, e.g. the adiabatic approximation $pV^\gamma = \text{constant}$ (p is the pressure, V the volume and γ the ratio of specific heat capacities). This is only strictly justified when the system is in thermal equilibrium. In order to calculate quantities of a system not in thermal equilibrium kinetic theory can be applied. However, this is typically difficult. It is common practise to use the hydrodynamic approach, especially with the adiabatic-fluid approximation [46, 113].

As noted in §1, the additional pressure term due to the warm ions in the fluid description leads to a sound speed of

$$c_{\text{hot}} = \sqrt{\frac{kT_e + \gamma_i kT_i}{m_i}}. \quad (6.1)$$

Kuhn *et al* [113] treat a 1D plasma in contact with a wall via two different kinetic approaches. They show that the usual approach of closing the fluid equations with a constant γ polytropic law may in some cases be wrong. In both of their models they find γ varies spatially and can take a wide range of values.

6.1.1 The Generalised Bohm Criterion

Continuing the discussion of the sound speed we look more closely at the Generalised Bohm Criterion (GBC). We quoted the GBC in §2 but did not discuss it in detail. As we are interested in the case of flowing plasmas we now look to satisfy the GBC starting with a shifted Maxwellian distribution.

Recalling the Generalised Bohm Criterion,

$$\int_0^\infty \frac{f_i(v)}{v^2} dv \leq \frac{m_i}{kT_e},$$

we see immediately that it can never be satisfied with a shifted Maxwellian,

$$f_{\text{Max}}^{\text{1D}}(v_x) = \sqrt{\frac{m_i}{2\pi kT_i}} \exp\left(-\frac{m(v_x - u)^2}{2kT_i}\right).$$

A shifted Maxwellian will always have a finite value of $f(0)$ causing the integral to diverge. Regardless of the flow speed, a presheath is required to accelerate the ions to satisfy the GBC. Taking a crass model in 1D we assume the ion distribution of the

¹ See A.1 for details

background plasma to be a shifted Maxwellian at the start of the presheath. The ions are accelerated through some potential $\delta\phi$ towards the sheath. At the sheath edge the distribution function has the form²

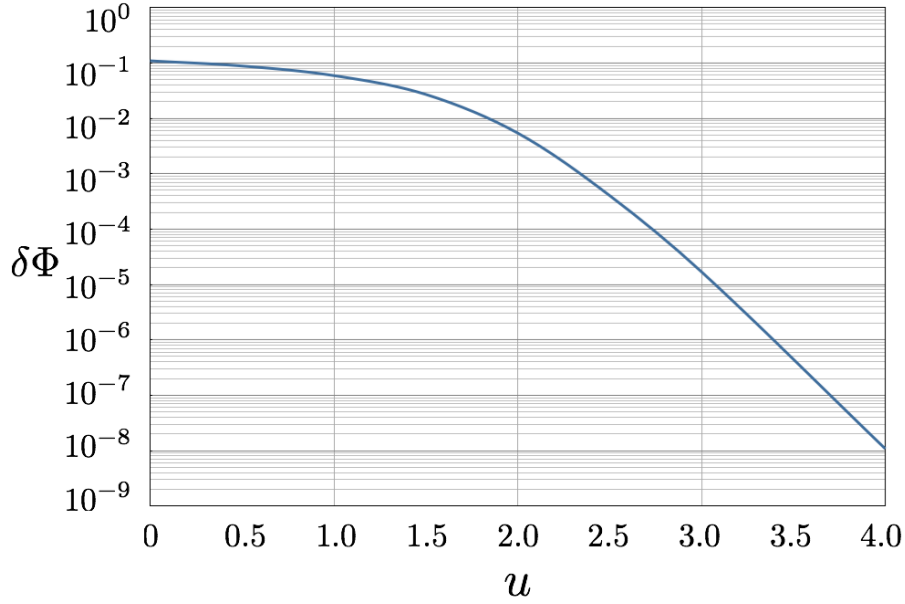


Figure 6.2.: The potential required to satisfy the Generalised Bohm Criterion for a shifted Maxwellian as a function of flow velocity. u is the flow velocity normalised by $\sqrt{kT_e/m_i}$, $\beta = 1.0$ and $\delta\Phi = -e\delta\phi/kT_e$.

$$f_{Max}^{1D}(v) = \sqrt{\frac{1}{2\pi\beta}} \exp\left(-\frac{(\sqrt{(v^2 - 2\delta\Phi)} - u)^2}{2\beta}\right),$$

the velocities are normalised by $(kT_e/m_i)^{1/2}$.

The potential drop, $\delta\Phi$, required to satisfy the GBC as a function of flow speed u is found by solving

$$\int_0^\infty \frac{\sqrt{\frac{1}{2\pi\beta}} \exp\left(-\frac{(\sqrt{(v^2 - 2\delta\Phi)} - u)^2}{2\beta}\right)}{v^2} dv = 1.$$

The required potential is plotted as a function of the flow velocity in Fig. 6.2 on a logarithmic axis. As expected, we see that although the potential drop required in the presheath does not go to zero, it becomes extremely small as virtually no ions are left at low flow speeds for highly shifted Maxwellians.

² See Appendix C.2.

We now look at simulation results for large dust grains in strongly flowing plasmas and begin by summarising the major differences between plasma immersed dust and an object in a neutral gas.

6.2 DIFFERENCES: DUST IMMERSED IN A PLASMA/NEUTRAL GAS

In the neutral gas case a shock is present at the Mach cone, in the plasma case this boundary is not a shock. In the neutral gas case there is a standoff distance in front of a blunt object, like a sphere, and the bow shock starts here. For large objects in the plasma case the observed cones are truncated and start on the grain surface. In the neutral case the flow must move around the object, in the plasma case the flow impinging on the grain is effectively absorbed as recombination takes place. These differences are illustrated schematically in Fig. 6.3.

In addition there are two further important differences. Firstly, in the neutral case a second shock may be seen downstream due to converging flow. In the plasma case a single cone is seen at high ion temperatures, but for $\beta \lesssim 0.5$ two “nested” cones are always observed. Finally, in the neutral case the shock extends over large distances, whereas the plasma cones extend for a few grain radii before being damped away.

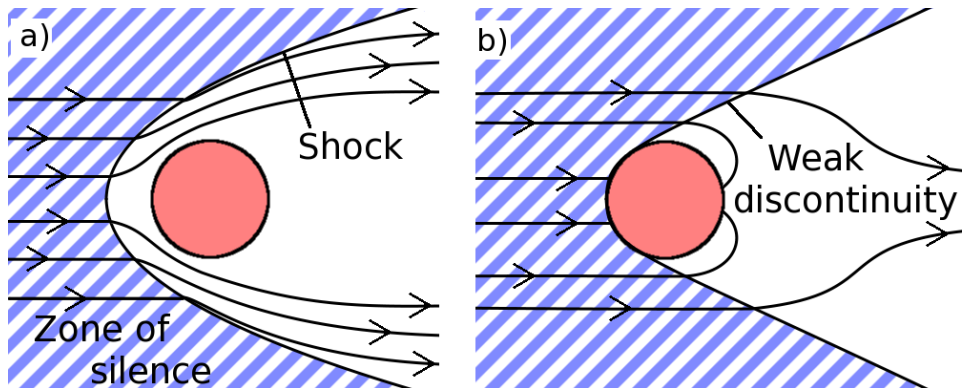


Figure 6.3.: Schematic representation of the flow pattern in a) the conventional case of an object in supersonic flow and b) an absorbing dust grain in supersonic flow.

These differences are due to the following key underlying differences. In the neutral gas case the interaction is mediated by gas pressure, in the plasma the interaction is mediated by electrostatic fields. As mentioned above, in the plasma case the object is perfectly absorbing hence no density build up is possible in front of the object. In the neutral case gas impinges directly onto an object, in the plasma case the upstream, quasineutral plasma is separated from the object by a thin sheath of positive space charge. Finally, in the neutral case the characteristic velocity is the sound speed. For the plasma, the characteristic velocity is the Bohm speed/ion

acoustic speed although it is unclear *a priori* what value this takes for the case of warm ions, considered here.

6.2.1 The Effect of Ion Temperature

As noted, the ion temperature is critical in determining the downstream plasma behaviour. We can reproduce this single/double cone transition with a simplistic model. This “toy” model (the following are not results from SCEPTIC) does not aim to encompass all the effects present, or include any individual effects precisely, it is simply a means of illustrating the effect of the thermal motion on the convergence of the ion stream behind a large dust grain.

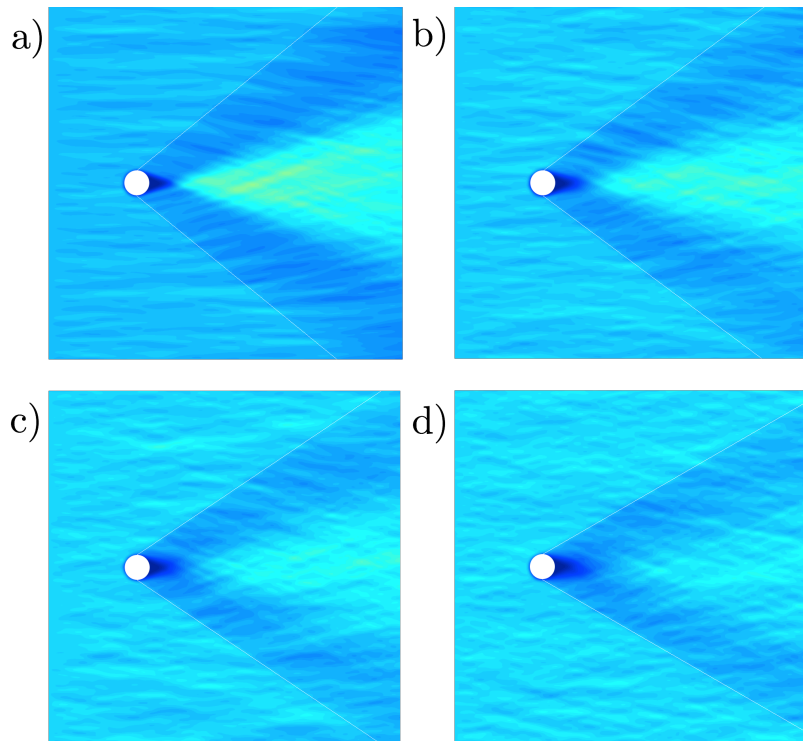


Figure 6.4.: Simple model of ion flow past a dust grain, as the amount of random motion is increased the double cone is lost. The random component is a) 10%, b) 20%, c) 40% and d) 50% of the flow speed.

Starting ions upstream of a dust grain, all with the same flow velocity, we advance them towards an absorbing grain. A Mach cone, formed due to information about the object only being allowed to travel at the sound speed, has a half angle θ given by $\sin(\theta) = c_s/u$ (c_s is the speed of sound and u the flow speed of the medium in relation to the object). We reproduce the effects of the dust grain, as seen in simulation, by defining some Mach angle in relation to the grain³. As the

³ Specifically the Mach angle in our toy model is given by $\sin \theta = c_{\text{hot}}/u$ where $c_{\text{hot}} = \sqrt{1 + 3\beta^+}$ and β^+ is the pseudo-thermal motion.

streaming ions enter this Mach cone region they receive a single “kick” in their velocity towards the grain. This kick is inversely proportional to the square of their distance from the grain to represent the reduction in the potential as we move away from the grain. Initially the ions are given a random component of velocity, transverse to the flow direction, which acts as a pseudo-thermal motion. The ion

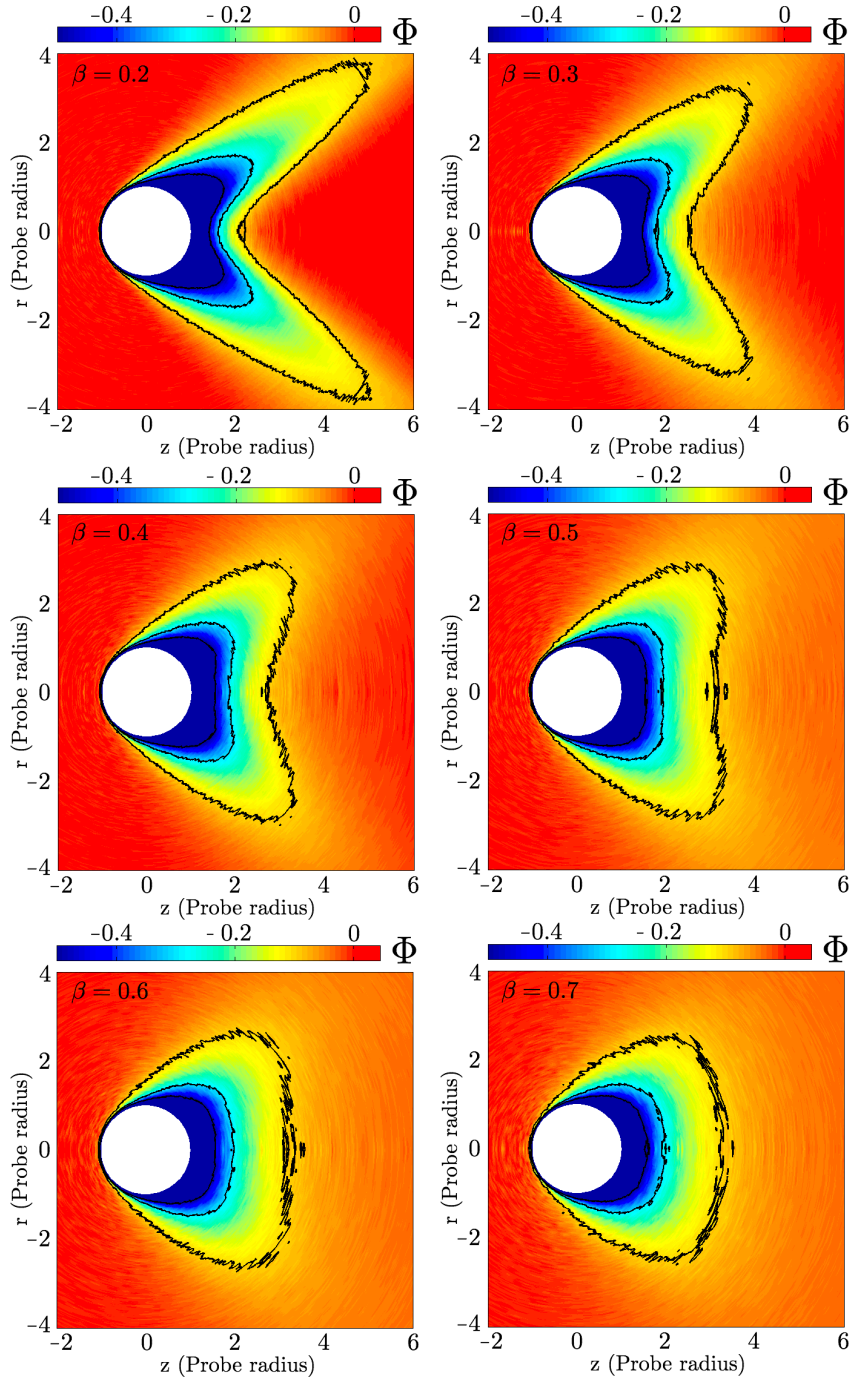


Figure 6.5.: The transition from double to single cone for $\beta = 0.2$ to $\beta = 0.7$. The flow velocity is $1.75\sqrt{kT_e/m_i}$ and the grain radius is $\rho = 80$. $\Phi = -e\phi/kT_e$.

density given by this toy model is shown in Fig. 6.4. We see that when the thermal motion is small a primary and secondary cone are clearly distinguishable due to the converging ion streams. As the amount of random motion is increased the second cone is seen to diminish. It appears therefore that much of the structure may be attributed to the convergence of the flow behind the grain.

The series of figures in Fig. 6.5 are from SCEPTIC simulations. They illustrate the transition between single and double cone as ion temperature is varied. Each of the figures is for a flow speed of $1.75\sqrt{kT_e/m_i}$ however, as the ion temperature is increased, the sound speed is also increased hence the Mach angle is expected to vary.

6.3 A HYDRODYNAMIC ANALOG

We now examine these results in more detail. For a stationary plasma the sheath and presheath around a dust grain are spherically symmetric. As flow is introduced the spherical symmetry of the presheath is lost as the presheath is deformed. For supersonic flows a well defined, truncated Mach cone is seen, the form of this cone is dependent on the ion temperature. For $\beta \gtrsim 0.5$ a single Mach cone forms, for lower ion temperatures a double cone is seen, Fig. 6.6. Wake structures and rarefaction cones have previously been observed with SCEPTIC [72] but not explored in detail. We are primarily concerned with low ion temperatures and double cones. The inner cone can be seen to begin at some point behind the grain. As already

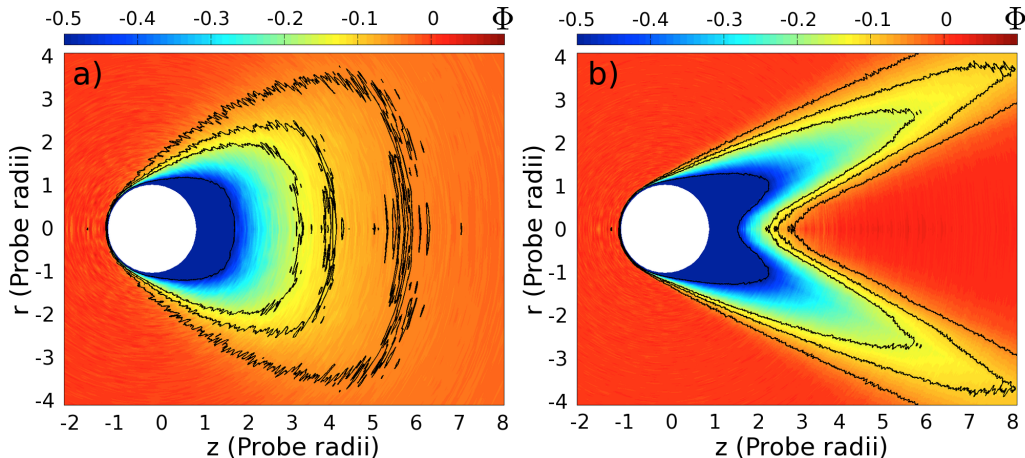


Figure 6.6.: Potential distribution Φ a) Single cone: $\beta = 1.0$, $\rho = 80$, $u = 2.5$. b) Double cone: $\beta = 0.2$, $\rho = 80$, $u = 2.5$. u is normalised by $\sqrt{kT_e/m_i}$.

noted, the outer cone is not a conventional shock wave as the density and velocity vary smoothly across the cone i.e. there are no jumps at the cone boundary. Fig. 6.7 shows the ion density and z component of velocity at $z = 2$. These quantities are

seen to vary smoothly everywhere. This is a critical point, both cones are more akin to weak discontinuities [109] but with fuzzy boundaries i.e. the derivatives change quickly over a short distance but are not discontinuous. Ion density decreases across the outer cone to some minimum and then increases towards the axis. Experimental work by Merlino and D'Angelo [110] found a rarefaction wave in the wake of a negatively charged object (a conducting disk). Ion deflection in their case was assumed to be due to the sheath whereas we are concerned with deflection in the presheath but similarities can be seen between their Fig.6 and our Fig. 6.7. The z velocity increases on entering the outer cone and reaches a peak due to the form of the potential. The z velocity then falls below the flow velocity to some minimum on axis. The further downstream the smaller the density and velocity perturbations.

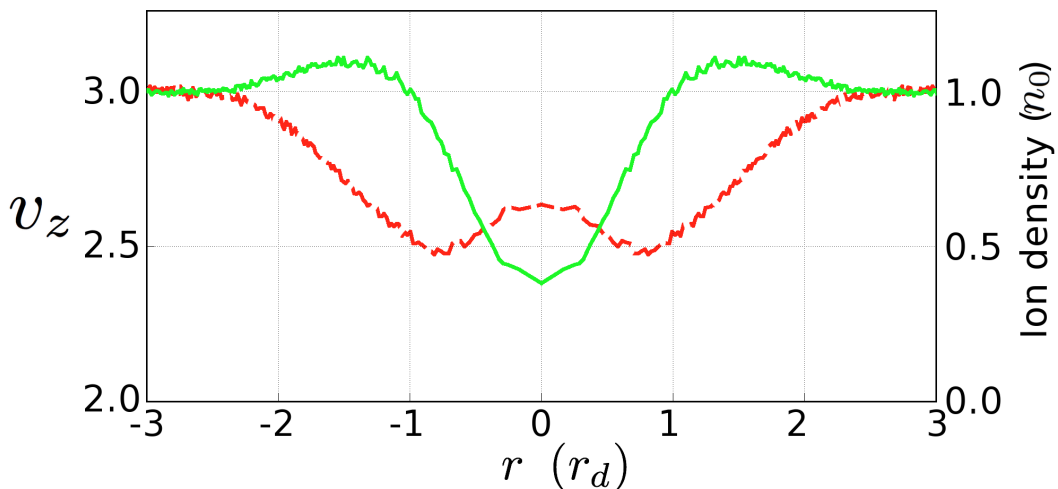


Figure 6.7.: Ion density contour (red, dashed line) and the z component of the flow, v_z (green, solid line). The contour is taken from the downstream wake at $z = 2.0 r_d$. Here $\beta = 0.3$, $u = 3.0$ and $\rho = 40$. u is normalised by $\sqrt{kT_e/m_i}$.

6.3.1 Downstream Negative Space Charge

For flow velocities up to approximately twice the sound speed a spherically symmetric sheath of positive space charge is seen in a thin sheath ($\sim 5\lambda_{De}$) around the grain. We define the sheath edge as the point at which quasineutrality breaks down, Fig. 4.12. For larger flows the positive space charge region behind the grain is reduced due to depletion of ion orbits. This ion depletion has been observed in numerical work concerning spacecraft wakes in the ionosphere [111], this is an example of the direct application of large ρ grains in a supersonic plasma. Increasing the flow velocity further, a negative space charge region develops downstream. This initially enhances the negative potential immediately downstream before being screened. This is a particularly interesting point as the Bohm criterion does not

have to be satisfied for negative space charge. The position of the sheath edge on the axis downstream from the grain is shown in Fig. 6.8 as a function of flow velocity. Note that on this figure $z = 1$ is the downstream edge of the grain.

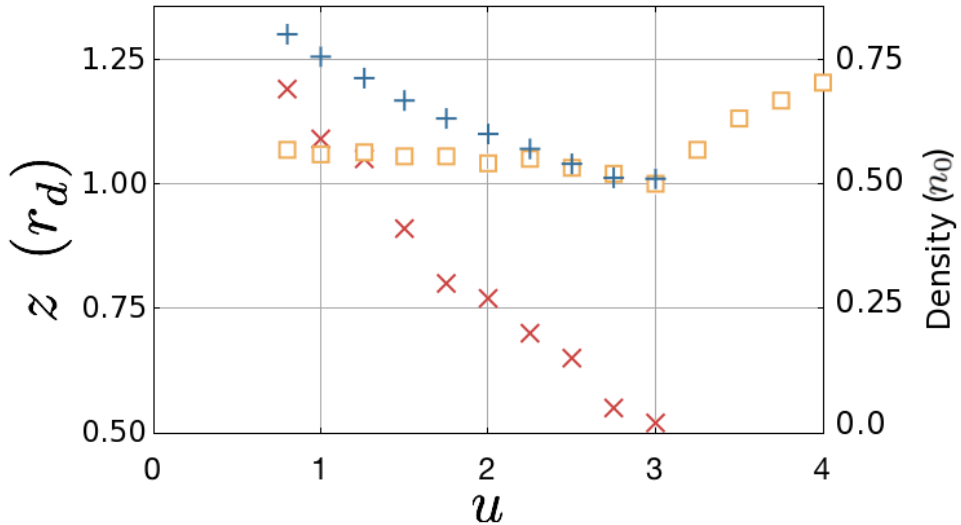


Figure 6.8.: $\beta = 0.2$, $\rho = 80$. Position of the stagnation point (+), position of the downstream sheath boundary (\square) and density at the stagnation point (\times). u is normalised by $\sqrt{kT_e/m_i}$.

For flow around the sound speed a stagnation point, the point on the downstream axis where the average z velocity is zero, is observed. The stagnation point is in the plasma (not in the sheath) and there is a significant ion density at the stagnation point. The position of and density at the stagnation point are shown in Fig. 6.8. As u is increased the stagnation point moves towards the grain. The sheath boundary also moves towards the grain due to the increased depletion of ion orbits, the width of the positive space charge sheath downstream is reduced. In the case shown, at $u \approx 3.0$ the sheath boundary downstream reaches the grain surface, i.e. there is no sheath downstream. Increasing the flow further causes the sheath boundary to move away from the surface but the space charge in the sheath region is now negative. As can be seen in Fig. 6.8, the position of the sheath boundary changes faster with increasing flow when the sheath is negative than when positive.

The inner cone, seen in Fig. 6.6b), is due to converging flows and does not start at the stagnation point. The stagnation point, when it exists, is always closer to the grain than the apex of the inner cone. The inner cone is lost for $\beta \gtrsim 0.5$. This is probably due to the increasing thermal energy of the ion causing them to “wash out” potential structure.

6.3.2 Gas Dynamics

In trying to understand a problem involving Mach cones and compressible flows theoretically, the obvious choice of model is gas dynamics. Assuming cold ions (isothermal) there is a well defined sound speed, $c_s = 1$ (normalised by $\sqrt{kT_e/m_i}$), and the Bohm criterion [55] is $v \geq c_s$. That is, the velocity of the ions at the sheath edge must be greater than or equal to the sound speed. For a non-absorbing spherical object in supersonic flow, a shock wave is expected to form upstream at some standoff distance with the half angle of the cone being the Mach angle, $\sin \theta = c_s/u$. If there is a stagnation point the flow must have transitioned from supersonic to subsonic and a shock would be expected somewhere in the neighbouring region, and the density at the stagnation point should be large.

Work has been carried out by Stangeby and Allen [112] for objects in a flowing plasma of cold ions. The ion and electron densities in the plasma are given by the Boltzmann relation, and the ion motion is described by the equations of fluid flow. In the cold ion case, the motion of a fluid element is the same as the motion of an individual particle hence the ion trajectories follow/are the streamlines. In a region of supersonic flow a Mach surface is defined such that the fluid velocity component perpendicular to the Mach surface is equal to the sound speed. A plasma-sheath boundary, at a positive space charge sheath, is a Mach surface [112]. This is no longer the case for a negative space charge sheath, which may form over part of the plasma boundary. For sufficiently high flow velocities, as seen in Fig. 6.8, the ion depletion behind the grain causes a region of negative space charge to form downstream. As such, a Mach surface around the grain will close on the grain surface rather than extending around the back of the grain, ions cannot be accelerated sufficiently by the presheath to satisfy the Bohm criterion and form a positive sheath downstream. This is shown in Fig. 6.9a), the contour of radial velocity at the cold ion sound speed is the left most contour, if the Bohm criterion were satisfied around the grain this contour would extend around the the grain. Instead the contour closes on the grain itself at some angle downstream indicating the electric field is insufficient to satisfy the Bohm criterion here. Figure 6.9b) shows the breakdown of quasineutrality in this case, a positive region of space charge is seen around the front and sides of the grain, but not the back.

Contrasting our results with the gas dynamic theory, the primary cone may be approximated but very little of the downstream behaviour is predicted. In the case of an absorbing dust grain the shock is replaced by something resembling a weak discontinuity beginning approximately on the grain surface. A thin sheath still exists around the grain, though it is deformed downstream for larger flows. At no point does the plasma move to avoid the grain. Ions are also collected downstream (depending on the flow velocity) and this may lead to a stagnation

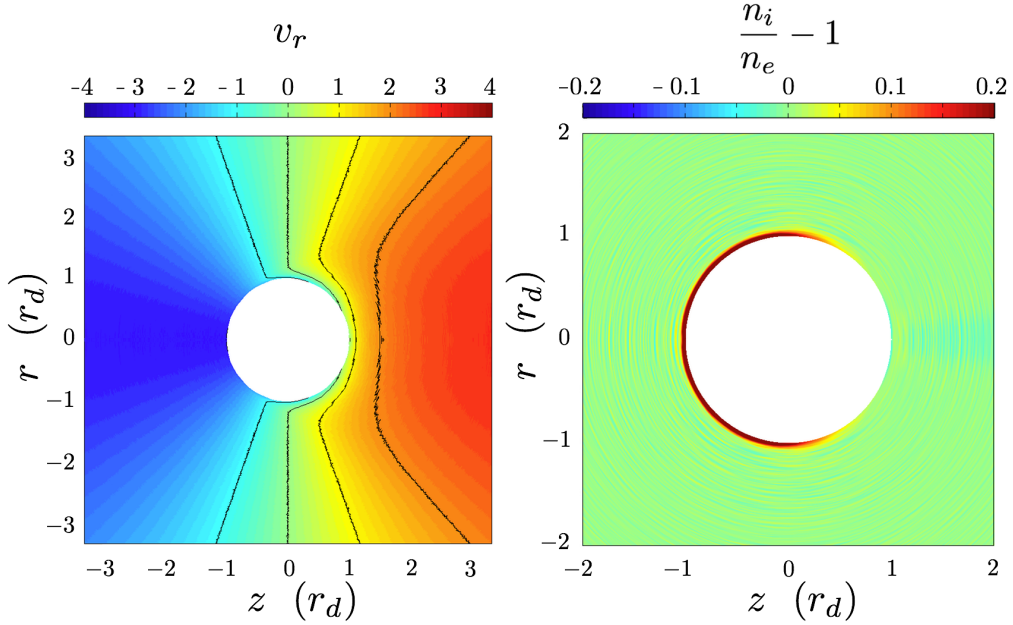


Figure 6.9.: a) Radial velocity (in spherical coordinates) contours around a large dust grain in a flowing plasma, the left most contour is $v_r = \sqrt{kT_e/m_i}$ and closes on the dust grain. b) The break down in quasineutrality. $\beta = 0.2$, $u = 3\sqrt{kT_e/m_i}$ and $\rho = 80$.

point somewhere behind the dust. The outer cone is truncated upstream and “fades away” downstream, the inner cone has an apex. The fact that the Mach cone is truncated upstream is due to the absorbing nature of the grain, the plasma upstream does not need to “know” about the grain unless the ion velocity perpendicular to the plasma-sheath transition is less than the hot ion Bohm/sound speed. The flow is accelerated and deflected upon entering the outer cone and then decelerated as it approaches the inner cone. Here one might expect a shock wave, however no jumps in the potential, density or velocity are observed. This is surprising considering that at some supersonic flow velocities we have a stagnation point and would expect a shock wave, from a compressible fluid point of view, at the transition from supersonic to subsonic flow. The density increases on the axis as the flow converges with the effects on the velocity, potential and density becoming less pronounced the further downstream we look.

6.4 THE PRESHEATH IN SUPERSONIC FLOW

The presheath around a dust grain in a stationary plasma has the function of accelerating the ions to a velocity perpendicular to the sheath which satisfies $v \geq c_s$. If the ions are streaming towards an object at a velocity already satisfying the Bohm criterion then there will be no presheath. If the object were a cone at the Mach angle, i.e. with the same shape as the outer potential contour in Fig. 6.6b) (for that specific

case), the plasma could flow onto it freely as the Bohm criterion would already be satisfied, and there would be no presheath upstream. For the same conditions a cone with a smaller half-angle would require a presheath in order to satisfy the Bohm criterion at its surface. The outer cone is a 2D collisionless presheath required to deflect the ions so they satisfy the Bohm criterion at the sheath edge.

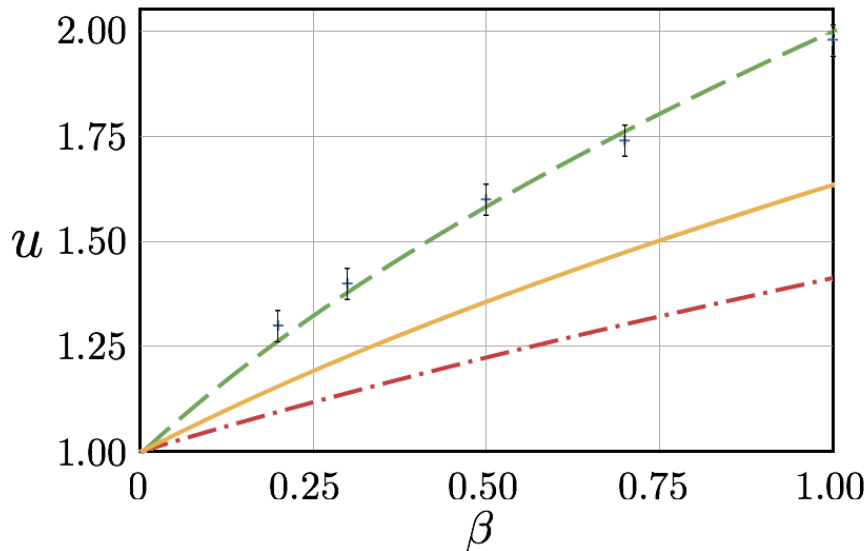


Figure 6.10.: Flow velocity at which the upstream presheath width goes to zero. Fits are $\sqrt{1+\gamma\beta}$ with $\gamma = 1$ (red, dot dashed), $\gamma = 5/3$ (yellow, solid) and $\gamma = 3$ (green, dashed). u is normalised by $\sqrt{kT_e/m_i}$.

The speed of sound is no longer a simple quantity; it depends on the ion temperature, but is not described by any simple expression. The downstream structure is also damped (Landau damping), but less so when T_i is small compared with T_e [114]. In the collision-free case, with finite ion temperature initially, one cannot deduce an adiabatic relation between pressure and density. The warm ion Bohm speed may be estimated by observing the flow velocity at which the upstream presheath width falls to zero, that is, the velocity at which ions approaching from directly upstream are unperturbed right up to the sheath edge. Figure 6.10 shows the flow velocity at which the upstream presheath width goes to zero as a function of β . Alternatively we may use the half angle of the outer cone to determine the speed at which information propagates perpendicular to the flow. Both methods result in a hot ion Bohm/sound speed well approximated by the semi-empirical formula $c_{hot} = \sqrt{k(T_e + \gamma T_i)/m_i}$, with $\gamma \approx 3$. The Mach angle is then $\sin \theta = c_{hot}/v$.

6.5 COMPARISON WITH EXPERIMENT

As in chapters 4 and 5, most of the experimental work performed has focused on small grains suspended in the sheath of a gas discharge [88, 89, 101]. The wake from an object of $\rho \approx 100$, the shuttle orbiter, has been investigated experimentally [115]. Whilst detailed information about the wake is lacking, a significant density depletion is observed in the wake near to the shuttle. This depletion corresponds to the ion vacuum we have observed on the downstream side of our simulated dust grains. More detailed laboratory experiments have been performed by Stone [116, 117]. Here a conducting sphere of $\rho \approx 1$ is subject to fast flowing plasma, Mach numbers around 17, and the density in the wake investigated. The sphere used is not floating, but the potential is varied. The resulting wake behaviour is qualitatively similar to our simulations, with a region of ion depletion directly behind the grain followed by a region of ion focus further downstream. SCEPTIC could be used to make a detailed parameter scan of the position of the ion focus position and extent of the ion vacuum region as a function of plasma flow velocity and grain potential. This would then allow for direct comparison with experiment. We have provided detailed information on the form of the potential and density around a spherical object. Of particular interest is the behaviour of the sheath region as it closes on the grain for sufficiently large flow velocities. Detailed information on the potential, density and ion velocity distribution around this area would be useful, but is likely to be very difficult to obtain experimentally.

6.6 SUMMARY

Wake effects have been investigated primarily for large grains in supersonic flows. The typical terminology used to describe the observed wake phenomenon is Mach cone. However, this is suggestive of shocks and only weak discontinuities are observed. Instead we propose the term Electrostatic Mach Cone (EMC) to refer to these unusual structures.

The general structure of the wake has been reported before [100, 101, 102, 115, 116, 117]. Namely the region of ion depletion and subsequent ion focus. We have investigated the effect of ion temperature on the wake structure and found that whilst the ion temperature is less than approximately half the electron temperature, two nested cones are seen. In other words, structure exists in the wake at appreciable ion temperatures. The isothermal ($\gamma = 1$) gas dynamic model is not appropriate for describing the processes seen in warm, supersonic ion flow past an absorbing object. By observing the upstream presheath width disappearing, and the angle of the primary cone relative to the direction of flow, $\gamma = 3$ is found to be an

excellent approximation for the Bohm velocity. Not only is this a novel approach to determining the ion acoustic speed, it also clarifies what we mean by *ion acoustic speed* when the ions are not cold.

For significant flow velocities an ion vacuum is observed downstream. This has been found experimentally for $\rho \geq 1$ [110, 115, 116, 117]. We provide a more detailed analysis of when this ion vacuum occurs and how far it extends. The ion vacuum forms as the presheath cannot sustain a large enough radial electric field, and maintain quasineutrality, to accelerate the ions sufficiently to satisfy the Bohm condition. Finally, the sheath closing on the grain has not been considered before and the double layer arising from both the sheath-ion vacuum region and the ion vacuum-ion focus region require further study.

LARGE GRAINS AND THE ION DRAG FORCE

This chapter contains a short introduction to the dust in tokamaks code, `DTOKS`. `DTOKS` has been updated with the modified charging theories introduced in §4 and §5. We see the resulting effect on dust grains in tokamak conditions as well as the potential application to other problems.

Effects due to electron emission, which we broadly label secondary charging, have been included in previous `DTOKS` work concerning small grains [119]. Secondary charging is not included here as this chapter is mainly concerned with investigating the effects of the updated charging (and ion drag force) model. Secondary charging is critical in order to accurately model dust charging and motion in a tokamak plasma. As such, the dust trajectories we show here are predominantly illustrative.

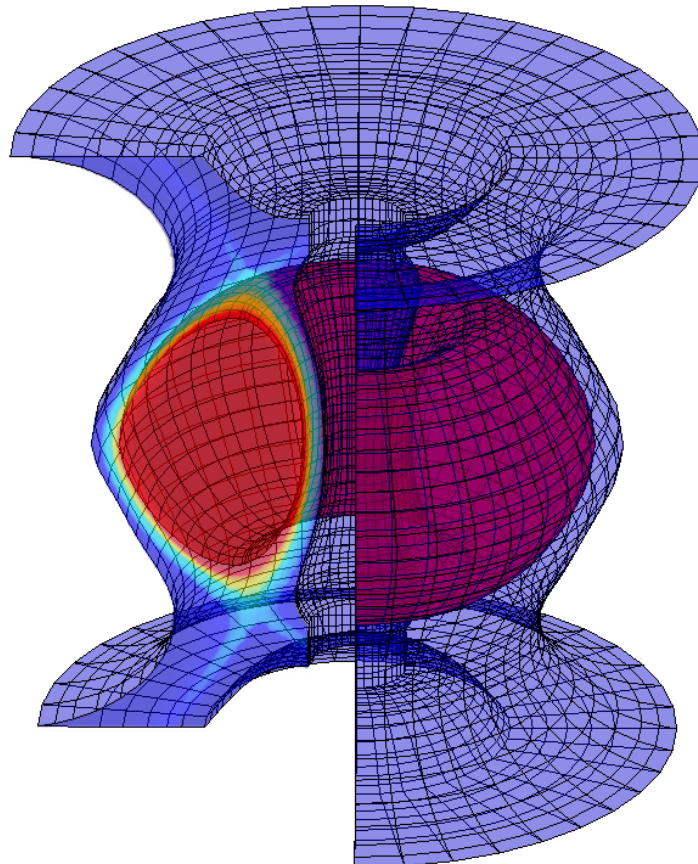


Figure 7.1.: Representation of the 3D background used by `DTOKS`. The electron temperature in `MAST` is shown, red indicates hotter regions and blue cooler.

7.1 DTOKS OUTLINE

`DTOKS`, originally developed by Martin [1, 42], is a “lightweight”, flexible code which takes realistic tokamak plasma backgrounds and tracks dust grain trajectories. Dust grain material is variable, as is launch position, velocity and angle. The code contains detailed charging and heating models which are outlined below.¹

The current incarnation of `DTOKS` has a constant plasma background generated by the `B2-SOLPS 5.0` [118] code. The `B2-SOLPS` code is used to study the scrape off layer and does not provide a profile of the core plasma. This is sufficient for our needs as dust grains reaching the core will quickly evaporate. In addition, dust grains penetrating to the core plasmas will be cause enough for concern without knowing precisely how they behave there. A number of backgrounds are available: two configurations for `MAST` and one for `ITER`. The `DTOKS` backgrounds are time-independent and there is certainly room for improvement therein, this will be discussed in §8. A number of 2D background quantities are shown in Fig. 7.2 for `MAST` and Fig. 7.3 for `ITER`². `DTOKS` assumes the plasma background to be toroidally symmetric and simulates dust motion in 3D. A 3D representation of the `MAST` double-null configuration as used by `DTOKS` is shown in Fig. 7.1.

The background temperatures are important for two reasons:

- The ratio of ion to electron temperature, β , is critical for calculating the potential and determining how incorrect OML is for large grains. Figure 7.2c) shows that β has a large range; there are some regions where the ions are cooler than the electrons, in particular near the divertor region where dust is likely to be present. The lowest β in this particular plasma background is approximately 0.25. We know that for large grains the error in using OML increases as β is lowered. Therefore, the largest inaccuracies in using OML for large grains will be in the divertor region. In `ITER`, we see from Fig. 7.3c) that the ion temperature relative to the electron temperature is generally higher than in `MAST`, as such, OML will not be as poor an approximation.
- The plasma temperature is critical for determining secondary charging effects. The melting and evaporation of a dust grain is also controlled by the temperature. The original version of `DTOKS` includes secondary charging effects however, we limit ourselves to primary charging to observe the effects of our updated charging model directly.

¹ For a complete description of `DTOKS` see [119]

² A comparison of the difference in scale between `MAST` and `ITER` can be found in Fig. B.1

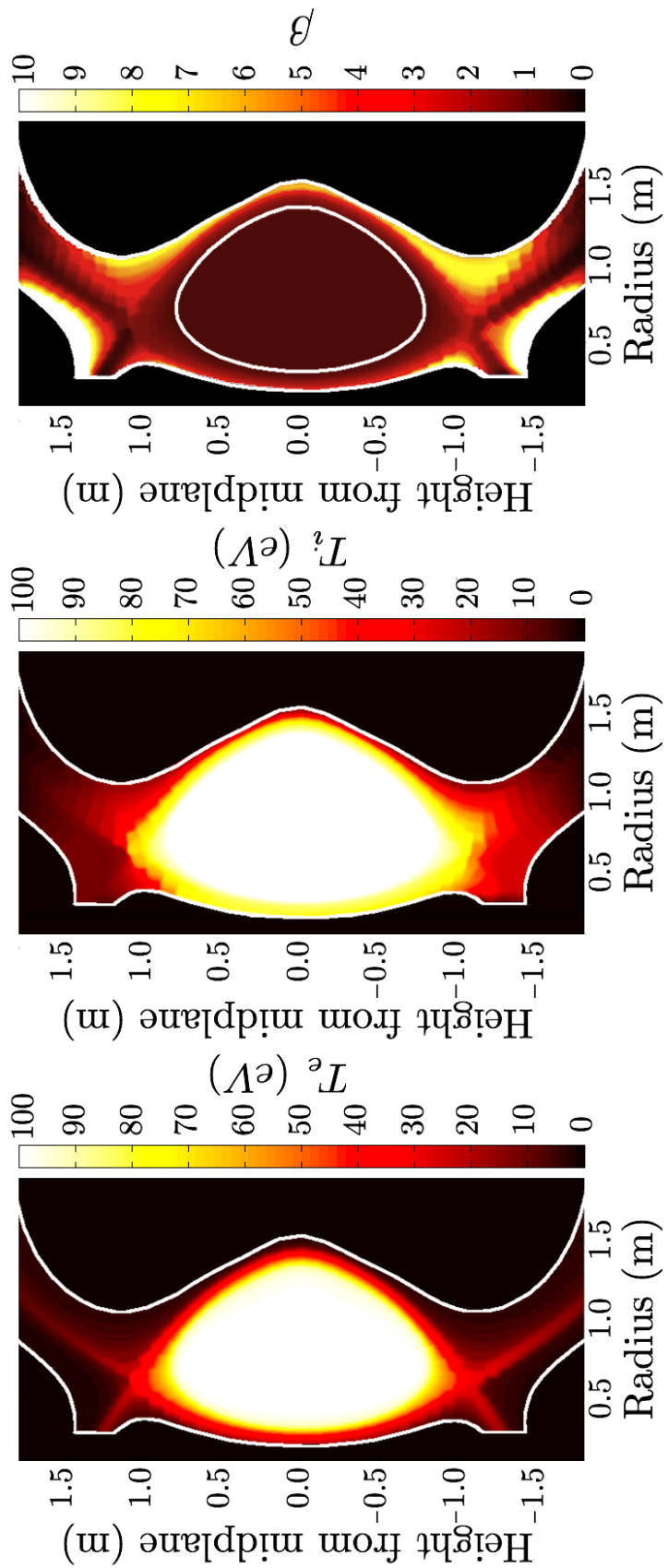
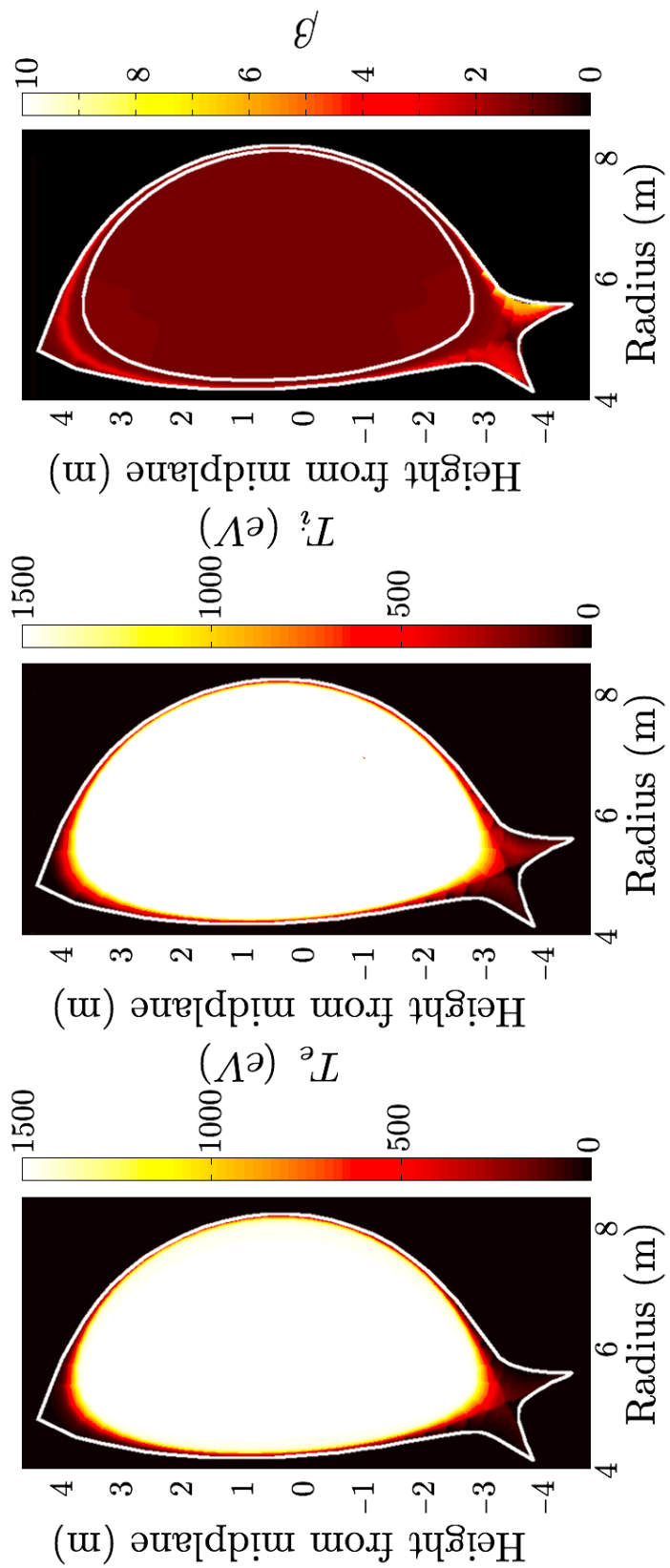


Figure 7.2.: dtoks background for T_e , T_i and β in MAST.

Figure 7.3.: DTOKS background, T_e , T_i and β in ITER.

7.1.1 Secondary Charging

The secondary effects included in DTOKS are [119]:

- Secondary electron emission due to the bombardment of the dust grain by ions and electrons.
- Thermionic emission due to heating of the grain. For low temperatures this current is zero, however, when the thermal energy of the electrons is sufficient to overcome the work function of the material the thermionic current quickly becomes the dominant charging mechanism. This can lead to positive dust grains.

The modified OML/SOML model we have developed provides us with an ion current. As such, we could simply add the additional currents due to secondary effects into the current balance and solve for the potential as normal. However, the problem may be considerably more complex. When using the OML/SOML approach we assume the potential to be monotonic with a positive space charge sheath surrounding the grain. As mentioned, thermionic emission can become the dominant charging mechanism and the subsequent effect on the shape of the potential radially requires careful study, this is discussed further in §8.

In effect we are turning secondary effects off in order to focus on the changes in trajectory purely due to the updated charging models and its effect on the ion drag, described next.

7.1.2 Ion Drag Force

The ion drag force, briefly introduced in section 1.5.4.1, consists of two parts. The first of these is the momentum transferred due to ions striking the dust grain, the collected ions. The second is the momentum transferred by ions deflected in the electric field due to the grain but not striking the grain, the scattered ions.

The ion drag experienced by individual dust grains has received attention recently [44, 87, 120]. Most of this work has focussed on grains smaller than the Debye length where the scattering term dominates, the crux of the matter generally being attributed to choosing an appropriate “effective screening length”. As we are interested in grains large with respect to the Debye length, we will focus on the collection term.

7.1.2.1 Collection Term

The collection component of the ion drag force in DTOKS follows Shukla [11]. It is given by

$$F_c = \pi r_d^2 m_i n_0 \left(\frac{8kT_i}{\pi m_i} \right)^{1/2} (\hat{v} - \hat{v}_{dust}) \left(1 - \frac{e\phi}{kT_i} \right). \quad (7.1)$$

where \hat{v} is the plasma drift velocity and \hat{v}_{dust} is the dust velocity, both are normalised by the ion thermal speed. The above description is the OML ion collection rate multiplied by the average momentum, it is an approximation exact only for zero ion temperature [44], this is clearly not valid in a tokamak plasma. The original argument for using the above is that it is valid for plasma flow velocities much less than the ion thermal speed [45]. This may not be the case as tokamak plasmas can rotate with velocities around the ion thermal speed. In addition, hypervelocity³ dust grains have been reported in the Frascati Tokamak Upgrade [121].

The most consistent value for the collection term is given by integrating the OML momentum flux over a shifted Maxwellian [44], the derivation for this can be found in Appendix C.1.

$$F_c = n_i r_d^2 m \frac{\sqrt{\pi}}{2} \frac{v_T^2}{u^2} \left[u \left(2u^2 + 1 + \frac{2\Phi}{\beta} \right) e^{-u^2} + \frac{\sqrt{\pi}}{2} \left(4u^4 + 4u^2 - 1 - 2(1 - 2u^2) \frac{\Phi}{\beta} \right) \text{erf}(u) \right], \quad (7.2)$$

as usual, $\Phi = -q\phi/kT_e$. As we will be focussing on large grains, it is important to describe the collection contribution well. For small grains it is not as important as the scattering contribution dominates the drag force. We will compare the drag forces from eqn.(7.1) and eqn.(7.2) in section 7.1.3.

7.1.2.2 Scattering Term

The scattering term F_s in DTOKS, which we mention for completeness, is determined via a binary collisions approach

$$F_s = \frac{\sqrt{32\pi}}{3} (\hat{v} - \hat{v}_{dust}) \epsilon_0 \left(\frac{kT_i}{e} \right)^2 \Lambda \beta_T^2.$$

Here Λ is the modified Coulomb logarithm, $\Lambda = -e^{\beta_T/2} Ei(-\beta_T/2)$ (Ei is the exponential integral) and β_T is the thermal scattering parameter, $\beta_T = r_d e |\phi_d| / \lambda kT_i$

³ Velocities of the order of a few km/s

where λ is the effective screening length [119, 122]. Regarding the ion drag force Hutchinson notes [87]:

- The uncertainty in this approach to the scattering force, such as what form the potential takes, is concentrated in the effective screening length λ . The choice of screening length is not clear.
- For $r_d > \lambda_D$ the estimates for the scattering force have little justification. Fortunately, the scattering component quickly becomes small in relation to the collection component, and may be neglected.
- The collection term, eqn.(7.2), will be too large due to the unaccounted for absorption radii.

This third point is exactly what we have addressed with our modified version of SOML.

7.1.3 A Few Potential Choices

At first glance it would appear appropriate to use eqn.(7.2) to describe the collection part of the ion drag force for large grains with the potential determined by modified OML/SOML. However, the effect of the potential in eqn.(7.2) is as a multiplicative factor. In modified OML/SOML the magnitude of the potential increases due to absorption radii reducing the ion current. As such, using the potential from modified OML/SOML in eqn.(7.2) will result in an increase in the ion drag force. As noted above, the collection term is already expected to be too large due to the unaccounted for absorption radii. Therefore, using an even larger value for the potential will increase this error further.

The error in using the grain potential is exactly the problem we overcame in modifying OML, we assumed the ion current to the grain surface as equal to the ion current at the sheath edge. We could use the same approach to determine the ion drag as we did in modifying OML, that is, use the potential at the sheath edge. This seems sensible as the momentum onto an imaginary spherical surface at the sheath edge is the same as the momentum transferred to the grains surface.

Various approaches to the ion drag force are shown in Fig. 7.4. Also shown is the ion drag calculated by SCEPTIC⁴ for a grain of $\rho = 100$ and plasma with $\beta = 0.1$. The SCEPTIC calculation of the drag force includes both the collected and scattering terms implicitly. As such, our estimates made using eqn.(7.2) are expected to underestimate the drag force as we are neglecting the scattering component.

The first solution we discuss is that of eqn.(7.1), the current ion drag collection force in DTOKS. This is shown as the dashed line and is a reasonable approximation of the SCEPTIC ion drag force for $u < 1$, the region we are most interested in. For larger flows it departs from eqn.(7.2) (and the SCEPTIC data) and significantly overestimates the drag force. The blue and red curves are the drag force using the potential from normal SOML and the potential from modified SOML respectively in eqn.(7.2). Despite not including the scattering component, both terms are larger than the SCEPTIC calculated drag force due to the unaccounted for absorption radii, the error in the red curve being largest as the potential is bigger.

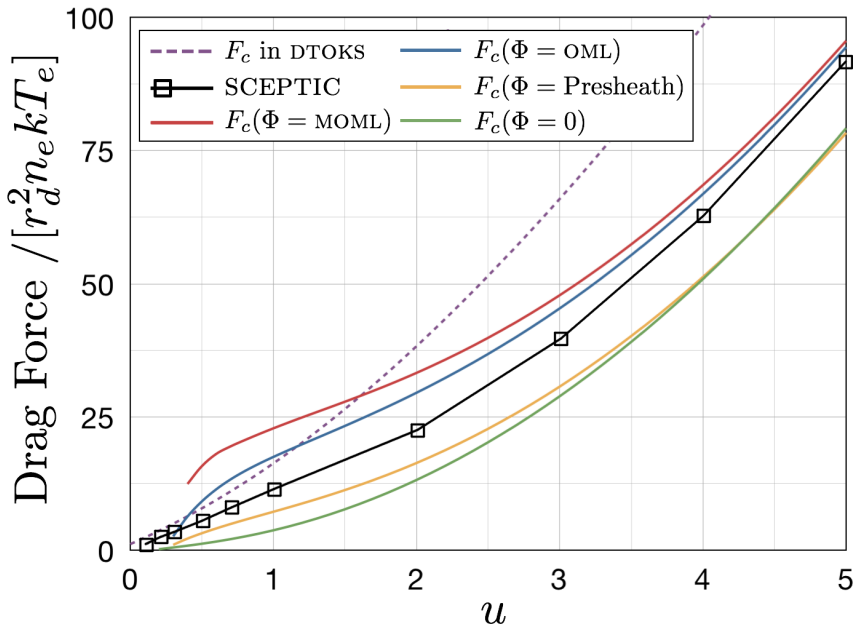


Figure 7.4.: Ion drag components, “ F_c in DTOKS” is the original ion drag model, eqn.(7.1). The SCEPTIC data is reproduced from Fig.14 of [87], $\rho = 100$ and $\beta = 0.1$. The other 4 solid lines are the drag force from eqn.(7.2) as explained in the text.
 u is normalised by $\sqrt{kT_e/m_i}$.

Finally we look at eqn.(7.2) using just the potential drop across the presheath, the yellow curve. Also shown is eqn.(7.2) with the potential set to zero. Using the presheath potential drop provides the best approximation to the SCEPTIC data for $u \lesssim 2$, but not for higher flows. This is interesting as, for large flow velocities we saw in §6 that the upstream flow was unperturbed hence the drag force should be well

⁴ Reproduced from Fig.14 of [87]

represented by the green line. However, in §6 we also observed and discussed the wake effects for supersonic flows. The scattering component due to ion motion in the wake may account for the difference in the drag force between the yellow/green lines and SCEPTIC.

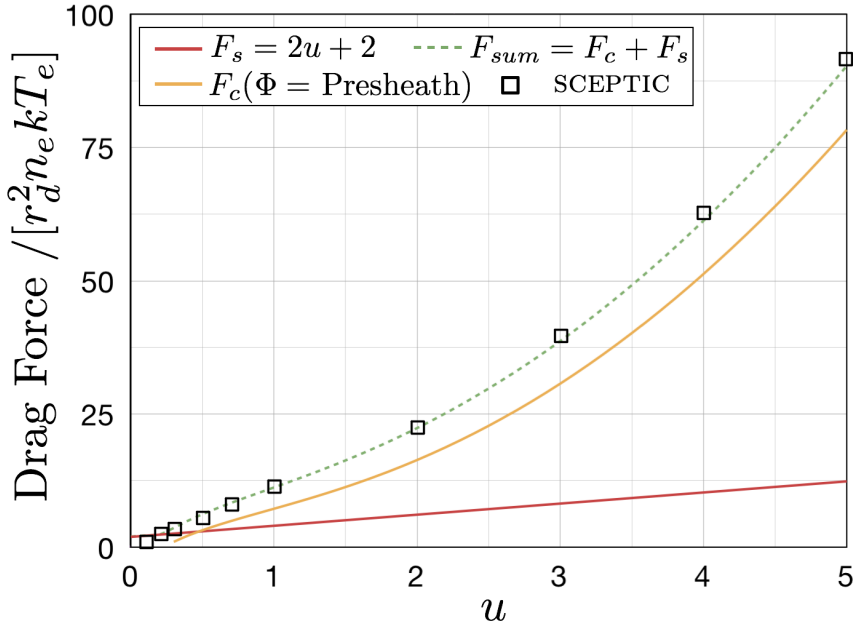


Figure 7.5.: F_c determined via eqn.(7.2) with the potential drop across the presheath used as Φ . The summation of F_c and F_s is seen to fit the SCEPTIC data very well. The SCEPTIC data is reproduced from Fig.14 of [87], $\rho = 100$ and $\beta = 0.1$. u is normalised by $\sqrt{kT_e/m_i}$.

It is interesting to note that estimating the scattering component of the drag force by subtracting the collection component (using the presheath drop) from the SCEPTIC data results in a straight line. For the case shown in Fig. 7.4 the scattering component determined this way is very well approximated by $F_s = 2u + 2$. The scattering and collection components are shown in Fig. 7.5 along with the summation of the two and the SCEPTIC data. The summation indicates just how well the scattering component is represented by this linear dependence on the flow speed.

This is potentially an interesting result and is included as part of the further work discussed in §8. For the subsequent work we choose to use eqn.(7.2) to determine the collection force component with the potential drop across the presheath used as Φ . It appears from Fig. 7.5 that the scattering component is not negligible, particularly for $u < 1$. However, considerable further work is required to describe the scattering force on large grains accurately and we neglect it in the following work.

7.2 2D BACKGROUND

As we are interested in what amounts to a significantly stripped down version of DTOKS we initially look at the motion of a dust grain in two dimensions with a constant temperature background and constant flow speed. This allows us to quickly get a handle on the effect of our charging model over a large parameter space. We will perform some runs in three dimensional tokamaks in the next section.

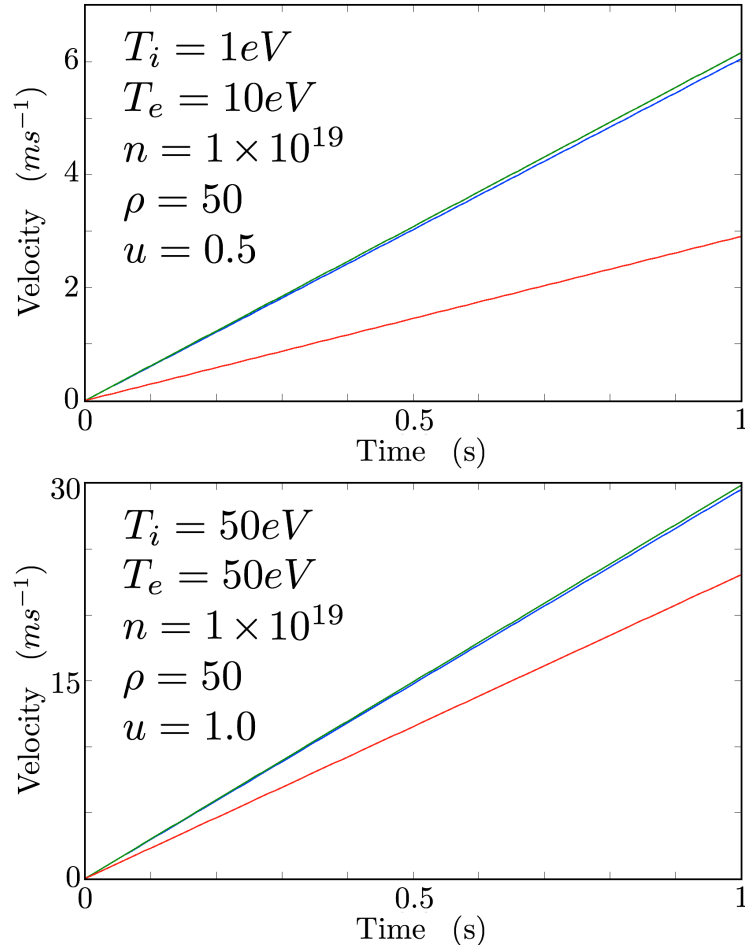


Figure 7.6.: The velocity evolution with time of a dust grain. Each line is calculated using F_c given by eqn.(7.2). The potential described by: OML for the topmost, green line, SOML for the middle, blue line, and the potential at the sheath edge calculated using modified SOML for the bottom, red line.

We see from Fig. 7.6 that, as expected, the choice of charging model has a significant effect on the velocity of the dust grain. The drag force due to collection is significantly reduced if we use modified SOML and take the potential at the sheath edge rather than using OML/SOML.

7.3 3D BACKGROUND

7.3.1 Dust grains in MAST

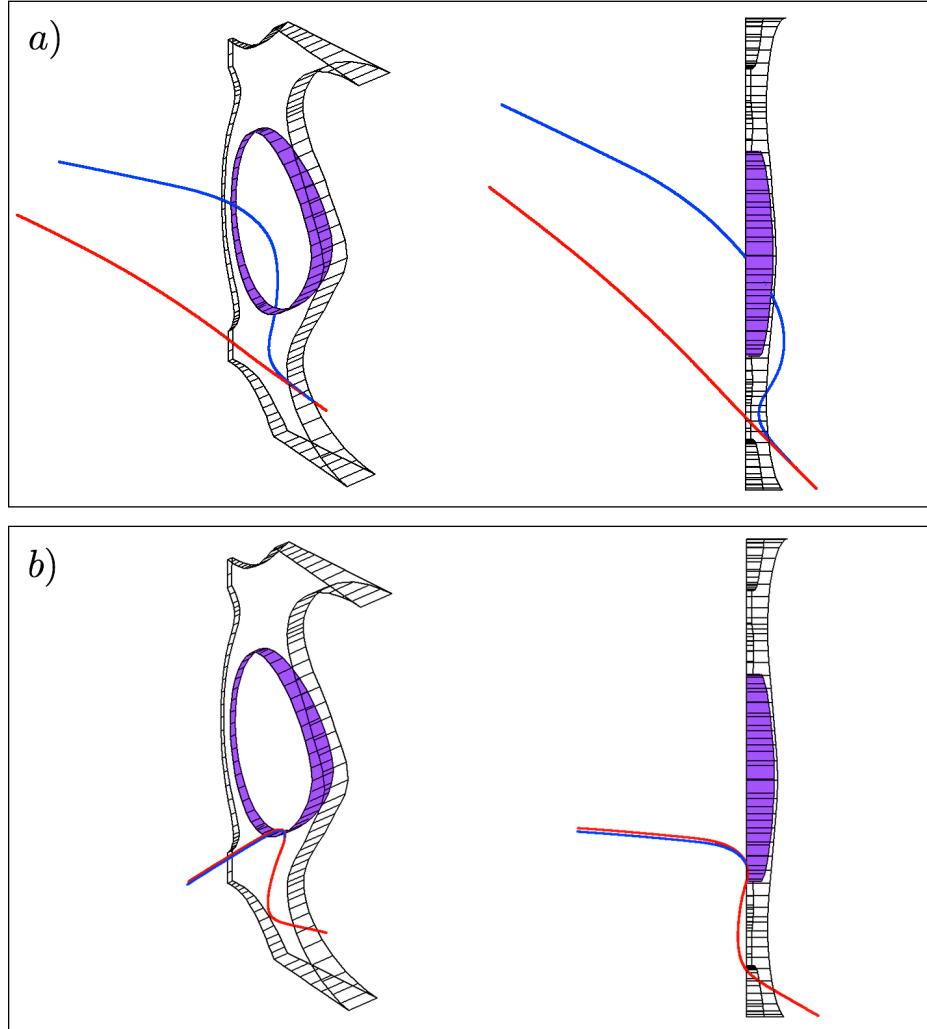


Figure 7.7.: Dust trajectories from the lower divertor in MAST. Carbon grains of $r_d = 20\mu\text{m}$ are injected with initial velocity 15ms^{-1} and two injection angles. The red and blue trajectories indicate the two approaches to the drag force discussed in the text.

Figure 7.7 shows the trajectories of two dust grains in MAST. The dust grains are carbon spheres with an initial radius of $20\mu\text{m}$. The Debye length in the SOL of MAST is $< 1\mu\text{m}$ so $\rho \gtrsim 20$. The choice of initial velocity and injection angle are not obvious, reports of dust detection in MAST [39] have observed grains with velocities $\gg 10\text{ms}^{-1}$ shortly after mobilisation. Here we choose a launch velocity of 15ms^{-1} and two different launch angles. The blue trajectories are determined using standard SOML for the potential and eqn.(7.2) for the drag force. The red trajectories use modified SOML for the potential and eqn.(7.2) with the potential chosen as

that at the sheath edge. The two trajectories shown in Fig. 7.7a) illustrate the considerable impact the choice of charging model can have. The trajectories of the two grains are initially similar as they are launched with identical initial parameters. However, after a short distance the two grains begin to follow considerably different paths. The blue trajectory finds its way briefly into the core plasma whereas the red trajectory does not. Figure 7.7b) highlights the opposite case, here the two trajectories remain very similar over the entire lifetime of the dust grain.

7.3.2 Dust grains in ITER

As with MAST, we now inject dust grains into an ITER plasma background. Figure 7.8 shows a number of dust grains injected from the divertor in ITER. The grains are tungsten spheres of radius $15\mu\text{m}$. Tungsten is chosen as it is one of the proposed materials for ITER's divertor. The grains are launched perpendicular to the divertor with initial velocities of 7ms^{-1} .

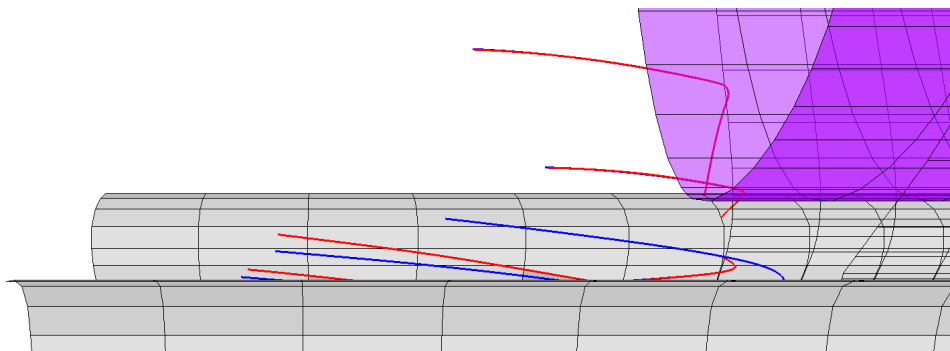


Figure 7.8.: Trajectories of tungsten spheres in ITER. Each grain has an initial radius of $15\mu\text{m}$ and is launched perpendicular to the divertor with initial velocity of 7ms^{-1} .

As expected, a difference can be seen in some of the trajectories. Again, the blue trajectories are determined using standard SOML for the potential and eqn.(7.2) for the drag force and the red trajectories use modified SOML for the potential and eqn.(7.2) with the potential chosen as that at the sheath edge. Figure 7.9 shows the trajectories from the top down. For simplicity we refer to this as the xy plane, the dust grain height in the vessel is then represented by z .

Whilst the 3D views are useful in practise, without the ability to rotate them (i.e. on paper) they are of limited use. The top-down view provides us with some interesting information, the grains are initially injected with velocity only in the zx direction. Due to the plasma rotation they are quickly “swept up” and accelerated around the torus. Depending on the initial conditions the two models either agree or disagree. This highlights a particularly challenging problem with dust simula-

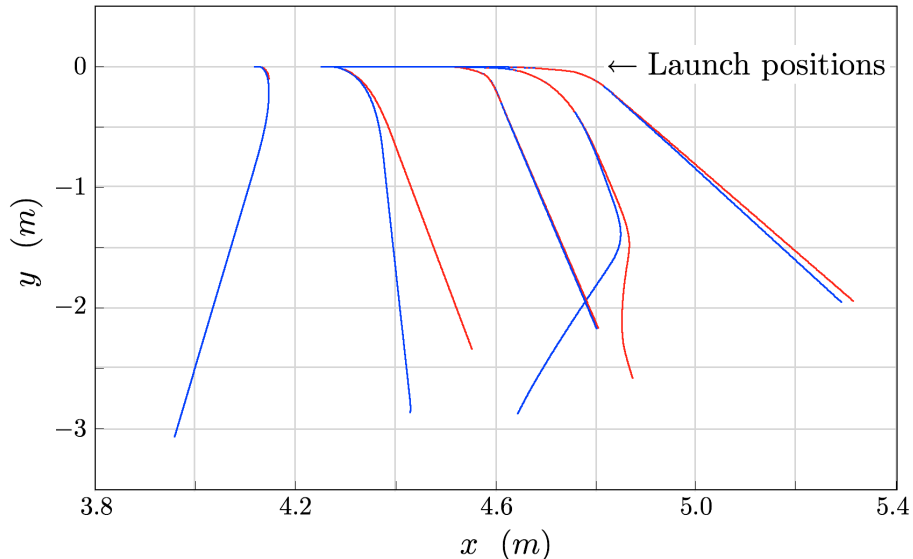


Figure 7.9.: Trajectories of tungsten spheres in ITER, top-down view. Each grain has an initial radius of $15\mu\text{m}$ and is launched perpendicular to the divertor with initial velocity of 7ms^{-1} .

tion in tokamaks. Conditions in the vessel can vary strongly over small regions, sheared flow *et cetera*. A slight variation in the initial conditions, or in the choice of drag/potential model, can have a significant impact on the grains trajectory and consequently, its lifetime.

As with the MAST case, these trajectories are primarily for illustrative purposes. However, they do illustrate that choosing an appropriate model for determining the potential and collection term in the drag force is important. The additions required before a more detailed investigation of dust trajectories can be carried out are discussed in the next chapter.

7.4 APPLICATION TO OTHER PROBLEMS

Whilst we have only briefly investigated the effects of our updated charging model on large grains in tokamak plasmas, this work is applicable anywhere providing $\rho > 1$. As illustrated in §1, situations with $\rho < 1$ are most commonly encountered however, large grains do exist outside of tokamak environments. The majority of these cases are extraterrestrial: spacecraft, comets, asteroids and even planets in the solar wind and interstellar medium. Nevertheless, this work may prove useful in other fields.

SUMMARY AND FURTHER WORK

8.1 SUMMARY AND CLOSING REMARKS

Chapter 1 introduced the subject of dust in plasmas, the work to follow and the motivation behind it. Chapter 2 contained background theory on the problem of dust charging, in addition to previous work on the subject. The PIC code used for the majority of the simulations was outlined in Chapter 3. In Chapter 4 we began by investigating the floating potential over a wide range of parameters in a collisionless, stationary plasma. This initially led to a number of numerical expressions for calculating the floating potential as a function of dust grain radius, a key parameter missing from the often used OML theory, T_i/T_e and the ion mass number. This work was then extended by modifying OML for use in the thin sheath limit by applying OML only in the presheath. Taking a simple planar wall model for the potential drop across the sheath allowed us to form a modified OML ion current. The resulting agreement between this modified theory and PIC simulation was seen to be very good. In Chapter 5 the modified version of OML was extended to include flowing plasmas. Again, the modified theory agreed well with simulation. The modified OML/SOML theory is embodied in the modified SOML current balance:

$$e^{-\Phi} = \sqrt{\beta \frac{m_e}{m_i}} \left[\frac{\sqrt{2\pi\beta}}{4u} \left(1 + \frac{u^2}{\beta} \right) \operatorname{erf}\left(\frac{u}{\sqrt{2\beta}}\right) + \frac{1}{2} \exp\left(-\frac{u^2}{2\beta}\right) + \sqrt{\frac{\pi\beta}{2u^2}} \operatorname{erf}\left(\frac{u}{\sqrt{2\beta}}\right) \frac{\Phi - \Delta\Phi}{\beta} \right].$$

with the sheath drop $\Delta\Phi$ given by

$$\Delta\Phi = \frac{1}{2} \ln \left[2\pi \frac{m_e}{m_i} (1 + \gamma\beta) \right].$$

In the limit of $u \rightarrow 0$ this reduces to modified OML.

We moved away from the floating potential in Chapter 6 and studied the wake effects around large grains in strongly flowing plasmas. Insight was gained into the warm ion Bohm speed and unexpected wake behaviour was observed. Finally, in Chapter 7 we discussed the ion drag force and how to calculate it for grains much larger than the Debye length. We included the modified charging theory in our in-house code DTOKS and updated the ion drag collection term. This was

done in order to investigate the difference in ion drag forces resulting from a more appropriate floating potential for large grains. A distinct difference in particle trajectory was observed validating our initial statement that to correctly predict dust motion in plasma, the floating potential is a critical parameter.

8.2 FURTHER WORK

Some additional work that could be undertaken following directly from the work contained in this thesis is now discussed.

8.2.1 *Modifications to SCEPTIC*

As demonstrated, *SCEPTIC* is a powerful tool for investigating solitary, spherical objects in stationary and flowing plasmas. Two issues stand out with regard to further work using the *SCEPTIC* CODE: the validity of describing the electrons with the Boltzmann relation and the effect of non-spherical dust grains.

8.2.1.1 *PIC Electrons*

There are two main arguments for introducing particle electrons to *SCEPTIC*:

- Tokamak plasmas are permeated by magnetic fields, this will alter the charging of immersed dust grains. Including a magnetic field in the electron's equation of motion invalidates the use of the *SCEPTIC* assumed Boltzmann relation linking the electron density to the potential. To treat magnetic fields properly therefore requires the electrons be handled like the ions. The drawback of including PIC electrons is the much shorter time step required to resolve their motion, in addition to the fact that there are more particles to simulate, and hence more operations required.
- The second argument for particle electrons is the inclusion of secondary charging effects such as thermionic emission. We have not included thermionic emission in any of our work but, in tokamak-like plasmas, it is likely to be a critical factor. Simply adding additional terms to the current balance equation and solving for the potential is not sufficient. The inclusion of a strong thermionic current may have a strong impact on the shape of the potential. It may lead to maxima/minima in the potential, in turn this may have repercussions for electron trapping.

8.2.1.2 Non-spherical Probe

All the work contained here is for spherical grains. Whilst these certainly exist in tokamak plasmas [28], there are other common shapes too. Cylindrical objects are often found, as are flakes of material. It would be interesting to investigate the behaviour of large cylindrical grains, both from a charging and wake point of view. Unfortunately it will prove difficult to modify the shape of the object in SCEPTIC. The code is already cylindrically symmetric hence the inner boundary to form a 3D cylinder would be a 2D rectangle. This would be difficult to define on the spherical grid used in the field solver, this is illustrated in Fig. 8.1. In addition, the inner boundary condition in the code is a current balance assuming the object to be spherical. As charging theories such as OML exist for cylindrical objects, it is possible that this issue may be overcome. Unfortunately the cylinder could only be oriented into the flow.

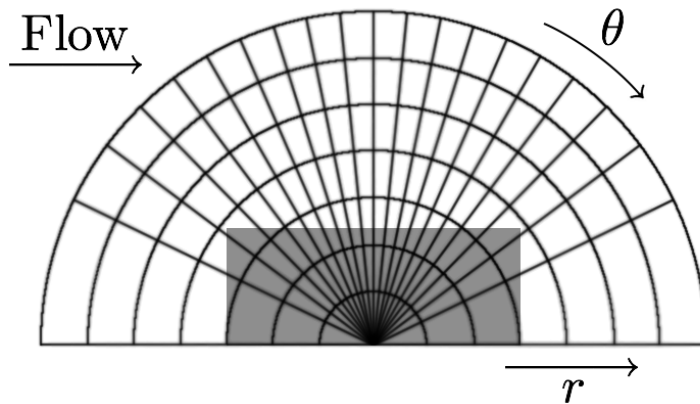


Figure 8.1.: The inner boundary shape (shaded area) required for a cylindrical grain in relation to the computational mesh.

Alternatively, the introduction of a conical object directed into the flow may yield different results after the discussion in Chapter 6. The effects of having a conical object and varying the half angle around the Mach angle may well lead to new insights. In this case the shape of the inner boundary condition may be more easily adapted to the shape of a cone, Fig. 8.2.

8.2.2 Double Cones

The work discussed in Chapter 6 has only scratched the surface of an extensive subject. The drag force due to the scattering of the ions in the wake of large grains was briefly discussed in Chapter 7 and warrants further investigation. The resolution of

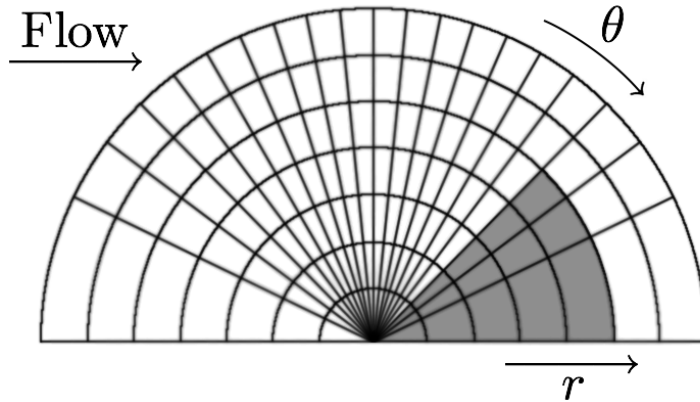


Figure 8.2.: The inner boundary shape (shaded area) required for a conical object directed into the flow.

SCEPTIC directly downstream is poor, improved resolution simulations may lead to new insights. The negative space charge regions seen directly downstream under fast flow conditions, and the breakdown of the Bohm criterion warrant further study. As the grains are large compared to the Debye length this region could perhaps be observed experimentally; measurements of the form of the potential along the axis downstream would be extremely useful.

8.2.3 Modification to DTOKS

Finally some future work regarding DTOKS is discussed. Whilst the code could be updated in a number of ways, here three are suggested which relate closely to the work contained in this thesis.

8.2.3.1 Secondary Charging for Large Grains

The modified version of OML, appropriate for large dust grains, has been incorporated into DTOKS introducing a size dependence into the floating potential. As with OML, the floating potential from modified OML is found by equating an ion and electron current and finding the root. It is therefore easy to include secondary effects, such as thermionic emission, by adding appropriate terms to the current balance. The downside of this approach, as with normal OML, is that we do not know the form of the potential. Additional work is needed as secondary effects may lead to maxima/minima in the potential which could be important for trapping particles.

8.2.3.2 Ion Drag

Hutchinson [87] has performed a detailed investigation of the ion drag force using SCEPTIC. The range of parameters investigated are $0.05 \leq \rho \leq 100$, $0.01 \leq \beta \leq 1.00$ and flow speeds up to $5\sqrt{kT_e/m_i}$. This range is sufficient to cover dust motion in tokamak plasma, with the exception of some parts of the SOL where the ion temperature can exceed the electron temperature, i.e. $\beta > 1$. Hutchinson provides a modified version of the ion drag force which fits the SCEPTIC data closely. Inclusion of this modified drag force into DTOKS may potentially yield significantly different dust particle trajectories as the largest deviations in the Hutchinson ion drag calculations are for flows around the sound speed. In tokamak conditions, the current incarnation of ion drag in DTOKS could be wrong by a factor of 6 or 7¹.

8.2.3.3 Time Varying Background

Finally, the dust grains in DTOKS experience different plasma conditions as they move around the plasma background. Ideally the DTOKS background should evolve in time. Grains launched at different times would then have different trajectories. This is the next milestone in the development of DTOKS, after updating the charging and ion drag models, and will allow the study of time varying affects such as ELMS. The DTOKS code will then be a formidable tool in the simulation of dust lifetime and trajectory in tokamaks.

¹ See Fig.12 of [87]

BIBLIOGRAPHY

- [1] J. D. Martin. *Theory and Simulation of Dust in Tokamak Plasmas*. PhD thesis, Imperial College London (2006)
- [2] F. F. Chen. *Introduction to Plasma Physics*. §1 Plenum Press (1997)
- [3] S. Chandrasekhar and E. Fermi. *Magnetic Fileds in Spiral Arms*. Astrophysical Journal, **118** p113 (1953)
- [4] G. L. Delzanno and G. Lapenta. *Modified Jeans Instability for Dust Grains in a Plasma*. Physical Review Letters, **94** 175005 (2005)
- [5] E. E. Scime, J. L. Phillips and S. J. Bame. *Effects of Spacecraft Potential on Three-dimensional Electron Measurements in the Solar Wind*. Journal of Geophysical Research, **99** A8 4 769 (1994)
- [6] U. Feldman and E. Landi. *On the sources of fast and slow solar wind*. Journal of Geophysical Research, **110** A07109 (2005)
- [7] M. G. Kivelson, C. T. Russel. *Introduction to Space Physics*. New York: Cambridge University Press, (1995)
- [8] D. Samsonov, S. Zhdanov, G. Morfill and V. Steinberg. *Levitation and agglomeration of magnetic grains in a complex (dusty) plasma with magnetic field*. New Journal of Physics, **5** 24 (2003)
- [9] I. Hutchinson. *Ion collection by probes in strong magnetic fields with plasma flow*. Physical Review A **37** 4358-4366 (1988)
- [10] S. Khrapak, D. Samsonov, G. Morfill et. al. *Compressional waves in complex (dusty) plasmas under microgravity conditions*. Physics of Plasma **10** No.1 (2003)
- [11] P. K. Shukla and A. A. Mamun. *Introduction to Dusty Plasma Physics*. IoP Series in Plasma Physics (2002)
- [12] K. U. Riemann. *The Bohm criterion and sheath formation*. Journal of Physics D: Applied Physics, **24**. 493-518 (1991)
- [13] H. Thomas, G. E. Morfill, V. Demmel, J. Goree, B. Feuerbacher and D. Möhlmann. *Plasma Crystal: Coulomb Crystallization in a Dusty Plasma*. Physical Review Letters, **73** 5 (1994)

- [14] R. A. Quinn, C. Cui, J. Goree, J. B. Pieper, H. Thomas and G. E. Morfill. *Structural analysis of a Coulomb lattice in a dusty plasma.* Physical Review E, **53** (3) 652 (1995)
- [15] D. Samsonov, S. K. Zhdanov, R. A. Quinn, S. I. Popel, and G. E. Morfill. *Shock Melting of a Two-Dimensional Complex (Dusty) Plasma.* Physical Review Letters, **92** 255004-1 (2004)
- [16] D. Samsonov, G. Morfill, H. Thomas, T. Hagl, H. Rothermel, V. Fortov, A. Lipaev, V. Molotkov, A. Nefedov, O. Petrov, A. Ivanov, and S. Krikalev. *Kinetic measurements of shock wave propagation in a three-dimensional complex (dusty) plasma.* Physical Review E, **67** (3), 036404 (2003)
- [17] D. Samsonov and G. E. Morfill. *High-speed imaging of a shock in a complex plasma.* IEEE Transactions on Plasma Science, **36** 1020 (2008)
- [18] D. Samsonov, J. Goree, Z. W. Ma, A. Bhattacharjee, H. M. Thomas, and G. E. Morfill. *Mach Cones in a Coulomb Lattice and a Dusty Plasma.* Physics Review Letters, **83** 3649 (1999)
- [19] D. Samsonov, J. Goree, H. M. Thomas, and G.E. Morfill. *Mach cone shocks in a two-dimensional Yukawa solid using a complex plasma.* Physical Review E, **61** (5) 5557-5572 (2000)
- [20] F. F. Chen. *Industrial Applications of Low-Temperature Plasma Physics.* Physics of Plasmas, **2** 2164, (1995)
- [21] Lieberman and Lichtenberg. *Principles of plasma discharges and materials processing.* Wiley Interscience, (1994)
- [22] D. Samsonov and J. Goree. *Particle growth in a sputtering discharge.* Journal of Vacuum Science and Technology A, **17** 2835 (1999)
- [23] D. Samsonov and J. Goree. *Instabilities in a dusty plasma with ion drag and ionization.* Physical Review E, **59** 1047 (1999)
- [24] G. S. Selwyn, E. Heidenreich and K. L. Hailer. *Particle trapping phenomena in radio frequency plasmas.* Applied Physics Letters, **57** 1876 (1990).
- [25] R. Maingi, T. H. Osborne, B. P. LeBlanc *et al.* *Edge-Localized-Mode Suppression through Density-Profile Modification with Lithium-Wall Coatings in the National Spherical Torus Experiment.* Physical Review Letters, **103**, 075001 (2009)
- [26] C. H. Skinner, B. Rais, A. L. Roquemore, H. W. Kugel, R. Marsala and T. Provost. *First real-time detection of surface dust in a tokamak.* Review of Scientific Instruments, **81** 10E102 (2010)

- [27] Ph. Chappuis, E. Tsitrone, M. Mayne, X. Armand, H. Linke, H. Bolt, D. Petti, J.P. Sharpe. *Dust characterization and analysis in Tore-Supra*. Journal of Nuclear Materials, 290-293 245-249 (2001)
- [28] J. Winter. *Dust in fusion devices - experimental evidence, possible sources and consequences*. Plasma Physics and Controlled Fusion, 40:1201, (1998)
- [29] A. T. Peacock, P. Andrew *et al* *Dust and flakes in the JET MkIIa divertor, analysis and results*. Journal of Nuclear Materials, 266:423, (1999)
- [30] H. Maier, K. Kreiger, M. Balden, J. Roth, and the ASDEX Upgrade-Team. *Erosion and deposition in the ASDEX Upgrade tungsten divertor experiment*. Journal of Nuclear Materials, 266:1003 (1999)
- [31] M. Mayer, R. Behrisch, K. Plamann, P. Andrew, J. P. Coad, and A. T. Peacock. *Wall erosion and material transport to the Mark I carbon divertor of JET*. Journal of Nuclear Materials, 266:604, (1999)
- [32] G. Federici, et.al. *Plasma-material interactions in current tokamaks and their implications for next step fusion reactors*. Nuclear Fusion, 41 1967, (2001)
- [33] R. D. Stambaugh et al. *Enhanced confinement in tokamaks*. Physics of Fluids, B: Plasma Physics, 2(12):2941, (1990).
- [34] S. Fielding, J D Ashall, A Colton, D Gates, A W Morris, M Valovic, and the COMPASS-D and ECRH teams. *The H-mode in COMPASS-D*. Plasma Physics and Controlled Nuclear Fusion, 38:1091-1102 (1996)
- [35] P. Jones *An experimental investigation into tokamak edge MHD behaviour*. PhD thesis, Imperial College London (2003)
- [36] T. Fujita. *Spatial structure of internal and edge transport barriers*. Plasma Physics and Controlled Fusion, 44 (Supplement 5A):A19-A35, (2001)
- [37] H. Zohm. *Edge localised modes (ELMs)*. Plasma Physics and Controlled Nuclear Fusion, 38:105-128, (1996).
- [38] J. W. Connor, R. J. Hastie, H. R. Wilson, and R. L. Miller. *Magnetohydrodynamic stability of tokamak edge plasmas*. Physics of Plasmas, 5:531-542, (1998)
- [39] G. De Temmerman, M. Bacharis, J. Dowling and S. Lisgo. *Dust creation and transport in MAST*. Nuclear Fusion, 50 105012 (2010)
- [40] J. P. Sharpe, D. A. Petti, H. W. Bartels. *A review of dust in fusion devices: implications for safety and operational performance*. Fusion Engineering and Design, 63-64 153 (2002)

- [41] A. Kallenbach, M. Kaufmann, D.P. Coster, J.C. Fuchs, A. Herrmann, J. Neuhauser, R. Schneider, K. Borrass, H.-S. Bosch, A. Carlson, J. Gafert, K. Lackner, K. Schmidtmann, J. Schweinzer, W. Suttrop, U. Wenzel, ASDEX Upgrade Team *Scrape-off layer radiation and heat load to the ASDEX Upgrade LYRA divertor*. Nuclear Fusion, **39** 901 (1999)
- [42] J. D. Martin, M. Bacharis, M. Coppins, G.F. Counsell, J.E. Allen. *Modelling dust transport in tokamaks*. Europhysics Letters **83** 65001 (2008)
- [43] M. Bacharis, M. Coppins and J. E. Allen. *The critical issues for modelling dust transport in tokamaks*. Physical Review E, **82** 026403 (2010)
- [44] I. H. Hutchinson. *Ion Collection by a sphere in a flowing plasma: 3. Floating potential and drag force*. Plasma Physics and Controlled Fusion, **47** 71 (2005)
- [45] M. Bacharis. *Theoretical Study of Dust in RF Discharges and Tokamak Plasmas*. PhD thesis, Imperial College London (2009)
- [46] P. C. Stangeby. *The Plasma Boundary of Magnetic Fusion Devices*. IoP (2000)
- [47] S. A. Khrapak, A. V. Ivlev, G. E. Morfill and S. K. Zhdanov. *Scattering in the Attractive Yukawa Potential in the Limit of Strong Interaction*. Physical Review Letters **90**. No. 22 (2003)
- [48] R. V. Kennedy. *Potential Acquired by a Dust Particle Immersed in a Plasma*. D.Phil. Thesis, University of Oxford (2001)
- [49] J. D. Swift and M. J. R. Schwar. *Electrical Probes for Plasma Diagnostics*. Iliffe Books Ltd. §3 (1970)
- [50] I. B. Bernstein and N. Rabinowitz *Theory of Electrostatic Probes in a Low Density Plasma*. Physics of Fluids, **2** 112 (1959)
- [51] I. Langmuir *The Interaction of Electron and Positive Ion Space Charges in Cathode Sheaths*. Physical Review, **33** 954 (1929)
- [52] L. Tonks and I. Langmuir. *A General Theory of the Plasma of an Arc* Physical Review, **34** 876 (1929)
- [53] R. C. Bissell and P. C. Johnson *The solution of the plasma equation in plane parallel geometry with a Maxwellian source*. Physics of Fluids, **30** 779 (1987)
- [54] R. C. Bissell, P. C. Johnson and P. C. Stangeby. *A review of models for collisionless one-dimensional plasma flow to a boundary*. Physics of Fluids B, **1** 1133 (1989)
- [55] D. Bohm *The Characteristics of Electrical Discharges in Magnetic Fields*. Ed. A. Guthry and R. K. Wakerling (New York: MacGraw-Hill) §3, p 77 (1949)

- [56] E. R. Harrison and W. B. Thompson. *The low Pressure Plane Symmetric Discharge*. Proceedings of the Physical Society, **74** 145 (1959)
- [57] J. E. Allen. *A note on the generalized sheath criterion*. Journal of Physics D: Applied Physics, **9** 2331 (1976)
- [58] F. F. Chen. *Introduction to Plasma Physics*. §8 Plenum Press (1997)
- [59] K. U. Riemann. *Bohm's Criterion and Plasma-Sheath Transition*. Contributions to Plasma Physics, **36** S19 (1996)
- [60] K. U. Riemann. *Kinetic theory of the plasma sheath transition in a weakly ionized plasma*. Physics of Fluids, **24** 2163 (1981)
- [61] K. U. Riemann. *The Bohm criterion and the field singularity at the sheath edge*. Physics of Fluids B, **1** 961 (1988)
- [62] P. N. Hu and Ziering S. *Collisionless Theory of a Plasma Sheath near an Electrode*. Physics of Fluids, **9** 2168 (1966)
- [63] J. E. Allen, R. L. F Boyd and P. Reynolds. *The Collection of Positive Ions by a Probe Immersed in a Plasma*. Proceedings of the Physical Society, **70** 297 (1957)
- [64] R. V. Kennedy and J. E. Allen. *The floating potential of spherical probes and dust grains. Part 1. Radial motion theory*. Journal of Plasma Physics, **67** part 4, 243-250 (2002)
- [65] H. M. Mott-Smith and I. Langmuir. *The Theory of Collectors in Gaseous Discharges*. Physical Review, **28** 727-763 (1926)
- [66] J. E. Allen, B. M. Annaratone and U. de Angelis. *On the Orbital Motion Limited Theory for a Small Floating Potential in Maxwellian Plasma*. Journal of Plasma Physics, **63** 299-309 (2000)
- [67] R. V. Kennedy and J. E. Allen *The floating potential of spherical probes and dust grains. II: Orbital motion theory*. Journal of Plasma Physics, **69** 485 (2003)
- [68] J. M. Shull. *Disruption and Sputtering of Grains in Intermediate-Velocity Interstellar Clouds*. The Astrophysical Journal, **226** 858-862 (1978)
- [69] Bohm G, Burhop E H S and Massey H S W: *The Characteristics of Electrical Discharges in Magnetic Fields*. McGraw-Hill §2 (1949)
- [70] J. G. Laframboise. *The theory of spherical and cylindrical probes in a collisionless, Maxwellian plasma at rest*. UTIAS Report, **100** (1966)

- [71] Ya. L. Al'Pert, A. V. Gurevich and L. P. Pitaevskii. *Space physics with artificial satellites*. English edition by Plenum Press, New York (1995)
- [72] I. H. Hutchinson. *Ion collection by a sphere in a flowing plasma: 1. Quasineutral* Plasma Physics and Controlled Fusion, **44** 1953 (2002)
- [73] I. H. Hutchinson. *Ion collection by a sphere in a flowing plasma: 2. non-zero Debye length*. Plasma Physics and Controlled Fusion, **45** 1477 (2003)
- [74] L. Patacchini and I. H. Hutchinson. *Angular distribution of current to a sphere in a flowing, weakly magnetized plasma with negligible Debye length*. Plasma Physics and Controlled Fusion, **49** 1193 (2007)
- [75] L. Patacchini and I. H. Hutchinson. *Ion-collecting sphere in a stationary, weakly magnetized plasma with finite shielding length*. Plasma Physics and Controlled Fusion, **49** 1719 (2007)
- [76] I. H. Hutchinson and L. Patacchini. *Computation of the effect of neutral collisions on ion current to a floating sphere in a stationary plasma*. Physics of Plasmas, **14** 013505 (2007)
- [77] <http://silas.psfc.mit.edu/sceptic/sceptic.tar.gz>
- [78] www.top500.org
- [79] W. J. Duffin. *Electricity and Magnetism*. 3rd ed, McGraw-Hill p100 (1980)
- [80] W. H. Press, S. A. Teukolsky, W. T. Vetterling and B. P. Flannery. *Numerical Recipes. The Art of Scientific Computing*. 3rd ed, §20. Cambridge University Press (2007)
- [81] I. S. Grant and W. R. Philips. *Electromagnetism*. 2nd ed, §3. Wiley (1990)
- [82] C. K. Birdsall and A. B. Langdon. *Plasma Physics Via Computer Simulation*. IoP Series in Plasma Physics, §2 (2005)
- [83] C. T. N. Willis, M. Coppins, M. Bacharis and J. E. Allen. *The effect of particle size on the Floating Potential of dust in a collisionless plasma*. 36th EPS Conference on Plasma Physics, Sofia, **33E**. P-1.104 (2009)
- [84] P. C. Stangeby. *The Plasma Boundary of Magnetic Fusion Devices*. IoP p48 (2000)
- [85] P. C. Stangeby. *The Plasma Boundary of Magnetic Fusion Devices*. IoP p70 (2000)
- [86] C. T. N. Willis, M. Coppins, M. Bacharis and J. E. Allen. *The effect of dust grain size on the floating potential of dust in a collisionless plasma*. Plasma Sources Science and Technology, **19** 065022 (2010)

- [87] I. H. Hutchinson. *Collisionless ion drag force on a spherical grain.* Plasma Physics and Controlled Fusion, **48** 185 (2006)
- [88] A. Melzer, T. Trottenberg and A. Piel. *Experimental determination of the charge on dust particles forming Coulomb lattices.* Physics Letters A, **191**. 301-308 (1994)
- [89] T. Trottenberg, A. Melzer and A. Piel. *Measurement of the electric charge on particulates forming Coulomb crystals in the sheath of a radiofrequency plasma.* Plasma Sources Science and Technology, **4** 450-458 (1995)
- [90] V. E. Fortov, A. P. Nefedov, V. I. Molotkov, M. Y. Poustylnik and V. M. Torchinsky. *Dependence of the Dust-Particle Charge on Its Size in a Glow-Discharge Plasma.* Physical Review Letters, **87** 205002 (2001)
- [91] B. Walch, M. Horanyi and S. Robertson. *Measurement of the Charging of Individual Dust Grains in a Plasma.* IEEE Transactions on Plasma Science, **22** 2 (1994)
- [92] B. P. Pandey, S. V. Vladimirov, and A. A. Samarian. *Charge on the dust in the plasma.* Physical Review E, **83** 016401 (2011)
- [93] S. A. Khrapak, G. E. Morfill, A. G. Khrapak and L. D.G.D'yachkov. *Charging properties of a dust grain in collisional plasmas.* Physics of Plasmas, **12** 052114 (2006)
- [94] V. R. Ikkurthi, K. Matyash, A. Melzer and R. Schneider. *Computation of dust charge and potential on a static spherical dust grain immersed in rf discharges.* Physics of Plasmas, **15** 123704 (2008)
- [95] K. Matyash, R. Schneider, R. Ikkurthi, L. Lewerentz and A. Melzer. *P^3M simulations of dusty plasmas.* Plasma Physics and Controlled Fusion, **52** 124016 (2000)
- [96] E. C. Whipple. *Potentials of surfaces in space.* Reports on Progress in Physics, **44** 1197-1250 (1981)
- [97] D. H. E. Dubin. *The phonon wake behind a charge moving relative to a two-dimensional plasma crystal.* Physics of Plasmas, **7** 3895 (2000)
- [98] W. J. Miloch. *Wake effects and Mach cones behind objects.* Plasma Physics and Controlled Fusion, **52** 124004 (2010)
- [99] W. J. Miloch, H. L. Pécseli and J. Trulsen. *Numerical simulations of the charging of dust particles by contact with hot plasmas.* Nonlinear Processes Geophysics, **14** 575 - 586, (2007)

- [100] W. J. Miloch and J. Trulsen. *Numerical studies of ion focusing behind macroscopic obstacles in a supersonic plasma flow*. Physical Review E, **77** 056408 (2008)
- [101] A. Melzer, V. A. Schweigert and A. Piel. *Measurement of the Wakefield Attraction for "Dust Plasma Molecules"*. Physica Scripta, **61** 494-501 (2000)
- [102] F. Melandø and J. Goree. *Polarized supersonic plasma flow simulation for charged bodies such as dust particles and spacecraft*. Physical Review E, **52** 5312-5326 (1995)
- [103] W. J. Miloch, S. V. Vladimirov, H. L. Pécseli and J. Trulsen. *Wake behind dust grains in flowing plasma with directed photon flux*. Physical Review E, **77** 065401 (2008)
- [104] W. J. Miloch, S. V. Vladimirov, H. L. Pécseli and J. Trulsen. *Numerical simulations of potential distribution for elongated insulating dust being charged by drifting plasmas*. Physical Review E, **78** 036411 (2008)
- [105] W. J. Miloch, S. V. Vladimirov, H. L. Pécseli and J. Trulsen. *Interaction of two elongated dust grains in flowing plasmas studied by numerical simulations*. Physics of Plasmas, **16** 023703 (2009)
- [106] S. V. Vladimirov, S. A. Maiorov and O. Ishihara. *Molecular dynamics simulation of plasma flow around two stationary dust grains*. Physics of Plasmas, **10** 3867-3873 (2003)
- [107] Y. Tyshetskiy and S. V. Vladimirov. *Shielding of absorbing objects in collisionless flowing plasma*. Physics of Plasmas, **17** 103701 (2010)
- [108] C. T. N. Willis, J. E. Allen, M. Coppins and M. Bacharis. *Wakes formed by dust grains in supersonically flowing plasmas*. Physical Review E, **84** 046410 (2011)
- [109] Landau and Lifshitz. *Fluid Mechanics* 2nd ed. §96
- [110] R. L. Merlino and N. D'Angelo. *The interaction of a conducting object with a supersonic plasma flow: ion deflection near a negatively charged obstacle*. Journal of Plasma Physics, **37** part 2 185-198 (1987)
- [111] É. Coggiola and A. Soubeyran. *Mesothermal Plasma Flow Around a Negatively Wake Side Biased Cylinder*. Journal of Geophysical Research, **96**(A5) 7613-7621 (1991)
- [112] P. C. Stangeby and J. E. Allen. *Plasma boundary as a Mach surface*. Journal of Physics A: General Physics, **3** 304 (1970)

- [113] S. Kuhn, K. U. Riemann, N. Jelić. D. D. Tskhakaya, Sr. and D. Tskhakaya, Jr., M. Stanojević. *Link between fluid and kinetic parameters near the plasma boundary.* Physics of Plasmas, **13** 013503 (2006)
- [114] B. D. Fried and R. W. Gould. *Longitudinal Ion Oscillations in a Hot Plasma.* Physics of Fluids, **4** 139 (1961)
- [115] G. B. Murphy, D. L. Reasoner, A. Tribble, N. D'Angelo, J. S. Pickett and W. S. Kurth. *The Plasma Wake of the Shuttle Orbiter.* Journal of Geophysical Research, **94** 6866-6872 (1989)
- [116] N. H. Stone. *The plasma wake of mesosonic conducting bodies. Part 1. An experimental parameters study of ion focusing by the plasma sheath.* Journal of Plasma Physics, **25** 351-371 (1981)
- [117] N. H. Stone. *The plasma wake of mesosonic conducting bodies. Part 2. An experimental parameters study of the mid-wake ion density peak.* Journal of Plasma Physics, **26** 385-397 (1981)
- [118] D. P. Coster, X. Bonnin and M. Warrier. *Extensions to the solps edge plasma simulation code to include additional surface interaction possibilities* Physica Scripta, **T124:9-12** (2006)
- [119] M. Bacharis, M. Coppins and J. E. Allen. *Dust in tokamaks: an overview of the physical model of the Dust in TOKamaks (DTOKS) code.* Physics of Plasmas, **17** 042505 (2010)
- [120] S. A. Khrapak, A. V. Ivlev, S. K. Zhdanov, and G. E. Morfill. *Hybrid approach to the ion drag force.* Physics of Plasmas, **12** 042308 (2005)
- [121] C. Castaldo *et al.* *Diagnostics of fast dust particles in tokamak edge plasmas.* Nuclear Fusion, **47** L5 (2007)
- [122] V. E. Fortov, A. V. Ivlev, S. A. Khrapak, A. G. Khrapak and G. E. Morfill. *Complex (dusty) plasmas: Current status, open issues, perspectives.* Physics Reports, **421** 1-103 (2005)

Part I
APPENDIX

APPENDIX

A.1 THE SOUND SPEED

For cold ions the sound speed is well defined, but for hot ions things are not as clear. Following Chen [2], a collisionless plasma does not support ordinary sound waves. Due to the charge of the constituent ions however, vibrations may be transmitted to other ions, and acoustic waves can still occur. The ions are massive hence the oscillations will be low frequency. The plasma approximation is therefore assumed, i.e. $n_e = n_i = n_\infty$. The ion fluid equation of motion is

$$m_i n \left[\frac{\partial \mathbf{v}_i}{\partial t} + (\mathbf{v}_i \cdot \nabla) \mathbf{v}_i \right] = e n \mathbf{E} - \nabla p.$$

Taking $\mathbf{E} = -\nabla\phi$ and using $p = nkT$ we have

$$m_i n \left[\frac{\partial \mathbf{v}_i}{\partial t} + (\mathbf{v}_i \cdot \nabla) \mathbf{v}_i \right] = -e n \nabla \phi - \gamma_i k T_i \nabla n.$$

Linearising and assuming plane waves

$$-i\omega m_i n_0 v_{i1} = -e n_0 i k \phi_1 - \gamma_i k T_i i k n_1. \quad (\text{A.1})$$

Force balance on the electrons gives

$$n_e = n_0 \exp \left(\frac{e\phi_1}{k T_e} \right) = n_0 \left(1 + \frac{e\phi_1}{k T_e} + \dots \right)$$

The perturbation in the electron density (and hence the ion density) is

$$n_1 = n_0 \frac{e\phi_1}{k T_e}. \quad (\text{A.2})$$

Finally we need the linearised ion continuity equation to relate n_1 and v_{i1}

$$i\omega n_1 = n_0 i k v_{i1}. \quad (\text{A.3})$$

Substituting eqn.(A.2) and eqn.(A.3) into eqn.(A.1) and rearranging, we find the sound speed v_s

$$v_s = \frac{\omega}{k} = \sqrt{\frac{kT_e + \gamma_i kT_i}{m_i}}. \quad (\text{A.4})$$

As the ions are one-dimensionally compressed in the plane waves assumed, γ_i can be set to 3 in this case. As the electrons are considered fast enough to equalise their temperature everywhere they are considered isothermal and γ_e , not included, is equal to 1.

B

APPENDIX

B.1 ITER AND MAST

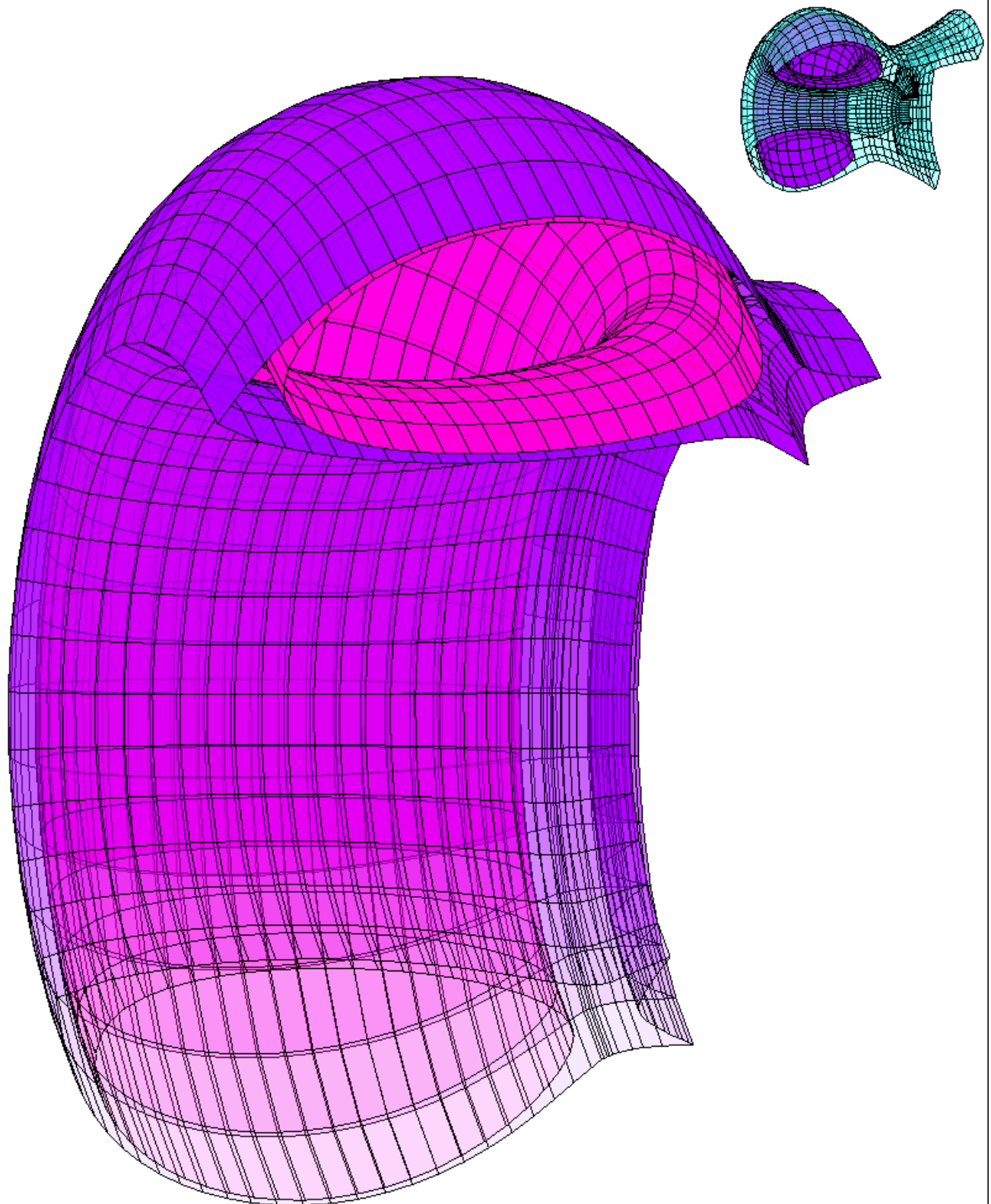


Figure B.1.: A comparison of scale between the *MAST* and *ITER* plasmas

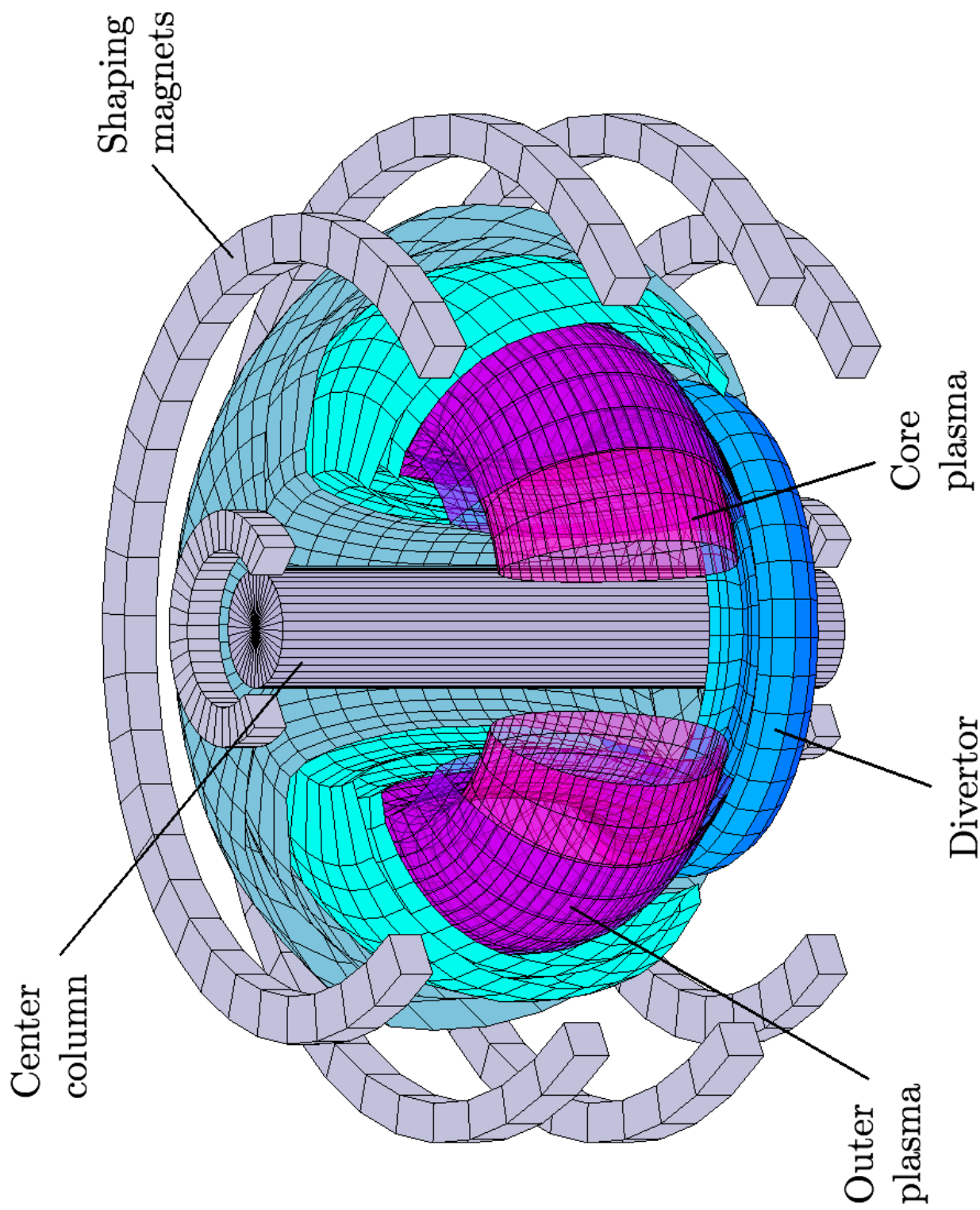


Figure B.2.: A schematic representation of ITER's plasma and main vessel components.

APPENDIX

C.1 SOML ION DRAG VIA COLLECTION

The following derivation is the collection part of the ion drag force, according to soml. Starting in cartesian coordinates with plasma flow w along z and a dust grain at the origin, as shown in Fig.C.1, the momentum components are

$$P_z = mv \cos \theta$$

$$\left. \begin{aligned} P_x &= mv \sin \theta \cos \phi \\ P_y &= mv \sin \theta \sin \phi \end{aligned} \right\} \text{both go to zero.}$$

Force on dust grain along \hat{z} due to collisions is:

$$F_c = \frac{dP}{dt} = m \int_0^\infty v v \sigma(v) f(v) dv$$

The cross section, as in OML, is

$$\sigma(v) = \pi r_d^2 \left(1 - \frac{2q\phi}{mv^2} \right).$$

Taking a shifted Maxwellian distribution with flow along z .

$$f(v) = n_i \left(\frac{1}{\pi v_T^2} \right)^{3/2} \exp \left(-\frac{1}{v_T^2} (v^2 + w^2 - 2vw \cos \theta) \right),$$

where v_T is the thermal velocity $(2kT_e/m)^{1/2}$ and $v^2 = v_x^2 + v_y^2 + v_z^2$.

$$F_c = m \int_0^\infty v \sigma(v) f(v) \mathbf{v} \cdot d\mathbf{v} = m \int_0^\infty v \sigma(v) f(v) v \cos \theta dv$$

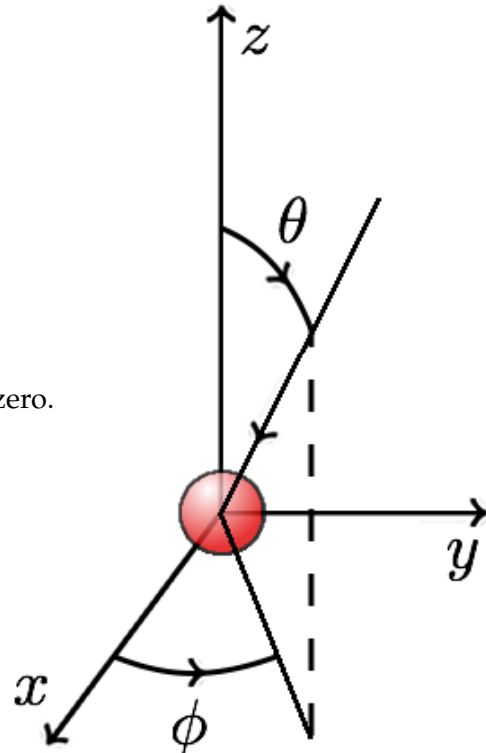


Figure C.1.: Ion drag

Using spherical coordinates

$$F_c = m \int v^2 \sigma(v) f(v) \cos \theta v^2 \sin \theta d\phi d\theta dv.$$

In full then we have

$$\begin{aligned} F_c = m \int_0^\infty \int_0^\pi \int_0^{2\pi} v^4 \pi r_d^2 \left(1 - \frac{2q\phi}{mv^2}\right) n_i \left(\frac{1}{\pi v_T^2}\right)^{3/2} \\ \exp\left(-\frac{1}{v_T^2}(v^2 + w^2 - 2vw \cos \theta)\right) \sin \theta \cos \theta d\phi d\theta dv. \end{aligned}$$

Setting $u = w/v_T$ and integrating over ϕ and θ

$$\begin{aligned} F_c = -n_i r_d^2 \frac{\sqrt{\pi}}{2u^2} \frac{1}{v_T^3} \int_0^\infty \left\{ -2v^3 mw + 4vq\phi w - v^2 v_T^2 m + 2v_T^2 q\phi \right\} e^{-\frac{(v+w)^2}{v_T^2}} + \\ \left\{ -2v^3 mw + 4vq\phi w + v^2 v_T^2 m - 2v_T^2 q\phi \right\} e^{-\frac{(v-w)^2}{v_T^2}} dv. \end{aligned}$$

The first part of the integral

$$\begin{aligned} \int_0^\infty \left\{ -2v^3 mw + 4vq\phi w - v^2 v_T^2 m + 2v_T^2 q\phi \right\} e^{-\frac{(v+w)^2}{v_T^2}} dv = \\ -mv_T^5 \sqrt{\pi} \left\{ \operatorname{erf}(u) \left(u^4 + \frac{q\phi}{mv_T^2} - \frac{1}{4} + u^2 - \frac{2q\phi u^2}{mv_T^2} \right) \right. \\ \left. + e^{-u^2} \left(\frac{u^3}{\sqrt{\pi}} + \frac{u}{2\sqrt{\pi}} - \frac{2q\phi u}{v_T^2 m \sqrt{\pi}} \right) + \left(u^4 + u^2 - \frac{2q\phi u^2}{mv_T^2} - \frac{1}{4} \sqrt{\pi} + \frac{q\phi}{mv_T^2} \right) \right\}, \end{aligned}$$

and the second

$$\begin{aligned} \int_0^\infty \left\{ -2v^3 mw + 4vq\phi w + v^2 v_T^2 m - 2v_T^2 q\phi \right\} e^{-\frac{(v-w)^2}{v_T^2}} dv = \\ -mv_T^5 \sqrt{\pi} \left\{ \operatorname{erf}(u) \left(u^4 + \frac{q\phi}{mv_T^2} - \frac{1}{4} + u^2 - \frac{2q\phi u^2}{mv_T^2} \right) \right. \\ \left. + e^{-u^2} \left(\frac{u^3}{\sqrt{\pi}} + \frac{u}{2\sqrt{\pi}} - \frac{2q\phi u}{v_T^2 m \sqrt{\pi}} \right) + \left(-u^4 - u^2 + \frac{2q\phi u^2}{mv_T^2} + \frac{1}{4} \sqrt{\pi} - \frac{q\phi}{mv_T^2} \right) \right\}. \end{aligned}$$

Summing the two we have the soml ion drag force due to collection,

$$F_c = n_i r_d^2 m \frac{\sqrt{\pi} v_T^2}{2 u^2} \left\{ u \left(2u^2 + 1 + 2\Phi \right) e^{-u^2} + \frac{\sqrt{\pi}}{2} \left(4u^4 + 4u^2 - 1 - 2(1 - 2u^2)\Phi \right) \operatorname{erf}(u) \right\},$$

where $\Phi = -q\phi/kT_i = -2q\phi/mv_T^2$.

C.2 ACCELERATED MAXWELLIAN: 1D

Starting with

$$f_{Max}^{1D}(v_x) = n_i \sqrt{\frac{m_i}{2\pi k T_i}} \exp\left(-\frac{m_i(v-u)^2}{2kT_i}\right).$$

Conservation of energy on a single ion gives

$$E = \frac{1}{2} m_i v_0^2 + e\phi_0 = \frac{1}{2} m_i v_{SE}^2 + e\phi_{SE}.$$

Here E is the total energy and the subscript SE indicates quantities at the sheath edge. Rearranging for v_0

$$v_0 = \sqrt{v_{SE}^2 + \frac{2e(\phi_{SE} - \phi_0)}{m_i}}.$$

Substituting this into our distribution

$$f_{Max}^{1D}(v_x) = n_i \sqrt{\frac{m_i}{2\pi k T_i}} \exp\left(-\frac{m_i}{2kT_i} \left(\sqrt{v_{SE}^2 + \frac{2e(\phi_{SE} - \phi_0)}{m_i}} - u \right)^2\right).$$

Normalising the velocities by $\sqrt{kT_e/m_i}$

$$f_{Max}^{1D}(v_x) = n_i \sqrt{\frac{1}{2\pi\beta}} \exp\left(-\frac{1}{2\beta} \left(\sqrt{\hat{v}_{SE}^2 + \frac{m_i}{kT_e} \frac{2e(\phi_{SE} - \phi_0)}{m_i}} - \hat{u} \right)^2\right),$$

where $\beta = T_i/T_e$ and hats indicate normalised quantities. We finally normalise the potential using

$$\delta\Phi = -\frac{e}{kT_e} (\phi_{SE} - \phi_0)$$

to give

$$f_{Max}^{1D}(v_x) = n_i \sqrt{\frac{1}{2\pi\beta}} \exp\left(-\frac{1}{2\beta} \left(\sqrt{\hat{v}_{SE}^2 - 2\delta\Phi} - \hat{u} \right)^2\right),$$